

**Pumpless Fluid Management on Surfaces:  
Wettability Patterning and Applications**

by

Aritra Ghosh  
B.E. (Jadavpur University, India) 2011

Thesis submitted in partial fulfillment of the requirements  
for the degree of Doctor of Philosophy in Mechanical Engineering  
in the Graduate College of the  
University of Illinois at Chicago, 2018

Chicago, Illinois

Defense Committee:

Constantine Megaridis, Chair and Advisor

W. J. Minkowycz

Amin Salehi-Khojin

Ranjan Ganguly (Jadavpur University, India)

Ryan Enright (Bell Labs, Ireland)

Copyright by

Aritra Ghosh

2018

To Amma, Ma and Baba.

## ACKNOWLEDGMENTS

”Working on a PhD is one of the best things that’s happened to me; you get to be a student and you get paid”, said Dr. G. one sultry morning during the *clueless* phase of my life in my senior (4th-UG) year. Well Dr. G., I can’t agree more.

It’s been a long journey from Jadavpur to Chicago. I would like to acknowledge Professor Constantine Megaridis, my thesis advisor for his constant guidance and support to make this journey a success. His mentoring method of empowering his students and not merely telling what to do gave me the academic freedom to try different things (albeit, failed in many of those). He made my PhD experience enjoyable and rewarding, both professionally and personally. Thank you for everything, Professor.

Dr. Ranjan Ganguly’s (RG) visit to Chicago during my formative years of graduate study was one of the best research experiences I ever had. The central theme of this thesis was an outcome of several fun sessions of experiments tried in the lab. I especially remember his favorite statement at the end the day (generally after 8.00 pm), ”Let’s discuss the results tomorrow morning”. His mornings started at 7:30 am and in between 8 hours of experimental data was to be recorded. RG recently coined a term for this, *torMentoring*. The thesis would not have been possible without several of these *torMentoring* sessions. Thank you, Dr. G.

My internship at Bell Labs, Dublin with Dr. Ryan Enright gave me a gamut of experience at an industrial R&D facility supplementing my PhD training. Ryan is the best researcher

## ACKNOWLEDGMENTS (Continued)

whom I am fortunate enough to know and work with. I still take 2-3 days to process all the information after an hour of discussion with Ryan. Thank you, Ryan for the opportunity.

Sincere thanks, to Drs. Minkowcyz, Salehi-Khojin, Ganguly and Enright for agreeing to serve on my thesis committee.

Past MNFTL members Tom, Joseph and Arindam made my transition to this lab smooth and memorable. The lab grew in personnel really fast. Mohamed, Pat, Theodore, Reza, Ali, Johnny, Uddalok, Jared, Souvick and Pallab made my time in the lab fun and productive, some of whom being contributing co-authors to my MNFTL research work.

I take pride in training my room mates Arunava, Souvick, Pallab, Rakesh and Soumyadip to become more patient in life and develop intuition to deal with hard and challenging circumstances (me being a room mate). Thanks for being there. The favor was returned manyfold, thank you Sameera.

A man is known by his friends surrounding him. I am very lucky to have some of the greatest friends, Sourav, Souvick and Arijita back home in India. Arunava, Souvick, Pallab, Arindam (Madnira), Tirtha, Isha and Sameera for making my stay in Chicago enjoyable. Special mention to Ian, Vicky and Ross from Dublin.

Ma and Baba, I simply would not exist without you two (for obvious reasons!). I can't be grateful enough for all the sacrifices and teachings that you have bestowed on me to be the person I am today. I will try to do better. Dodo, Papa, Jojo and Jeet, thank you for having faith in your elder brother. I would also like to thank my uncles and aunts and all my cousins who made growing up so much fun.

## ACKNOWLEDGMENTS (Continued)

Lastly, sincerest gratitude to several of my teachers, from kindergarten to high school. Special thanks to a few gentlemen and ladies who taught me well what not to do in life.

## Contribution of Authors

- Chapter 1: Aritra Ghosh (AG) wrote the entire chapter. Constantine Megaridis (CMM) and Ranjan Ganguly (RG) advised and made comments for revision.
- Chapter 2: AG conceived the hypothesis and performed all the experiments and data processing. A.G. developed the theory. RG and Souvick Chatterjee (SC) verified the results. CMM encouraged to investigate the normalization of the different shape volumes and overall supervised the work. AG wrote the chapter. All authors commented to refine the chapter.
- Chapter 3: AG, and RG conceived the idea. AG performed all the experiments, fabricated samples and collected data. AG and RG analyzed the data. AG, RG, Thomas Schutzius (TMS) and CMM discussed the results. AG wrote the manuscript. All authors provided critical feedback and help shape the analysis, research and writing the manuscript.
- Chapter 4: AG and RG conceived the idea. AG carried out all sample preparation and experiments. AG and RG lead the analysis of the data and interpretation of the results. Sara Beaini (SB) and Bong June (BJ) provided critical comments regarding testing conditions. AG performed additional experiments for more reliable data. AG took lead in writing the manuscript. RG and CMM commented and refined the manuscript. CMM supervised the overall research. All authors shared feedback.
- Chapter 5: AG, Pallab Sinha Mahapatra (PSM) and CMM conceived and planned the experiments. AG and PSM carried out the experiments. AG prepared all the samples

and collected data. PSM took the lead in analysis and RG in data interpretation. CMM supervised overall research. AG took the lead in writing the manuscript. All authors provided critical feedback and helped shape the research, analysis and manuscript.

## TABLE OF CONTENTS

<u>CHAPTER</u>		<u>PAGE</u>
<b>1</b>	<b>INTRODUCTION . . . . .</b>	<b>1</b>
1.1	Background . . . . .	1
1.2	Capillarity and surface microfluidics . . . . .	5
1.3	Recent advances . . . . .	9
1.4	Thesis objective . . . . .	17
1.4.1	Describing liquid behavior on wettability-patterned tracks . .	17
1.4.2	Demonstrating pumpless transport of liquid by harnessing Laplace pressure gradient on wettability-patterned substrates . . . . .	17
1.4.3	Demonstrate applications beyond lab-on-a-chip . . . . .	18
1.5	Scope of the work . . . . .	18
<b>2</b>	<b>SHAPE OF LIQUID ON WETTABILITY-PATTERNED TRACKS</b>	<b>20</b>
2.1	Introduction . . . . .	20
2.2	Experiment . . . . .	21
2.3	Theory and modeling . . . . .	22
2.3.1	Model: $A_{LG}$ for configuration C1 and C2 . . . . .	25
2.3.2	Assumptions . . . . .	28
2.4	Results and discussion . . . . .	29
2.4.1	Case study: $L = 50 \text{ mm}$ , $\delta = 1 \text{ mm}$ . . . . .	29
2.4.2	Model vs experiment . . . . .	36
2.4.3	Parametric variation of track width $\delta$ . . . . .	37
<b>3</b>	<b>RAPID PUMPLESS TRANSPORT . . . . .</b>	<b>42</b>
3.1	Introduction . . . . .	42
3.2	Materials and methods . . . . .	46
3.2.1	Materials . . . . .	46
3.2.2	Methods . . . . .	47
3.3	Results and discussion . . . . .	50
3.3.1	Liquid transport along a wedge-shaped track . . . . .	50
3.4	Liquid transport using complex pattern . . . . .	61
3.4.1	Droplet metering, merging and rapid transport . . . . .	61
3.4.2	Droplet splitting in multiple equal volumes . . . . .	66
3.4.3	Liquid transport up an incline . . . . .	68
<b>4</b>	<b>PUMPLESS TRANSPORT AUGMENTING DROPWISE CON- DENSATION . . . . .</b>	<b>72</b>
4.1	Introduction . . . . .	72

## TABLE OF CONTENTS (Continued)

<u>CHAPTER</u>		<u>PAGE</u>
4.2	Materials and methods . . . . .	79
4.2.1	Materials . . . . .	79
4.2.2	Sample preparation . . . . .	79
4.2.3	Characterization . . . . .	81
4.2.4	Experiments and image analysis . . . . .	81
4.3	Results and discussion . . . . .	82
4.3.1	Control of condensate droplet size: Proof of concept . . . . .	82
4.3.2	Dimensioning patterns for drop size control . . . . .	89
4.3.3	Dependence of DWC heat transfer rate on departing drop size: Theoretical basis . . . . .	92
4.3.4	Water collection tests . . . . .	97
4.3.5	Design considerations for optimal collection . . . . .	102
<b>5</b>	<b>PARAMETRIC STUDY OF ENHANCED DROPWISE CONDENSATION ON WETTABILITY-PATTERNED SURFACES .</b>	<b>107</b>
5.1	Introduction . . . . .	107
5.2	Experimental procedure . . . . .	111
5.3	Results and discussion . . . . .	113
5.3.1	Pattern design for enhanced condensate transport . . . . .	113
5.3.2	Effect of FWC fractional area ratio . . . . .	119
<b>6</b>	<b>CONCLUSIONS AND RESEARCH OUTLOOK . . . . .</b>	<b>126</b>
6.1	Shape of liquid on wettability-patterned tracks . . . . .	126
6.2	Rapid pumpless transport . . . . .	127
6.3	Pumpless transport augmenting dropwise condensation . . . . .	128
6.4	Parametric study of enhanced dropwise condensation on wettability- patterned surfaces . . . . .	129
6.4.1	Research outlook . . . . .	130
	<b>APPENDICES . . . . .</b>	<b>132</b>
	<b>Appendix A . . . . .</b>	<b>133</b>
	<b>Appendix B . . . . .</b>	<b>142</b>
	<b>Appendix C . . . . .</b>	<b>150</b>
	<b>Appendix D . . . . .</b>	<b>152</b>
	<b>Appendix E . . . . .</b>	<b>156</b>
	<b>CITED LITERATURE . . . . .</b>	<b>157</b>
	<b>VITA . . . . .</b>	<b>173</b>

## LIST OF TABLES

<u>TABLE</u>		<u>PAGE</u>
I	DEVIATION OF THEORETICAL AND EXPERIMENTAL $V_{CR}$ FOR VARIABLE RECTANGULAR TRACK WIDTHS. PERCENTAGE DEVIATION IS WITHIN ADMISSIBLE EXPERIMENTAL ERROR LIMIT. . . . .	40
II	SESSILE CONTACT ANGLE VALUES ON VARIOUS SUBSTRATES. CONTACT ANGLE DATA EVALUATED FROM SETS OF 10 READINGS. * CONTACT ANGLES TOO LOW TO MEASURE. . . . .	51
III	SUMMARY OF CONDITIONS (CASES C1 AND C2) AND EXPERIMENTAL RESULTS (CONDENSATION HEAT TRANSFER COEFFICIENT AND CONDENSATE COLLECTION RATE) COMPARING THE PLAIN ALUMINUM, MIRROR-FINISH UNPATTERNED CONTROL CASE WITH TWO PATTERNED CONFIGURATIONS* . . . . .	99
IV	SUMMARY OF CONDITIONS (CASES C1 AND C2) AND COMPARISONS OF CONDENSATION HTC AND CONDENSATE COLLECTION RATE ON THE PATTERNED SURFACES AGAINST THE CONTROL CASES OF MIRRORFINISHED ALUMINUM (DWC ONLY), SUPERHYDROPHILIC SURFACE (FWC ONLY), AND SUPERHYDROPHOBIC SURFACE (DWC ONLY). . . . .	118
V	CONTACT ANGLE FROM DIFFERENT REGIONS OF THE SUBSTRATE. *CA VALUES TOO LOW TO MEASURE. . . . .	142

## LIST OF FIGURES

<u>FIGURE</u>		<u>PAGE</u>
1	Schematic of a) spreading criterion of a liquid on a solid surface, b) directional transport of liquid along 2-D superhydrophilic tracks, surrounded by superhydrophobic strips. . . . .	5
2	Pumpless liquid-transport mechanisms: a) Schematic showing spreading of a liquid droplet on a porous substrate (a1, classical wicking) and a solid impermeable substrate with micro-nano roughness structures (a2, hemi-wicking). For both cases, spreading distance varies as $x \sim t^{0.5}$ . b) Tuning the curvature of liquid droplet to vary the Laplace pressure. (b1) Circular hydrophilic patches of diameter $d$ , surrounded by a hydrophobic background confine liquid droplets of different volumes. The radius of curvature for each case is different, although the hydrophilic patch area is the same. This causes a variable Laplace pressure, which scales with the curvature of the droplet. (b2 ) Representative plot showing how Laplace pressure changes with liquid volume on a hydrophilic disk of constant diameter. c) Thermal (c1) and chemical (c2) surface tension gradients in a liquid volume promote fluid actuation. In (c1), a temperature gradient on the substrate changes the local surface tension at the advancing (right) and receding (left) end of the liquid volume. (c2) represents how surfactants can alter local surface tension chemically, hence mobilizing the droplet by the differential capillary force between the advancing (right) and receding (left) fronts. $\gamma_{lgR}$ and $\gamma_{lgA}$ denote the liquid surface tension at the receding and advancing end, respectively. d) Droplet actuation by patterning the wettability of the substrate. (d1) Substrate with spatially-gradual wettability changes. The droplet moves from the hydrophobic to the hydrophilic region. (d2) Droplet actuation by a wettability step. The property of the substrate suddenly shifts from hydrophobic (left) to hydrophilic (right). Note the difference in shape of the droplet at the onset of transport. . . . .	8

## LIST OF FIGURES (Continued)

<u>FIGURE</u>		<u>PAGE</u>
3	Examples of wicking flow: a) Automated sequential fluid delivery in a 2D paper network. Each leg wicked fluid from a single buffer source, and dried dyes representing reagents created different fluids from each leg (colours). Each coloured fluid arrived at a different time at the detection zone (green box) and was shut off in a timed sequence after delivery. (Below) Time courses show colour across the full strip width or the detection zone as a function of time after device activation. Reproduced from Lutz et al. 2013 with permission from The Royal Society of Chemistry. b) Detection of individual heavy metals from a water sample using a multiplexed bioactive paper sensor. The aqueous sample containing Hg(II), Cu(II), Cr(VI), and Ni(II) was added to the circular regions of assay zones with markers for identifying individual elements. Reprinted with permission from Hossain et al. Copyright (2011) American Chemical Society. c) Electro-chemical detection on a three-electrode paper-fluidic device. The hydrophilic area at the center of the device wicked sample into the three separate test zones. Reproduced from Li et al. with permission from American Institute of Physics (Biomicrofluidics), Copyright 2012 d1) Brass-coated yarn (top) rejected a drop of aqueous dye deposited on it, while degummed, surfactant-treated silk yarn (lower) allowed the fluid to wick along its length. d2) A fabric chip showing proof of concept for selective wetting. Aqueous green dye solution deposited at one end flowed only along the hydrophilic yarns. An unused chip (white) is shown for contrast. Reproduced from Choudhary et al. 2015 with permission from The Royal Society of Chemistry. . . . .	12

## LIST OF FIGURES (Continued)

<u>FIGURE</u>		<u>PAGE</u>
4	<p>a) Long-range and short-range chemical interactions of two-component droplets, leading to spontaneous motion. (Top) Overlaid timelapse image of multiple coloured droplets deposited on a clean glass slide, interacting autonomously for 2 mins. Scale bar denotes 10mm. (Bottom) Two 0.5 <math>\mu\text{l}</math> droplets of 25% PG in water (blue) and 1% PG in water (orange) interacting. The behaviour can be divided into long-range attraction and short-range chasing portions. Scale bar denotes 3mm. Adapted by permission from Macmillan Publishers Ltd: [Nature] Cira et al. copyright (2015)</p> <p>b) Droplet of PDMS moving along a heater array by thermo-capillary actuation. A thin residue trailed the wetting droplet. The image sequence represents times <math>t = 0\text{s}, 44\text{ s}, 88\text{ s}</math> and <math>132\text{ s}</math>. Reproduced with permission from Journal of Microelectromechanical Systems, Copyright (2003) IEEE, DOI:10.1109/JMEMS.2003.820267. Darhuber et al.</p> <p>c) Uphill motion of a 1 <math>\mu\text{L}</math> drop on a surface-tension-gradient surface inclined at an angle <math>15^\circ</math>. Reprinted with permission from Science, Copyright 1992, AAAS. Chaudhury and Whitesides 1992</p> <p>d) Motion of a 2 <math>\mu\text{L}</math> glycerol/water droplet on a pattern with varying fraction of hydrophilic-to-total area of the plate. Radius of input droplet is 0.78 mm. Reprinted with permission from Bliznyuk et al.. Copyright (2011) American Chemical Society.</p> <p>e) Top views of free running droplets on a track delimited by hydrophobic regions. Time interval between two consecutive frames is 0.1 s and the scale bar is 1 cm. Reprinted with permission from Santos et al. Copyright (1995) American Physical Society.</p>	13
5	<p>a) Schematic drawing of a typical superhydrophilic rectangular track of length <math>L</math> and constant width <math>\delta</math>, surrounded by a superhydrophobic domain.</p> <p>b and c) Side views from experiment: Static liquid volume shape. (b) Configuration 1, liquid in the shape of a cylindrical sector. (c) Configuration 2, liquid in the shape of cylindrical sector plus bulge. Dotted white lines in (b) and (c) show the surface of the underlying metal plate and define the datum line <math>h = 0</math> for liquid height. . . . .</p>	23
6	<p>Model of liquid shape depicting two different configurations on a rectangular superhydrophilic track. a) Side view for Configuration 1, which is a part of a cylindrical sector and Configuration 2, which consists of a cylindrical sector over a reduced track length and the bulge. b) Straight-on view of liquid for Configurations 1 and 2; the outline is approximated by a circular segment. . . . .</p>	26

## LIST OF FIGURES (Continued)

<u>FIGURE</u>		<u>PAGE</u>
7	<p>a) Image sequence showing side profile of liquid deposited gently on a superhydrophilic rectangular track one droplet at a time. Note the transition in morphology between 4<sup>th</sup> and 5<sup>th</sup> droplet. White scale bar is 5 mm. b) Height trace (black dashed line) and bulge boundary demarcation (red line) from image analysis of sequence in a. c) Height of residual liquid (<math>h_{res}</math>, red triangles) and maximum bulge height (<math>h_{bul}</math>, blue diamonds) plotted against total liquid volume (<math>V_{tot}</math>). The black dashed line marks the critical height of the liquid where bifurcation takes place. d) Length of bulge <math>\Delta x_{bul}</math> variation with <math>V_{tot}</math>. Track dimensions for a, b, c and d are <math>L = 50mm, \delta = 1000\mu m</math>. . . . .</p>	32
8	<p>a) Variation of liquid-gas interfacial surface area with total volume of the liquid deposited on the track. <math>A_{LG}</math> for bulge (blue diamonds), residual volume (red triangles), total volume (open black squares with dashed line). The blue solid line is plotting theoretical <math>A_{LG}</math> assuming no transformation of the liquid from Configuration 1 (C1) to 2(C2) with increasing volume. The dotted purple line parallel to the y-axis is the theoretical critical volume (<math>V_{cr} \sim \frac{\pi\delta^2L}{8}</math>) coinciding with the experimental total volume of bifurcation. b) Bulge volume (<math>V_{bul}</math>, blue diamonds) and residual volume (<math>V_{res}</math>, red triangles) plotted vs total liquid volume. The black dashed line is the summation of <math>V_{bul}</math> and <math>V_{res}</math> i.e. <math>V_{tot}</math>. <math>V_{bul}</math> runs parallel to <math>V_{tot}</math> after the bulge is fully formed. . . . .</p>	35
9	<p>Composite plot showing comparison of experimental data and proposed model. In the primary axis, total <math>A_{LG}</math> is plotted for Configuration 1 (blue solid) and Configuration 2 (black dashed) from the model with increasing liquid volume. Black cross overlays the total <math>A_{LG}</math> from experimental data. The point of bifurcation from experiment matches well with the model. On the secondary axis, curvature of the liquid, which is an indicator of the Laplace pressure, is plotted with increasing volume for Configuration 1. Peak pressure point (where radius of curvature is maximum, i.e. <math>\theta_{app} \sim 90^\circ</math>) approximately coincides with the experimental and theoretical bifurcation volume. . . . .</p>	38

## LIST OF FIGURES (Continued)

<u>FIGURE</u>		<u>PAGE</u>
10	Plot showing $A_{LG}$ , $h_{res}$ and $h_{bul}$ with increasing $V_{tot}$ for tracks of varying width ( $\delta = 500, 750, 100, 1250, 1500\mu m$ ). a) The dashed line is the critical height for each track where $h_{cr} = \delta/2$ . $h_{res}$ initially rises till bifurcation and then decreases to a steady value, a similar trend for all track widths. The bifurcation point shifts to the right with increasing $\delta$ . b) Total, bulge volume area is increasing and residual volume area $A_{LG}$ is initially increasing till bifurcation and then decreasing with rising volume. Blue solid line is the theoretical $A_{LG}$ considering Configuration 1 for increasing volume. Experimental $A_{LG}$ deviates from theoretical value due to transition of liquid morphology from C1 to C2. The purple dotted line is the theoretical $V_{cr}$ which coincides with experimental $V_{tot}$ at the onset of bulge formation. . . . .	39
11	Normalized residual volume vs. normalized total volume for tracks with $\delta = 500, 750, 1000, 1250, 1500\mu m$ as per Equation 2.9a. The curves collapse on each other within the experimental error. Onset of bulge formation takes place at $\hat{V}_{res} = 1$ and $\hat{V} = 1$ . . . . .	41
12	Salient steps of surface preparation. (I) Uncoated substrate (aluminum, PET film or regular white paper). (II) Spray-coating of a $TiO_2$ -PMC aqueous suspension on the substrates. (III) Coated substrate, and SEM image (scale bar is $100\mu m$ ) of the coated surface showing the different length scales of the deposited nanoparticle composite coating. Combination of PMC and the roughness imparted by the $TiO_2$ particles renders the surface superhydrophobic (water beads). (IV) UV treatment of the superhydrophobic substrate through a patterned photomask (top) to form the superhydrophilic regions (bottom). Exposed regions turn superhydrophilic (S-philic) upon 30 minutes of exposure to UV, while the unexposed regions remain superhydrophobic (S-phobic). . . . .	49
13	(a) Time-lapsed images (top view) of liquid transport through the wedge-shaped superhydrophilic track on a horizontal Al-substrate. The white bar at the top denotes $10mm$ . (b) Morphology of the liquid bulge, approximated as an ellipsoid of finite footprint on the wedge-shaped superhydrophilic track, moving along the track; (c) origin of the driving capillary force on the liquid bulge. . . . .	52
14	(a) Arrangement for measurement of the capillary force $F_{cx}$ at the narrow end of the wedge at the onset of droplet motion. (b) Variation of $F_{cx}$ with the wedge angle $\alpha$ (error bar shows the standard deviation due to variability in droplet volume). . . . .	56

## LIST OF FIGURES (Continued)

<u>FIGURE</u>		<u>PAGE</u>
15	Transport of the liquid front and the liquid bulge along a wedge-shaped track with $\alpha = 3^\circ$ (see Figure 13a). (a) Distance $x$ from the dispensing location as a function of $t^{1/2}$ , and (b) velocity as a function of position along the track. Comparison of the experimental data (symbols) with the Washburn model for wetting behavior (continuous curves) is also made. The gray bar denotes the spatial region in which the bulge volume shape transformed to the spread-out rivulet shape. . . . .	58
16	Patterned Al substrate (a1) and mask (a2) used for demonstrating a multi-step functional surface device capable of performing pumpless liquid bridging and draining. Snapshots of events on the liquid bridge circuit: (b, b1) liquid bulges at the wider ends of tracks A and B just before a liquid bridging event; (c, c1) onset of liquid bridging, (d-f) progression of liquid bridge formation; (g-h) liquid bridge touches the end strip D of track C; (i-k) progression of liquid pumping along track C; (l) de-bridging over D at the end of pumping. Starting from the onset of the liquid bridge touching strip D (frame (g)) to the de-bridged state (frame (l)), this procedure achieves an average pumping rate of $357 \mu L s^{-1}$ . (b1)-(e1): End views of the bridge formation and growth events (top views in (b)-(e)) as seen from the downstream delivery side of the device.	63
17	(a) Elevated end view sequence displaying liquid bridging and draining on the design of Figure 16(a) applied on a horizontal paper substrate. (b) Collection of liquid on the bridge circuit on a horizontal transparency (PET) film substrate after pumping for (b1) 1 cycle ( $\sim 56 \mu L$ ), (b2) 4 cycles ( $\sim 226 \mu L$ ), (b3) 7 cycles ( $\sim 395 \mu L$ ), and (b4) 10 cycles ( $\sim 564 \mu L$ ). The liquid (water) is dyed for better visualization. . . . .	65
18	(a) Photomasking template for the droplet three-splitter design. (b) Time-lapsed snapshots of a complete cycle of droplet splitting on an Al substrate with 3 radially equispaced wedge tracks. The event achieves a collective average pumping rate of $157 L s^{-1}$ . . . . .	67
19	Transport of liquid up along an inclined superhydrophilic wedge-shaped track. (a) Snapshots of water (dyed for better visualization) moving up along a transparency (PET) film substrate to an elevation of $9 mm$ after: (a1) one drop ( $4.7 \mu L$ ), (a2) 5 drops ( $23.5 \mu L$ ), and (a3) 40 drops ( $188 \mu L$ ). (b) 25 droplets ( $117.5 \mu L$ ) were pumped up a height of $4 mm$ along an identical track on paper. (c) The photomasking template for the tracks used in (a) and (b). . . . .	69

## LIST OF FIGURES (Continued)

<u>FIGURE</u>		<u>PAGE</u>
20	Snapshots of liquid transport up an inclined plane through a $13^\circ$ upslope (height of $\sim 4$ mm) on a droplet bridging and draining circuit (inset at the top left corner) after dispensing $56.4 \mu L$ of liquid. Elevated end view (left column) and top view (right column), as taken from two distinct runs under the same conditions. The needle dispenser can be seen on the left of each top-view image. . . . .	71
21	Recent Studies on Enhanced Dropwise Condensation (DWC), as Classified on the Basis of the Working Fluid, Ambient Gas Environment, and Condensate Removal Approach . . . . .	78
22	Schematic of the sample-fabrication process. The protective polymer sheet on the aluminum substrate (as purchased) is laser cut using a precise CAD design (a) and then selectively peeled off, exposing selected regions of the aluminum underneath (b). (c) The substrate is subsequently exposed to selective chemical etching (in a 3 M HCl acid bath for 15 min), followed by passivation via boiling in water (1 h). (d) Finished sample with a wettability-patterned region after the polymer mask has been removed. The exposed region (wedge-shaped in this case) became superhydrophilic, while the rest of the sample remained hydrophilic (intrinsic wettability of aluminum) with $\theta \approx 78.2^\circ$ . The inset in (d) shows a scanning electron micrograph of the superhydrophilic triangle region. The scale bar in the inset denotes $100 \mu m$ . . . . .	80
23	Condensation experiment setup. Test samples are mounted on a computer-controlled Peltier cooler, which maintains the substrate surface temperature at a set point. The sample is exposed to controlled humidity and temperature in an environmental chamber. Droplet coalescence and shedding events are visualized through a heated (to prevent fogging) glass window (right) using high-speed photography. . . . .	83

## LIST OF FIGURES (Continued)

<u>FIGURE</u>		<u>PAGE</u>
24	<p>(a) Schematic of DWC on the wettability-patterned substrate. (b) Comparison of condensate drop size evolution with time on the patterned (left) and unpatterned (right) regions of the substrate. The patterned region featured equally spaced <math>800\ \mu\text{m}</math> wide mirror-finish (mildly philic) parallel stripes separated by <math>300\ \mu\text{m}</math> superhydrophilic (S-philic) tracks. The period between recorded images is <math>10\ \text{min}</math> (top to bottom). The unpatterned region exhibits a much greater droplet size than does the patterned region. The scale bar (black) denotes <math>3\ \text{mm}</math>. (c) The largest condensate droplet size (shown in different colors) depends on the location of initial nucleation (dark dots) on the mildly philic region. The closer the point of nucleation to the wettability contrast line, the smaller the size of the departing droplet (absorbed into the adjacent film covering the S-philic track).</p>	84
25	<p>(a) Typical dynamics of the capillary-driven motion of a drop placed across the wettability transition line (shown by the red arrow and dashed line) that separates the mirror-finish (A) and superhydrophilic (B) domains. The same mechanism affects condensate removal by capillary pumping along the superhydrophilic track. (b) A droplet growing (b1) on the hydrophilic DWC region (A) adjacent to a superhydrophilic track (B) eventually reaches the edge of the track (b2). Capillary pressure in the droplet pumps the liquid (b3, b4) rapidly into the adjacent liquid film occupying region B. The white scale bars in the top image denote <math>1\ \text{mm}</math> both in (a) and (b). (c) Relation between the theoretical maximum droplet diameter and the width <math>\lambda</math> of the hydrophilic track.</p>	88
26	<p>(a) Condensate removal induced by droplet coalescence. Two isolated neighboring droplets (frame a) grow on the hydrophilic region (A) until they touch and coalesce (frame b); inertia of the liquid in the coalescing droplets leads to lateral widening of the new droplet, which then touches the adjacent superhydrophilic (B) track. The liquid is then pumped into the superhydrophilic track by capillary pressure (frames c-f). The white scale bar denotes <math>1\ \text{mm}</math>. Images are captured every <math>5\ \text{ms}</math>. Yellow arrows indicate the direction of condensate flow. After the droplet is drained into the liquid film (f), the pristine surface left behind offers new sites for sustained nucleation.</p>	89

## LIST OF FIGURES (Continued)

<u>FIGURE</u>		<u>PAGE</u>
27	<p>(a) Droplets on patterned condensing surfaces comprising hydrophilic strips (A) of width <math>\lambda</math> interspaced by superhydrophilic tracks (<math>300 \mu m</math> wide in a1 and a2, <math>400 \mu m</math> wide in a3 and a4) (B). Region C denotes an unpatterned mirror-finish Al region (similar to A). The scale bar denotes <math>11 mm</math>. (b) Variation of the maximum droplet diameter (averaged over the hydrophilic strips of the patterned surface during a period of 30 min of steady condensation) with <math>\lambda</math>. The box plot presents the median, lower, and upper quartiles (25th and 75th percentiles, respectively) of the largest droplets recorded at 1 min intervals over the duration of each experiment. The black triangle represents the time-averaged value of the largest departing droplet diameter (<math>D_{max}</math>) over the same period. The dashed horizontal line represents the corresponding <math>D_{max}</math> for the unpatterned region (control surface). Each data point results from more than 150 measurements. . . . .</p>	91
28	<p>(a) Thermal resistance model of a condensate droplet under the water vapor + NCG condition (left) and representative temperature (T) and vapor mass fraction (<math>Y_w</math>) plots along the radius of the droplet (right).(b) Variation of the DWC heat transfer coefficient with the maximum departing droplet size following the Rose model and various values of <math>f = \Delta T_{bl}/\Delta T</math>, representing the extent of temperature difference occurring across the vapor + NCG boundary layer. The inset in (b) is a blowup over the range of droplet radii that can be controlled by wettability patterning. . . . .</p>	93
29	<p>Substrates with straight-line wettability patterns were tested in the condensation chamber for two different conditions, namely, C1 (<math>20^\circ C</math> DBT, <math>80\% RH</math>) (a1) and C2 (<math>35^\circ C</math> DBT, <math>80\% RH</math>) (b1). (a2, b2) Zoomed-in images of a1 and b1, respectively. The dimensions of the simple line design are marked in a2. A greater presence of water vapor in the atmosphere for b1 is substantiated visually by observing a greater number of droplets in b2 as compared to the number of droplets in a2. Red arrows in b2 show residual droplets after incomplete capillary pumping into the adjoining drainage routes. Scale bars in a1 and b1 denote <math>10 mm</math>. . . .</p>	101

## LIST OF FIGURES (Continued)

<u>FIGURE</u>		<u>PAGE</u>
30	<p>(a) Wedge-shaped superhydrophilic track aiding the pumpless transport of condensate from the narrow end to the wider end. The bulged puddle on the elliptic superhydrophilic well at the broad end of the wedge holds the condensate drained through this track. The area around the track is mildly hydrophilic and promotes DWC, as seen in this image. (b) Typical vein structure of a banana leaf. (c1) Condensation on an interdigitated wettability-patterned design inspired from the leaf vein network layout (image taken after 3 h of condensation under the same environmental conditions as in Figure 29a). The inset (c2) shows the condensate droplet distribution on the hydrophilic bands; one superhydrophilic tapered wedge track is highlighted in red; note the difference in droplet size in the two yellow-highlighted philic regions, which have different lateral widths. (c3) Key dimensions of the interdigitated design of the plate shown in c1. White scale bars denote 20 mm. All dimensions, except the wedge angle, in c3 are in millimeters. Image (b) was reprinted with permission from J. Brittin (<a href="http://www.jamesbrittin.com">www.jamesbrittin.com</a>). . . .</p>	103
31	<p>Bar graphs showing the relative improvement in condensation in terms of (a) condensate collection rate, and (b) latent heat transfer coefficient (HTC) for two different ambient environments for the unpatterned control case (bare Al), straight-line, and bioinspired interdigitated wettability patterns. Both patterned surfaces performed better than the control surface for 20 °C DBT 80% RH (C1) and 35 °C DBT 80% RH (C2) conditions. In the harsher situation (C2), the interdigitated pattern is more effective compared to the straight-line patterns. The improvement is solely attributed to the geometric shape of the wettability patterning of the substrate. . . . .</p>	105
32	<p>Two designs of periodically-patterned samples for condensation experiments. (a) Interdigitated design where the superhydrophilic tracks are arranged in-line on either side of the central drainage vein (base case), and (b) staggered design of the tracks. The latter facilitates more efficient drainage of the lateral wedge tracks into the vertical drainage vein. . . . .</p>	114
33	<p>(a) Example of an unpatterned condensing surface with 75% dropwise area (left) and 25% filmwise area (right). The scale bar (in white) denotes 10 mm. Variation of (b) water condensate collection rate, and (c) HTC with FWC area fraction (expressed as percentage of the total condensing surface). As FWC area ratio decreases, the corresponding DWC area ratio increases, thus enhancing heat transfer coefficient as well as water collection rates. . . . .</p>	116

## LIST OF FIGURES (Continued)

<u>FIGURE</u>		<u>PAGE</u>
34	Enhancement in (a) water collection rate, and (b) HTC for different FWC fractional areas under two distinct environmental conditions (Cases 1 and 2). For Case 1, the maximum enhancement in HTC is observed for FWC area of 29.9%. The maximum enhancement in HTC is $\sim 34.4\%$ and $\sim 30.5\%$ in water collection rate. For Case 2 (higher vapor content), the maximum enhancements in HTC (18%) and in water collection (15.4%) were observed for FWC fractional area of 35.9%. . . . .	122
35	Enhancement in (a) water collection rate, and (b) HTC for different FWC fractional areas under two distinct environmental conditions (Cases 1 and 2). For Case 1, the maximum enhancement in HTC is observed for FWC area of 29.9%. The maximum enhancement in HTC is $\sim 34.4\%$ and $\sim 30.5\%$ in water collection rate. For Case 2 (higher vapor content), the maximum enhancements in HTC ( $\sim 18\%$ ) and in water collection ( $\sim 15.4\%$ ) were observed for FWC fractional area of 35.9%. . . . .	123
36	Sessile droplets on the bare substrate (left) and superhydrophobic sections (right) of aluminum, paper and PET substrates. This figure shows one sample image for each substrate taken from several runs used to obtain the $\theta_e$ data. Each scale bar denotes 1 mm. . . . .	134
37	Image of the liquid accumulation on the inclined wedge track (a) just before $\beta$ reached the critical value below which the liquid bulge started moving up the plane, as shown in (b). (c) Variation of the capillary force on the droplet with droplet volume for different values of wedge angle $\alpha$ . Scale bar denotes 2 mm. . . . .	136
38	Image of the liquid accumulated after approximately 235 mL of water (dyed for better visualization) were dispensed at the left end of the track. Scale bar denotes 10 mm. . . . .	137
39	Effect of presuffusing on liquid mobility: for a dry track (top) the smaller surface features (characteristic dimension $d_{p,dry}$ ) limit the hemiwicking speed. For a presuffused track (bottom), the narrower crevices of the tracks are submerged, and the hemiwicking speed is limited by the relatively larger features ( $d_{p,wet}$ ) of the exposed surface roughness. . . . .	138
40	Velocity-time plot of the liquid bulge on a horizontal presuffused track with $\alpha = 3^\circ$ . . . . .	139

## LIST OF FIGURES (Continued)

<u>FIGURE</u>		<u>PAGE</u>
41	Growth of the capillary bridge thickness (normalized with $h_0$ , the initial bridge thickness) as measured from Figure 16(b1 - e1) as a function of time. The bridge height exhibits a linear dependence with $t^{1/2}$ (time scale is in milliseconds). . . . .	140
42	(a - b) Three-way droplet splitting on a paper substrate. (a1) The substrate, (a2) liquid accumulation after perfectly symmetric deposition of 5 drops ( $23.5 \mu L$ ) at the center, (a3) same, after 15 drops ( $70.5 \mu L$ ). (b) Biased accumulation after asymmetric splitting of 5 successively dispensed droplets. (c) Five-way droplet splitting on transparency (PET) film: (c1 - c3): sequence of the first droplet split, (c4) liquid accumulation after splitting of 10 droplets ( $47 \mu L$ ). Scale bars denote 5 mm. . .	141
43	Sessile water droplets on mirror-finish aluminum (left), superhydrophilic region (center), and mirror-finish aluminum priorly subjected to 6 hrs of DWC testing and left to dry. . . . .	143
44	Determination of $D_{max}$ . Five typical sample images showing the spatio-temporal evolution of condensate droplets on a patterned surface from the onset of DWC. The patterned region was divided in 6 equal strips of width $\lambda = 2000 \mu m$ (hydrophilic) separated by $400 \mu m$ wide superhydrophilic strips. The hydrophilic domains (strips) exhibited sustained DWC, while the superhydrophilic domains (tracks) remained covered in condensate films. A MATLAB code was used to identify the largest droplet in each hydrophilic strip at every time step. The red circles in frames 4 and 5 mark the largest droplet in each vertical strip; a similar exercise was performed for the earlier images. For each line pattern and the corresponding ambient conditions, $D_{max}$ was determined by averaging the maximum droplet diameter values for each strip and over all times. The white bar in the leftmost frame denotes 5 mm. . . . .	144
45	Snapshots of sustained DWC on the control surface after: (a) 30 minutes, and (b) 600 minutes from the inception of condensation under condition C1 (20C DBT, 80% RH, dew point $\sim 16.5 \text{ }^\circ C$ , substrate temperature $2.6 \pm 0.3 \text{ }^\circ C$ ). No visible transition from DWC to FWC was observed for the duration of the experiment. Note the difference in droplet sizes due to different phases in their surface rejuvenation cycle (nucleation-growth-departure-nucleation). Both scale bars denote 2 mm. . . . .	145

## LIST OF FIGURES (Continued)

<u>FIGURE</u>		<u>PAGE</u>
46	(a) Transport equations governing water vapor mass transport around a single condensate droplet, assuming spherically-symmetric transport over the hemispherical droplet in a quiescent environment. $F$ denotes the ratio of actual area of the spherical droplet exposed to the gas side to the total surface area of a sphere with the same diameter. Variations of (b) vapor-side temperature on the liquid surface, and (c) fractional temperature drop ( $f = \Delta T_{bl}/\Delta T$ ) with droplet radius for different vapor mass fluxes ( $j''$ in $kg\ m^{-2}\ s^{-1}$ ). . . . .	146
47	Step by step sequence of image processing. a) Raw image is cropped after identifying the track length from end to end. The origin (0, 0) for estimating height ( $h$ ) and length ( $x$ ) is set to at the lower left corner of the image. b) Image in (a) is processed and converted into binary format (black and white) for simplifying edge detection. A crisp edge at black and white intersection is detected, which is identical to the RAW image. Error is limited to $\pm 1$ px. c) The code scans every single rows and columns to detect the shift in color (from black to white) to isolate the edges. Black dashed lines traces the height of the liquid profile. Red lines demarcates the bulge boundary. . . . .	151
48	Copyright screen shot for Chapter 3 . . . . .	153
49	Copyright screen shot for Chapter 4 . . . . .	154
50	Parabolic curve fitting of the height of bulge volume using a second degree polynomial of $x$ . a) Shows the curve fitted data (red) overlapped on experimental data (black dashed). Plot for all the bulge volume for a single track width $\delta = 1000\ \mu m$ , $L = 50\ mm$ is shown. b) Corresponds to a single case where $V_{tot} = 70\ \mu L$ and track geometry similar to (a). .	155

## LIST OF ABBREVIATIONS

### Acronym

AC	Alternating current
ASSURED	Affordable, sensitive, specific , rapid, robust, equipment free, deliverable to user end
Ca	Capillary length
CA	Contact angle
CAD	Computer aided drawing
CAH	Contact angle hysteresis
CNF	Carbon nanofibers
DBT	Dry bulb temperature
DC	Direct current
DI	De ionised
DRie	Deep reactive ion etching
DSLR	Digital single lens reflex
DWC	Dropwise condensation
EWOD	Electrowetting on dielectric
FAS	Fluoroalkylsilane

## LIST OF ABBREVIATIONS (Continued)

FWC	Filmwise condensation
HCl	Hydrochloric acid
HR	Humidity ratio
HTC	Heat transfer coefficient
HVAC	Heating ventilation and air conditioning
NCG	Non condensible gases
OEW	Opto electric wetting
PDMS	Polydimethylsiloxane
PET	Polyethylene terephthalate
PFDTs	Perfluoro-decyltrichlorosilane
PMMA	Poly(methyl methacrylate)
POC	Point of care
RH	Relative humidity
STC	Surface tension confined
TAS	Total analytical system
UV	Ultra violet
WBT	Wet bulb temperature

## SUMMARY

Transporting liquid micro ( $\mu$ )-volumes in closed micro channels has been an active area of research for the last few decades and emerged as a new field known as *microfluidics*. The benefits of microfluidics are widely researched, published and implemented, primarily in the chemical and biological domains. However, confined flows inside closed channels and dependency on auxiliary equipment (pumps, power supplies etc.) limit application primarily to resource-hungry settings (read laboratory or research facilities in developed countries). Novel micro-nano fabrication techniques of functionalizing surfaces to tune liquid-solid interaction (wettability) has reinvigorated a 200 year old field, capillarity. Nanotechnology enabled us to conduct studies/experiments earlier deemed impossible. This further unlocked several novel liquid dynamics on surfaces. Pumpless liquid handling is one of the areas that has seen increased recent activity. This thesis is a step towards devising pumpless fluid management techniques on surfaces for transport of  $\mu$ -volume liquids.

As the name suggests, microfluidics deal with micro volume  $\sim O(1\mu L)$  liquid droplets. The length scale of such droplets are in general less than the capillary length  $\lambda_c$  of the particular liquid. As such, surface tension is dominant with negligible or no effect from gravity on the droplet. The general perception of pumping liquid is associated with an external mechanical device i.e. pump. However at smaller length scales, one can harness the capillary forces (due to surface tension) to transport liquid, eliminating the requirement of an external device or energy input. Capillary force is harnessed by tuning the interfacial forces between a solid and

## SUMMARY (Continued)

a liquid, thus controlling the interaction (wettability) of the liquid with the substrate using low-cost micro-nano fabrication and surface functionalization (coatings) technology. This field is called *wettability engineering*.

The initial part of the thesis explains the morphology of the liquid confined in wettability-patterned tracks, facilitating unidirectional spreading. The effect of liquid-gas interfacial surface area minimization in dictating the shape of the liquid is hypothesized and validated with experimental evidence. The second part of the thesis investigates how *surface tension force is harnessed to pumplessly transport liquids on open surfaces* culminating to a novel pumpless technique to transport liquids at very high velocities  $\sim O(100 \text{ mm/s})$  and flow rates  $\sim O(100\mu\text{L/s})$ . The technique is *substrate independent*. Simply, transporting liquid from point A to point B will not achieve any specific microfluidic tasks like merging, splitting, metering or mixing liquids as desired by real-world applications. Incompetence in complexly manipulating liquids for several microfluidic technologies reported in the scientific literature curbs their widespread use and practical implementation. Achieving such complex manipulation, that too without using any external device, poses significant challenge in design and fabrication. As such, the second part of the thesis addresses this issue by designing wettability-engineered substrates followed by demonstrating pumpless complex manipulation of liquids. It reports the first open surface pumpless droplet splitter, micro mixer, where substrates can be fabricated in less than 2 hours using a facile inexpensive technique.

Conventional microfluidics is primarily limited to biological applications with a very few implementations in other domains (chemical, heat transfer, etc.). Open-surface flow of  $\mu$ -

## SUMMARY (Continued)

volume liquids has the potential to usher several new application beyond lab-on-a-chip (LOC) and healthcare, such as enhanced heat transfer in condensation and boiling. The last part of the thesis focuses on non-trivial microfluidic application beyond lab-on-a-chip. It illustrates how pumpless transport of condensate on wettability-engineered heat transfer surfaces can remove droplets at small sizes  $\sim O(100\mu L)$ , eventually augmenting drop-wise condensation heat transfer. Effect of hydrophilic and hydrophobic area contribution on condensation heat transfer in an NCG (non condensable gas) environment is studied and quantified. The thesis ends with a future outlook of how pumpless fluid management can be explored in different areas and several challenges that need to be resolved.

## CHAPTER 1

### INTRODUCTION

#### 1.1 Background

The field of microfluidics has advanced by leaps and bounds since the early 1990s when Manz *et al.* first developed a miniaturized version of the total analytical system (TAS) with flow-through microfluidic channels(1). Owing to their high surface-to-volume ratio, such systems enable working with small quantities of samples and reagents with high spatio-temporal resolution and short processing times at reduced footprint and cost. These features make these systems highly suited for many biological, chemical and medical applications(2). Ensuring the appropriate flow of sample fluids and transport of reagents and analytes through these devices is a vital task, which has traditionally been achieved by several mechanisms(3), such as capillarity, pressure gradients, electrokinetic forces, centrifugal forces(4), acoustic forces(5) or magnetic forces(6). George Whitesides in 2006 in his seminal article about the future of microfluidics(2) concluded that *....much of the worlds technology requires the manipulation of fluids, and extending those manipulations to small volumes, with precise dynamic control over concentrations, while discovering and exploiting new phenomena occurring in fluids at the microscale level, must, ultimately, be very important.* Since then(7) there has been a tremendous amount of research done on engineering novel microfluidic and liquid manipulation technologies. Nonetheless, there still exist major pain points of conventional flow-through microfluidic

platforms, e.g. channel clogging by bubbles(8), fouling by debris(9), unwanted interaction of biological samples with channel walls, and non-specific surface adsorption that all need to be mitigated. Also, 3-D configuration of these devices requires expensive and elaborate fabrication processes (lithography(10), DRIe(11), micromachining(12) etc.) which are both time consuming and expensive. Most conventional microfluidic systems are based on closed-channel configurations, where microchannels are fabricated in a rigid substrate (e.g., silicon-based, glass, PMMA, etc.)(13) or soft elastomer poly(dimethylsiloxane) a.k.a. PDMS(14). In such systems, liquids flow at low Reynolds numbers. Besides, there are operational difficulties because of dependence on several off-chip components required for liquid transport (i.e. pumps, actuators, energy source for pumps etc.), which inhibits the possibility of using these devices at points of care with unskilled operators, especially in developing nations. **Surface microfluidics** is an emerging liquid-handling platform, and sub-genre of microfluidics. Unlike conventional flow-through microfluidic devices, their open-surface counterparts are meant for transporting and manipulating  $\mu$ -volume liquids on open substrates and not in a closed-channel configuration.

Manipulating small volumes of liquids on open surfaces offers several advantages over closed-channel systems; most of the common problems cited above for embedded microfluidic systems are dispelled by using surface microfluidic platforms, where the liquid is handled on a rigid or flexible(15), porous(16; 17) or impervious substrate, or even an immiscible liquid film(18). Surface microfluidic flow takes place at a length scale comparable to or less than the capillary length  $\lambda_c$  ( $\sim \sqrt{\frac{\gamma}{\rho g}}$ ); therefore surface tension can be harnessed as a dominating force for pumplessly (i.e., without any external energy input) actuating micro-volume liquids. Recent advancements

across the academic community and industry on surface coatings (19) have greatly facilitated tuning the interaction of liquids with surfaces. Facile microfabrication techniques have been developed for surface microfluidic platforms, bringing down the time and cost requirements for developing rapid prototypes. A typical PDMS-based microfluidic device takes a minimum of one day(13) for fabrication, provided all the steps (designing mask, fabrication of mask template, curing PDMS) are performed in house, which is not the norm in the majority of academic labs and points of need. On the contrary, a surface microfluidic device can be prototyped in less than 2 hours, from design to final product(15). This has stimulated renewed research interest in the microfluidics community towards exploring innovative and better lab-on-chip technologies, particularly for affordable healthcare solutions(20).

To date, the most widely used technique of complex liquid manipulation on surfaces for lab-on-chip applications is electrowetting on dielectric (EWOD). EWOD is not a passive mode of transport, as it relies on off-chip components. In an open-surface configuration, electrodes are patterned on primarily silicon wafer and covered with a dielectric and hydrophobic layer. Voltage (AC/DC) is applied from an external off-chip source to the electrodes, which locally creates a surface tension gradient, thus generating a net unbalanced force responsible for manipulating aqueous droplets. A detailed account of EWOD is provided by Nelson and Kim(21).

Generating liquid transport and controlled manipulation on surface microfluidic platforms without a pump or other on/off chip dependencies, has been the central challenge for a host of point of care (POC) devices. This thesis work is aimed to address some of the challenges. Surface tension-driven flow is a viable alternative of the aforementioned active transport strate-

gies. The concept is based on altering the local surface energy at different parts of the surface, so that a net unbalanced surface tension force ensues on any small liquid volume placed on the substrate. In order to influence the liquid/solid interactions and achieve controlled and pumpless liquid transport, several methods have been deployed, as discussed in the next section. A rapidly emerging, effective means of achieving this goal harnesses spatial domains of different wettabilities laid on a given surface. Engineering patterns of wettable and nonwettable regions on open surfaces, also known as *wettability patterning*, offers promise in designing passive surface-microfluidic devices, capable of not just transporting liquid without active power input, but also achieving complex fluidic tasks. Such surfaces comprise of juxtaposed regions of (super)hydrophilic and (super)hydrophobic domains that are separated by sharp wettability contrast lines. Liquids up to a critical volume, dispensed on the wettable domains can be kept confined by the wettability transition lines; the maximum liquid storage capacity of such a wettability-confined track depends on the track area and the contact angle ( $\theta_{Sphobic}$ ) of the surrounding hydrophobic region(22). By changing the shape (e.g., rectangular, triangular) of the hydrophilic area, one can fabricate surface tension confined (STC) tracks (23) to transport liquid or even self propel droplets(15), thereby achieving pumpless transport, a phenomenon elaborated in later chapters.

This thesis is intended to draw attention of broad microfluidics community to pumpless, liquid manipulation technique on solid surfaces. It summarizes the salient features of *wettability patterning* to achieve surface tension-driven transport of liquid droplets and their complex ma-

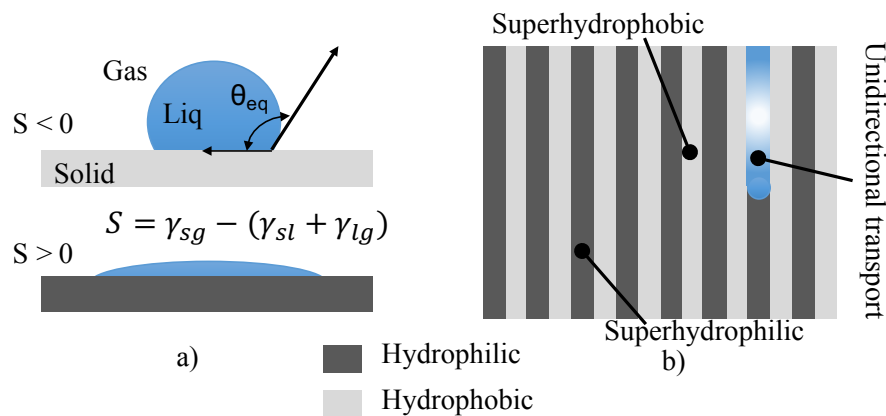


Figure 1. Schematic of a) spreading criterion of a liquid on a solid surface, b) directional transport of liquid along 2-D superhydrophilic tracks surrounded by superhydrophobic strips.

nipulations (e.g., droplet metering, merging, splitting, mixing, or even complex 3-D transport) on surface microfluidic platforms, without using any elaborate off-chip integration.

## 1.2 Capillarity and surface microfluidics

The simplest form of capillary transport of liquid on a solid surface is *spreading*. After a liquid droplet is deposited on a surface, the condition for spreading (or not) is defined by the spreading parameter  $S = \gamma_{sg} - (\gamma_{sl} + \gamma_{lg})$  (24), where  $\gamma_{lg}$  is the surface tension of the liquid,  $\gamma_{sg}$  is the solid-gas and  $\gamma_{ls}$  the solid-liquid interfacial surface energies. The liquid droplet spreads on the surface when  $S$  is positive, and it partially wets the surface for negative  $S$ . This tendency of the liquid to wet or partially wet a surface is attributed to minimization of the interfacial surface energy. Figure 1a shows a schematic of partial wetting and complete wetting of a liquid droplet on a solid surface in gaseous surroundings. At equilibrium, the interfacial energies

( $\gamma_{lg}$ ,  $\gamma_{sg}$  and  $\gamma_{sl}$ ) balance each other to dictate the shape of the drop as well as the contact angle that the liquid forms with the solid surface. The equilibrium contact angle  $\theta_{eq}$  is given by Young's equation;

$$\cos\theta_{eq} = (\gamma_{sg} - \gamma_{sl})/\gamma_{lg} \quad (1.1)$$

For homogeneous surfaces with  $S > 0$ , unrestrained spreading exhibits radial symmetry about the point of liquid deposition. This spreading may also be directed in a particular direction by guiding the liquid along a wettable (e.g., hydrophilic or superhydrophilic) track laid on a non-wettable (e.g., hydrophobic or superhydrophobic) background, as shown in Fig. Figure 1b.

Capillary forces arise as the system (liquid + substrate) attempts to attain the configuration of minimum energy. Such forces induce passive flow of the liquid, which can be broadly classified as *wicking or hemi-wicking*, or *Laplace-pressure driven*. Wicking is observed in a porous substance made up of a hydrophilic material. Liquid imbibes through the pores of the substrate during wicking, thus minimizing the total surface energy of the liquid-porous substrate systems (Figure 2a1). When a textured wettable surface is exposed to a wetting liquid, a film propagates through the crevices of the surface features without fully immersing the features (Figure 2a2). This phenomenon is known as hemi-wicking and differs from classical wicking where the liquid flows through capillary pores and not on the surface(25). The propagating liquid front in both wicking and hemi-wicking situations follows a  $x \sim t^{0.5}$  power law, which ensues by striking a

balance between the surface tension force and the resisting viscous force. Such spreading is more commonly known as Washburn spreading, since it is governed by the Washburn law:

$$x(t) = \sqrt{\frac{\gamma_{lg} r_{pore} t \cos \theta_{eq}}{2\mu}} \quad (1.2)$$

where  $x$  denotes the position of the front of the spreading liquid,  $t$  the duration of spreading,  $r_{pore}$  the hydraulic radius of the pores, and  $\mu$  the viscosity of the liquid. This model assumes uniform cylindrical pores, negligible gravitational effects, chemical homogeneity, and an unlimited reservoir volume (that supplies the spreading liquid)(26). It can be easily deduced from Equation 1.2 that the velocity of a hemi-wicking front decreases with time ( $\sim t^{-0.5}$ ). Several other spreading models have been proposed in the literature, taking into account the inertial, gravity, viscous and surface tension forces(27): the fundamental trend of decreasing spreading velocity with time persists for all models.

It is well known that the curvature of a droplet imposes a pressure discontinuity across the curved interface; this pressure jump is more commonly known as Laplace pressure and scales with the liquid surface tension  $\gamma$  as well as the local curvature  $\kappa$  ( $\sim \gamma\kappa \sim 2\gamma/r$ ). Figure 2b1 shows the schematic of liquid volumes placed on hydrophilic patches of diameter  $d$  and surrounded by a hydrophobic background. The wettability-confined droplets conform to different radii of curvature ( $R_{1,2,3,4}$ ), depending upon the liquid volumes and the patch diameter. The plot in Figure 2b2 shows how the Laplace pressure inside these drops varies with the droplet volume, considering negligible gravity (i.e. droplets smaller than capillary length),

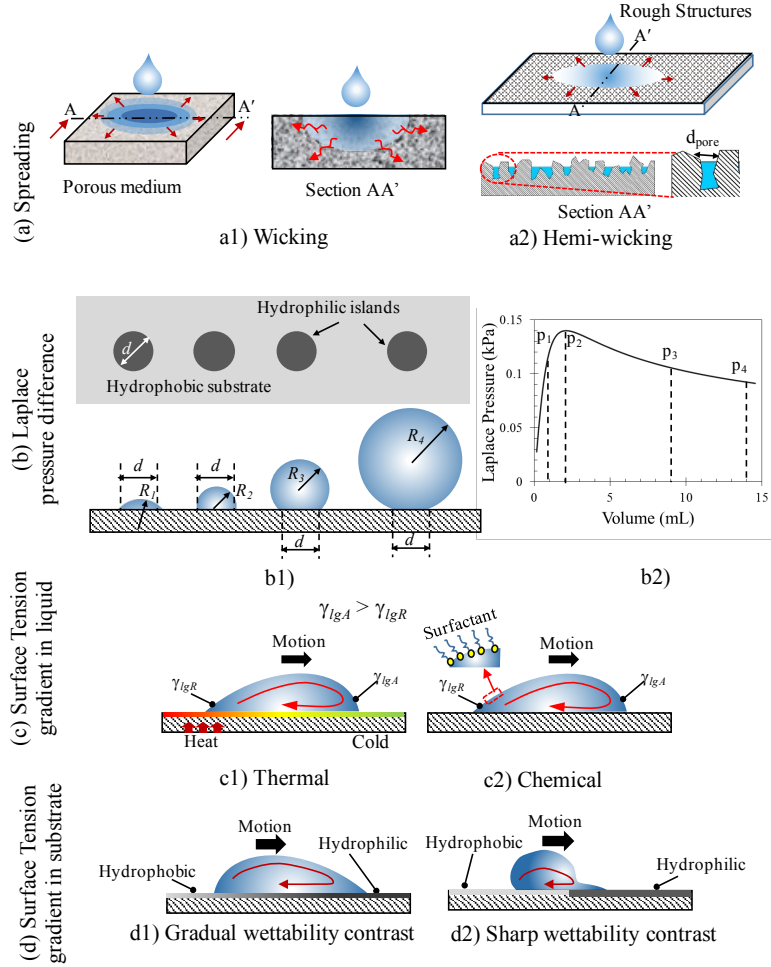


Figure 2. Pumpless liquid-transport mechanisms: a) Schematic showing spreading of a liquid droplet on a porous substrate (a1, classical wicking) and a solid impermeable substrate with micro-nano roughness structures (a2, hemi-wicking). For both cases, spreading distance varies as  $x \sim t^{0.5}$ . b) Tuning the curvature of liquid droplet to vary the Laplace pressure. (b1) Circular hydrophilic patches of diameter  $d$ , surrounded by a hydrophobic background confine liquid droplets of different volumes. The radius of curvature for each case is different, although the hydrophilic patch area is the same. This causes a variable Laplace pressure, which scales with the curvature of the droplet. (b2) Representative plot showing how Laplace pressure changes with liquid volume on a hydrophilic disk of constant diameter. c) Thermal (c1) and chemical (c2) surface tension gradients in a liquid volume promote fluid actuation. In (c1), a temperature gradient on the substrate changes the local surface tension at the advancing (right) and receding (left) end of the liquid volume. (c2) represents how surfactants can alter local surface tension chemically, hence mobilizing the droplet by the differential capillary force between the advancing (right) and receding (left) fronts.  $\gamma_{lgR}$  and  $\gamma_{lgA}$  denote the liquid surface tension at the receding and advancing end, respectively. d) Droplet actuation by patterning the wettability of the substrate. (d1) Substrate with spatially-gradual wettability changes. The droplet moves from the hydrophobic to the hydrophilic region. (d2) Droplet actuation by a wettability step. The property of the substrate suddenly shifts from hydrophobic (left) to hydrophilic (right). Note the difference in shape of the droplet at the onset of transport.

$d = 2$  mm and  $\gamma_{lg} = 0.07$  N/m (water). Clearly, the highest Laplace pressure corresponds to the case where the droplet radius of curvature  $R$  is minimum (case 2). Implementing this principle, when two liquid volumes of unequal curvature are connected by a wettable track on a substrate, liquid from the volume with the smaller radius (not necessarily the smaller volume) will be transported to the volume with larger radius by virtue of the Laplace pressure difference(28). Typical volume flow rate attained with this mechanism is of  $\sim O(0.1\text{ml}/h)$  and the time scales of transport are of  $\sim O(10s)$ .

Laplace pressure driven flow can also occur by artificially creating spatial non-homogeneity of local surface energy of the sessile liquid, or the underlying solid substrate. Broadly classifying, there are two major techniques of tuning the Laplace pressure of a liquid drop: 1) *by inducing surface tension gradient in the liquid* (see Figure 2c), and 2) *by inducing surface energy gradient on the substrate* (see Figure 2d). In the first case, surface tension of the liquid on the liquid-gas interface is tuned by creating a chemical(29) or thermal(30) gradient, thus inducing Marangoni stresses. For the second case, the local surface energy of the substrate may be altered by creating a gradient of surface energy(31) or fabricating contrast wettability-patterned tracks(23) of varied geometry. The subsequent section talks about the recent advances in transport mechanisms on surfaces and the challenges that need to be overcome.

### **1.3 Recent advances**

*Wicking:* The earliest elements of pumpless surface microfluidics were demonstrated by the Whitesides group and relied on the wicking properties of paper. Although wicking in paper and fibrous assemblies (e.g. fabrics) has been explored for centuries, its application in surface

microfluidics was not reported until 2007 when Martinez *et al.*(32) demonstrated the capability of wicking tracks on paper to transport liquids specifically for microfluidic applications. They reported the fabrication and operation of a paper-based microfluidic device that was capable of performing several lab-on-chip tasks. The treated paper unidirectionally wicked the liquid from a pseudo-infinite reservoir. The basic principle was to confine the liquid on paper (intrinsically hydrophilic) by selectively depositing hydrophobic wax on the surrounding areas either by photolithographic technique or using a desk-jet printer. Their device conformed to the World Health Organization’s ASSURED (Affordable, Sensitive, Specific, User-friendly, Rapid and robust, Equipment free and Deliverable to end user) standard for diagnostic devices intended for developing countries. Paper-based microfluidic devices relying on wicking for transport are competent to perform several low-cost biological and chemical diagnostics. The liquid transport is laminar and can be approximated as a Washburn type flow. The wicking-based transport mechanism, however, has a major limitation in terms of transport speeds. A simple scaling analysis using Equation 1.2 indicates that on a rough surface having an average  $r_{pore} \sim 0.1 - 1\mu m$ , a liquid droplet (e.g., water,  $\mu \sim 0.001 Pas$ ,  $\gamma = 72 mN/m$ ) would take  $O(\sim 10 - 100s)$  to get transported by hemiwicking over a distance of  $O(\sim 1cm)$ . In most paper-based microfluidic devices, contrast wettability patterning has been used to confine the liquid and transport it by wicking in a specific direction. Besides paper, wicking-based pumpless transport was recently explored on woven fabrics as well(33). On fabric-based wicking devices, threads of different wettability are interweaved to directionally transport liquid. Figure 3 shows some examples of wicking-based liquid transport, performing several lab-on-chip tasks. There are several chal-

allenges of wicking based pumpless transport and the three major ones are: 1) slow transport speeds, 2) loss of reagent/chemical in porous substrates and 3) in ability to perform complex liquid manipulation.

*Laplace pressure driven transport:* As mentioned in the previous section, this transport mechanism relies on tuning the local curvature of the liquid by imposing a surface energy gradient in the liquid or the substrate underneath the liquid; the latter may be achieved by varying the local wettability of the substrate either gradually (gradient wettability), or sharply (contrast wettability).

Cira *et al.*(29) observed that evaporation from a two-component, miscible-liquid mixture created spatial heterogeneity in liquid surface tension, thus leading to spontaneous liquid transport. When such droplets were deposited on glass, evaporation from one droplet altered the liquid-to-gas surface tension in the vicinity, thus affecting the mobility of a neighboring droplet. Figure Figure 4a shows two unequally evaporating liquid droplets (water and propylene glycol-PG) with different surface tension values (water  $\sim 72 \text{ mN/m}$ , propylene glycol  $\sim 45.6 \text{ mN/m}$ ) that develop Marangoni stresses, which in turn propel the droplets. Just like chemical surface gradients, temperature gradients locally alter the surface tension from the leading to the trailing edges of the droplet, thus creating an unbalanced capillary force. For example, surface tension of water at  $20 \text{ }^\circ\text{C}$  is  $\sim 72 \text{ mN/m}$ , whereas at  $90 \text{ }^\circ\text{C}$  it is  $\sim 60 \text{ mN/m}$ . This phenomenon was explored by Darhuber *et al.*(34) in fabricating a thermocapillary microfluidic droplet actuator, which relied on integrated microheater arrays to control the substrate temperature with high spatial resolution (Figure 4b). Chakraborty *et al.*(30) exposed a chemical wettability

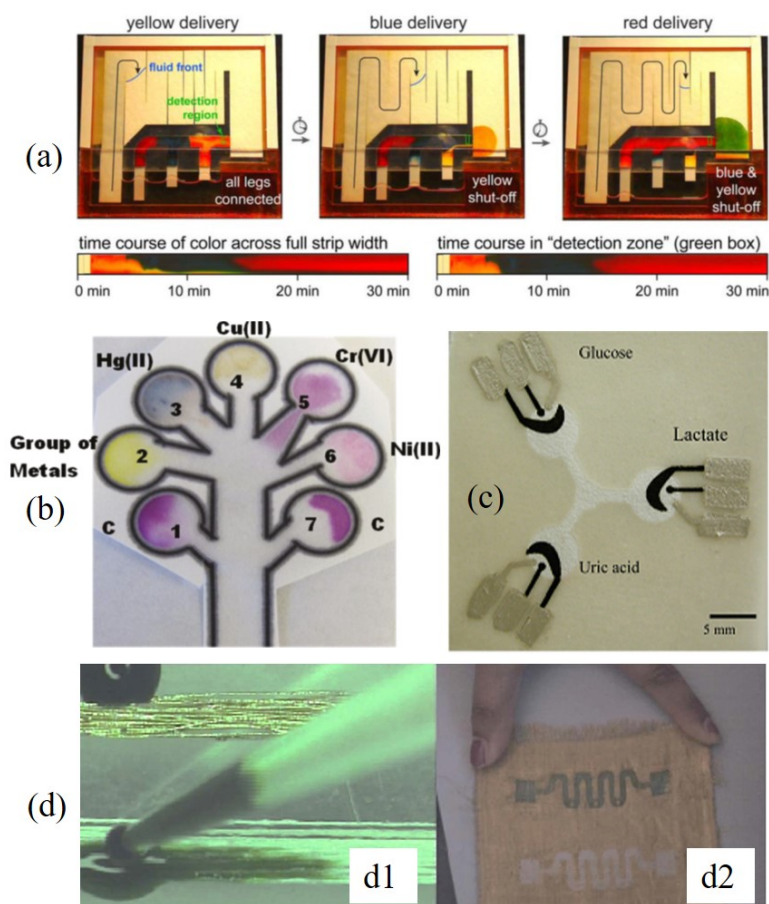


Figure 3. Examples of wicking flow: a) Automated sequential fluid delivery in a 2D paper network. Each leg wicked fluid from a single buffer source, and dried dyes representing reagents created different fluids from each leg (colours). Each coloured fluid arrived at a different time at the detection zone (green box) and was shut off in a timed sequence after delivery. (Below) Time courses show colour across the full strip width or the detection zone as a function of time after device activation. Reproduced from Lutz et al. 2013 with permission from The Royal Society of Chemistry. b) Detection of individual heavy metals from a water sample using a multiplexed bioactive paper sensor. The aqueous sample containing Hg(II), Cu(II), Cr(VI), and Ni(II) was added to the circular regions of assay zones with markers for identifying individual elements. Reprinted with permission from Hossain et al. Copyright (2011) American Chemical Society. c) Electro-chemical detection on a three-electrode paper-fluidic device. The hydrophilic area at the center of the device wicked sample into the three separate test zones. Reproduced from Li et al. with permission from American Institute of Physics (Biomicrofluidics), Copyright 2012 d1) Brass-coated yarn (top) rejected a drop of aqueous dye deposited on it, while degummed, surfactant-treated silk yarn (lower) allowed the fluid to wick along its length. d2) A fabric chip showing proof of concept for selective wetting. Aqueous green dye solution deposited at one end flowed only along the hydrophilic yarns. An unused chip (white) is shown for contrast. Reproduced from Choudhary et al. 2015 with permission from The Royal Society of Chemistry.

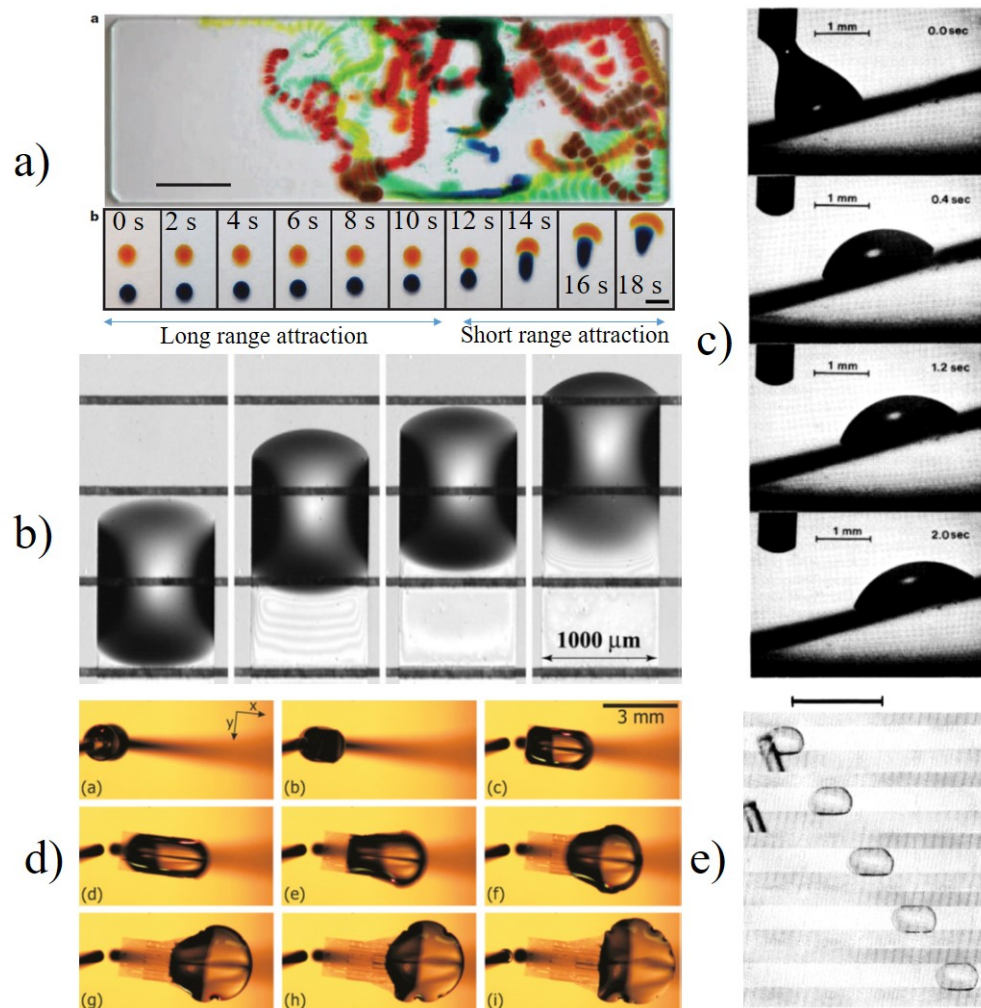


Figure 4. a) Long-range and short-range chemical interactions of two-component droplets, leading to spontaneous motion. (Top) Overlaid timelapse image of multiple coloured droplets deposited on a clean glass slide, interacting autonomously for 2 mins. Scale bar denotes 10mm. (Bottom) Two  $0.5 \mu\text{L}$  droplets of 25% PG in water (blue) and 1% PG in water (orange) interacting. The behaviour can be divided into long-range attraction and short-range chasing portions. Scale bar denotes 3mm. Adapted by permission from Macmillan Publishers Ltd: [Nature] Cira et al. copyright (2015) b) Droplet of PDMS moving along a heater array by thermo-capillary actuation. A thin residue trailed the wetting droplet. The image sequence represents times  $t = 0\text{s}, 44\text{s}, 88\text{s}$  and  $132\text{s}$ . Reproduced with permission from Journal of Microelectromechanical Systems, Copyright (2003) IEEE, DOI:10.1109/JMEMS.2003.820267. Darhuber et al. c) Uphill motion of a  $1 \mu\text{L}$  drop on a surface-tension-gradient surface inclined at an angle  $15^\circ$ . Reprinted with permission from Science, Copyright 1992, AAAS. Chaudhury and Whitesides 1992 d) Motion of a  $2 \mu\text{L}$  glycerol/water droplet on a pattern with varying fraction of hydrophilic-to-total area of the plate. Radius of input droplet is  $0.78\text{ mm}$ . Reprinted with permission from Bliznyuk et al.. Copyright (2011) American Chemical Society. e) Top views of free running droplets on a track delimited by hydrophobic regions. Time interval between two consecutive frames is  $0.1\text{ s}$  and the scale bar is  $1\text{ cm}$ . Reprinted with permission from Santos et al. Copyright (1995) American Physical Society.

gradient surface to elevated temperatures and reported that the droplet movement intensity increased with temperature differences on the substrate. The combined effect of chemically-induced Marangoni stresses with thermocapillarity was shown to propel droplets with velocities as high as  $\sim 40$  mm/s, which is significantly higher than the transport speed ( $\sim 1$ mm/s) due to thermocapillary action alone(35). Chakraborty *et al.*(30) also used significantly lower thermal gradient ( $0.08 - 0.20$  /mm), which lowered the energy requirement. Although this mechanism requires an active component (external energy supply), the ability to operate at low voltages makes this technique a convenient alternative for manipulating droplets. A combination of bi-component droplet and thermocapillary actuation was explored by Zhao *et al.*(35). They concluded that by coating an aqueous droplet with a long-chain alcohol (heptanol in this case), one could thermally mobilize the droplet on a hydrophobic surface. By applying a thermal gradient to this two-component system, the alcohol evaporated at different rates towards the front and the back of the droplet, creating a thermocapillary force, which eventually mobilized the droplet. Transport velocities were of  $\sim O(0.1$  mm/s) for the binary droplet and transport distances were limited to  $\sim 1$  mm. Linke *et al.*(36) harnessed the Leidenfrost effect(37) on a heated ratchet surface to self propel droplets. This self-propelling effect was further studied by Lagubeau *et al.*(38) who explained that the vapor escaping below the levitating Leidenfrost droplet provided a thrust due to the presence of asymmetric ratchet like structures. Droplet velocities of  $\sim O(10$ cm/s) were reported. Although the above transport mechanism is pumpless, for this particular case, the capillary force is not dominant. It is the viscous force exerted

by the vapor flow between the droplet and the underlying ratchet substrate that induces the droplet movement(36).

Chaudhury *et al.* (31) in a seminal study reported a novel technique of harnessing *surface energy gradients* to propel liquid droplets pumplessly on a surface. They achieved spatially-varying wettability on a silicon wafer through unequal deposition of a hydrophobizing silane vapor. The surface energy gradient of the substrate, thus established, resulted in an unbalanced Young's force on the droplet, thus actuating the liquid. Figure 4c shows such movement, where the droplet moves  $\sim 2mm$  in 2 seconds. Bliznyuk *et al.*(39) took an interesting approach in fabricating a stripe-patterned gradient surface to transport liquid droplets. They fabricated substrates with alternate hydrophilic and hydrophobic stripes and varied their relative width in such a way that the effective fraction of hydrophilic-to-total area increased on the plate. Figure 4d shows a glycerol droplet moving on striped silicon wafer (hydrophilic) patterned with 1H, 1H, 2H, 2H-perfluoro-decyltrichlorosilane/PFDTS (hydrophobic). Santos and Ondarçuhu(40) demonstrated that by depositing droplets of n-alkanes containing chlorosilane on glass (hydrophilic), the trailing end of the droplet released a thin chlorosilane film, which subsequently rendered the glass substrate hydrophobic. This created an unbalanced capillary force giving rise to *free-running droplets* (See Figure 4e) moving with velocities of  $\sim O(1cm/s)$ . Zorba *et al.* used a femtosecond laser-based technique to alter wettability (contact angles in the range  $66^\circ - 107^\circ$ ) of silicon by physical texturing only, without using any sort of chemical functionalization of the surface(41). Several other research groups(42; 43; 44; 45) used variants of the

above techniques of chemical patterning and physical texturing of substrates also to achieve pumpless liquid transport.

In this thesis, contrast *wettability-patterned substrates* have been used to induce rapid pumpless transport. The major difference between the transport mechanisms on surfaces with gradient wettability and contrast wettability is that, for the former there is a spatially gradual change in the surface energy of the substrate, whereas for the latter, there is a step change of surface energy from one domain to the other along a wettability transition line. Such wettability contrast lines may be appropriately used to confine the liquid strategically. Confining the liquid is important, since confinement restricts the intrinsic tendency to spread radially and instead imparts a directionality to the flow. Dahruber *et al.*(46) patterned the substrate with alternate lyophobic (liquid repelling) and lyophilic (liquid loving) tracks to confine the liquid on the latter. Liquid transport demonstrated by researchers on wettability-patterned surfaces has harnessed hemi-wicking. Schutzius *et al.*(23) fabricated anisotropic wetting patterns on a superoleophobic surface (fluoroacrylic copolymer + carbon nanofibers-CNF) using wettable paraffin wax. The liquid meniscus exhibited Washburn-type transport, recording velocities up to 3.1 *cm/s*. Their facile and top-down patterning approach provided promise for pumpless handling of low-surface-tension liquids. A versatile surface-microfluidic platform, comprising of a wedge-shaped superhydrophilic track laid on a superhydrophobic background has been developed. The approach harnessed Laplace-pressure gradients to induce rapid liquid flow along the track. When a  $\mu$ -volume liquid droplet was deposited at the narrow end of the track, it traversed towards the wider end, pumplessly (See Chapter 3).

## 1.4 Thesis objective

The primary objective of this thesis is to design, fabricate and develop an understanding of pumpless  $\mu$ -volume liquid transport mechanisms on surfaces, and extend application of microfluidics beyond lab on chip. As such, the following objectives are set:

### 1.4.1 Describing liquid behavior on wettability-patterned tracks

1. Study the shape evolution of liquid with volume on wettability-patterned surfaces.
2. Identify design parameters for pumpless liquid transport.

### 1.4.2 Demonstrating pumpless transport of liquid by harnessing Laplace pressure gradient on wettability-patterned substrates

1. Design and generate a polymer-nano composite solution to impart superhydrophobicity to disposable surfaces like plastic, paper, etc. Carefully choose a co-solvent which is compatible with all the materials of the substrates.
2. Develop a method to selectively change wettability of a surface. The challenge is to find a nano particle type that can both impart superhydrophobicity and aid in achieving superhydrophilicity.
3. Perform pumpless transport experiments of liquids by inducing Laplace pressure gradient on liquids dispensed on such surfaces.
4. Demonstrate facile fabrication and multi-functionality capability of the surfaces for potential applications for lab on a chip.

### **1.4.3 Demonstrate applications beyond lab-on-a-chip**

1. Based on understanding from the above objectives, design and fabricate a material system for wettability-patterned metal surfaces suitable for condensation heat transfer.
2. Design an experiment to study heat transfer characteristics of wettability patterned surfaces under controlled environment.
3. Employ iterative measures to refine the pattern designs for optimum heat transfer.
4. Perform a parametric study of primary influencing parameters in wettability-patterned substrates for enhanced dropwise condensation.

### **1.5 Scope of the work**

The goal of the thesis is to integrate facile platforms to make multifunctional microfluidic tools performing biological, chemical, and physical tasks towards next-generation POC diagnostic devices and applications beyond lab-on-chip. The primary scope of the thesis is to devise a novel material-independent method to manipulate liquids on surfaces for a variety of applications. As such, two different material systems were chosen to specifically demonstrate non-isothermal and isothermal applications where pumpless liquid transport can benefit or alleviate some existing pain points. Similar wettability patterns can be fabricated with countless methods as reported in the literature. The novelty of the work lies in the pattern designs. To the best of the author's knowledge, one of the key challenges in the microfluidics community is that there doesn't exist a truly point-of-care fluid management system that is facile to fabricate, inexpensive, allows fool-proof operation and not fully dependent on off-chip components.

Thus devising a pumpless mechanism is one of the major scopes this thesis addressed. Chapter 2 on the other hand talks about the shape evolution of liquids on wettability-patterned substrates. Understanding the complex shape on such tracks is crucial, since capillary forces at low Bond number is dominating which in turn depends on the geometry of the liquid. This forms a design guideline for building several devices performing microfluidic tasks. In Chapter 3, a suitable polymer nano composite solution dispersed in a substrate compatible solvent is designed, deposited and the substrates are characterized. Selective UV treatment rendered wettability-patterned surfaces. Several designs and arrangements of the superhydrophilic tracks carrying liquids are studied to achieve complex liquid manipulation. Chapters 4 and 5 are focused on demonstrating the role of surface microfluidics beyond lab on a chip. Phase change heat transfer is an effective means of transporting unwanted heat in several industrial applications (power plants, chemical industries, electronics cooling, etc.) Especially for dropwise condensation, size and interaction of liquids formed on a substrate play significant role in enhancing or decreasing heat transfer efficiency. Thus, the heat transfer augmenting capability of pumpless liquid transport surfaces is studied. Finally, the thesis ends with some conclusions and suggested future studies/experiments to fully understand the limitations of the approach and identify wider applications.

## CHAPTER 2

### SHAPE OF LIQUID ON WETTABILITY-PATTERNED TRACKS

#### 2.1 Introduction

A liquid droplet deposited on a surface spreads radially in all directions(47). To arrest this radial spread, one needs to confine the liquid to a desired path. Wettability-engineered surfaces gives us the ability to design tracks, pathways(23; 15) where such liquids can be confined and transported unidirectionally. Interesting droplet morphologies are observed when liquid is deposited in those tracks(22; 48). A volume of liquid deposited on a track with high aspect ratio (length:width  $\gg 1$ ) undergoes a shape instability at a critical deposited volume. When liquid is deposited on a rectangular lyophilic track surrounded by a lyophobic domain (a.k.a wettability patterned), it changes from a constant cross section morphology to a complex shape partly consisting of a bulk liquid (bulge) and the remaining liquid exhibiting a constant cross section (residual). Gau and Herminghaus (22) modelled this instability of liquid on a lyophobic strip with a series of droplets which can exchange volume amongst themselves while conserving the total volume. They have theoretically concluded that the liquid shifts its morphology when the apparent contact angle of the liquid at the lyophobic-lyophilic interface attains to  $90^\circ$ . The mean liquid curvature is maximum at this state and minimizes the total interfacial surface energy. Lipowski and his co-authors further performed a series of theoretical studies (49) in understanding the morphology of liquid on wettability-patterned domains. The combined

conclusion of interest from the above works for a liquid volume on a wettable strip confined by a non-wettable domain is that *the liquid volume shape transitions to a bulge and cylindrical morphology beyond a critical volume*. Our experimental observations validate the hypothesis as described later in the text. However, prior studies does not throw any light on the distribution of total volume into bulge and residual volume beyond the transition. Knowing the volume distribution is important from the point of achieving passive liquid manipulation on surfaces and designing novel microfluidic devices(15).

We conducted a series of experiments on rectangular superhydrophilic tracks (varying track width  $\delta$ ) surrounded by superhydrophobic domain. Volumes of droplets ranging from  $5 \mu L$  to  $200 \mu L$  are deposited on the tracks. For all the cases, as expected the liquid exhibited the bulge morphology beyond a critical total input volume ( $V_{cr}$ ). The greater the width of the tracks, the higher is the critical volume of bulge formation. Normalizing the residual volume ( $V_{res}$ ) with the critical volume ( $V_{cr}$ ) nicely collapses the data for all our experiments as described later in this chapter.

## **2.2 Experiment**

*Sample Preparation:* Aluminum metal sheets (60601, McMaster, 2 mm thick) are first acid etched in 3 molar hydrochloric acid (HCl) solution. The acid etches the aluminum metal and attacks the grain size of the metal. This renders the substrate with micro structures(50). Further boiling the etched sample in water initiates the growth of Boehmite structures (51) imparting a nanoscale roughness ( $\sim O(100nm)$ ) to the substrates. On coating the micro-nano scale roughened aluminum substrate with fluoro alkyl silanes (FAS), the substrate becomes

superhydrophobic. To fabricate the superhydrophilic tracks, the substrate is selectively exposed to a laser (Scorpion Rapide, 20 W), where the laser beam followed a CAD design to raster the region of interest. The superhydrophilic track exhibits a water contact angle of  $0^\circ$  whereas for the superhydrophobic background the contact angle is  $\sim 155 \pm 3^\circ$ .

*Image processing:* A digital camera is used to capture the steady state of the droplet shape on 5 tracks of varying width ( $\delta \sim 500 \mu m, 750 \mu m, 1000 \mu m, 1250 \mu m$  and  $1500 \mu m$ ) and constant length ( $L = 50 mm$ ). Once a droplet is deposited on the track, images are captured after waiting for 60 seconds for the liquid volume to stabilize. Longer wait was avoided to prevent evaporation-loss induced errors. The captured images are further processed and analyzed using a custom made MATLAB code. The details of the processing algorithm are explained in APPENDIX C.

### **2.3 Theory and modeling**

In a rectangular superhydrophilic track geometrically defined by constant local width  $\delta$  and length  $L$ , for a static situation, the input volume ( $V_{tot}$ ) either takes the shape of part of a truncated cylinder (configuration 1 or C1) or a complex shape comprising part of a cylinder as well as a bulge volume (configuration 2 or C2). Figure 5 shows the track geometry and the two configurations 1 & 2 of the liquid on the track. In the absence of the bulge, the liquid conforms to the shape of a cylindrical sector. See Figure 5b. Clearly from Figure 5c the droplet conforms to a complex shape (Configuration 2) which can be broadly identified as the bulge volume ( $V_{bul}$ ) and the residual volume ( $V_{res}$ ). The shape of  $V_{bul}$  can be approximated to a surface profile which follows a parabolic equation (of the form  $\sim ax^2 + bx + c$ ) and  $V_{res}$  is

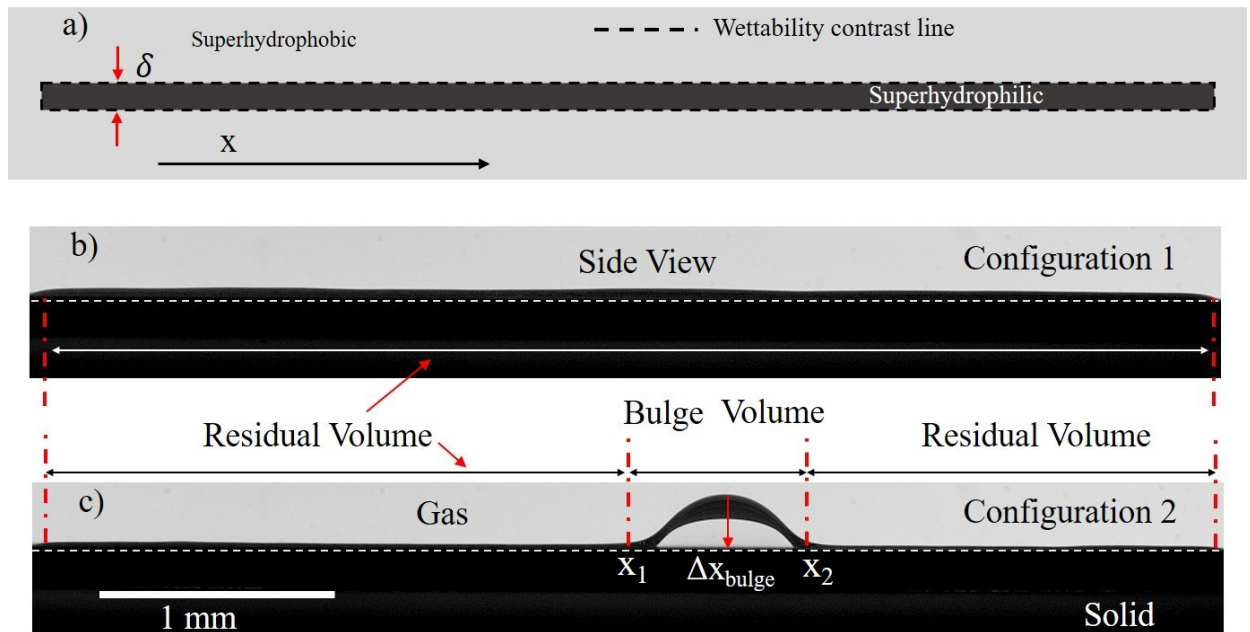


Figure 5. a) Schematic drawing of a typical superhydrophilic rectangular track of length  $L$  and constant width  $\delta$ , surrounded by a superhydrophobic domain. b and c) Side views from experiment: Static liquid volume shape. (b) Configuration 1, liquid in the shape of a cylindrical sector. (c) Configuration 2, liquid in the shape of cylindrical sector plus bulge. Dotted white lines in (b) and (c) show the surface of the underlying metal plate and define the datum line  $h = 0$  for liquid height.

identical to configuration 1 over reduced length  $(L - \Delta x_{bul})$ , where  $L$  is the total length of the track and  $\Delta x_{bul}$  is the length of the bulge.

This transition from C1 to C2 is governed by surface energy minimization. The liquid has the tendency to minimize the interfacial surface energy ( $E_\gamma$ ) among the three phases: solid (S), liquid (L) and gas (G).  $E_\gamma$  is given by Equation 2.1.

$$E_\gamma = \gamma_{LS}A_{LS} + \gamma_{LG}A_{LG} + \gamma_{SG}A_{SG} \quad (2.1)$$

where  $\gamma_{LS}$ ,  $\gamma_{LG}$ ,  $\gamma_{SG}$  and  $A_{LS}$ ,  $A_{LG}$ ,  $A_{SG}$  are the interfacial surface tensions and the interfacial surface areas, respectively of two of the phases (SG, LS, LG) at a time. As we deposit more liquid on the tracks i.e. as volume increases, the surface tension values ( $\gamma_{LS}$ ,  $\gamma_{LG}$ ,  $\gamma_{SG}$ ) are unchanged (assuming uniform environment, constant temperature of substrate and liquid, negligible contaminant absorption from atmosphere).  $A_{LS}$  is constant, since the superhydrophilic track is wet as we add more and more volume and the wetting area does not change as long as the liquid contact line is pinned at the wettability-contrast line. The track is always wet, hence the solid-gas interface does not exist, i.e.  $A_{SG} = 0$ . The only factor that change with the increasing volume is the liquid-gas (LG) interfacial surface area ( $A_{LG}$ ). Thus, Equation 2.1 reduces to Equation 2.2;

$$E_\gamma = \text{constant} + \gamma_{LG}A_{LG} + 0 \quad (2.2)$$

Thus, to understand the variability of net interfacial surface energy, it is pertinent to investigate how the surface area ( $A_{LG}$ ) evolves with the dispensed liquid volume ( $V_{tot}$ ). First, we conduct a series of experiments on different track geometries (varying track width  $\delta$ ) and then use image analysis algorithms to track the governing parameters (residual volume, bulge

volume, residual height, maximum bulge height, critical volume, critical height). Further, a semi-analytical model is proposed to explain the shape evolution of the liquid volume on the track.

### 2.3.1 Model: $A_{LG}$ for configuration C1 and C2

The major question we are trying to address is how the interfacial surface area ( $A_{LG}$ ) of a liquid volume ( $V_{tot}$ ) on a rectangular superhydrophilic track (length  $L$ , width  $\delta$ ) varies with increasing volume and at what critical volume ( $V_{cr}$ ), the transition from C1 to C2 will take place. The constant mean curvature of the liquid-gas interfacial area ( $A_{LG}$ ) is not available explicitly from the experiments. Due to the complicated nature of the liquid shape, the total liquid volume is assumed to be segregated into two simple volumes, a segment of a cylinder (residual volume, C1) and bulge section with a parabolic side profile (bulge volume, C2).

*Configuration 1:* Let us consider a cylindrical sector of height  $h(x)$ , cross sectional radius  $R(x)$  and length  $L$ ; see Figure 6a. The cylinder is constricted on the horizontal direction by track width  $\delta$  and ends of the track of length  $L$ . With increasing volume  $V_{tot}$ , the only way the track can accommodate additional liquid is to increase the height  $h(x)$  and the apparent contact angle  $\theta(x)$ , Figure 6b. Considering an elemental cylindrical segment of length  $dx$  with height  $h(x)$  and a circular cross section (Bond Number  $Bo \sim O(0.1) < 1$ , where  $Bo = \frac{\rho g l^2}{\gamma}$  and  $\rho = 1000 \text{ kg/m}^3$ ,  $g = 9.8 \text{ m/s}^2$ ,  $l = 1 \text{ mm}$ ,  $\gamma = 72 \text{ mN/m}$ , all values for water at room temperature), then for that segment the radius is given by:

$$R(x) = \frac{(\delta/2)^2 + h^2(x)}{2h(x)} \quad (2.3)$$

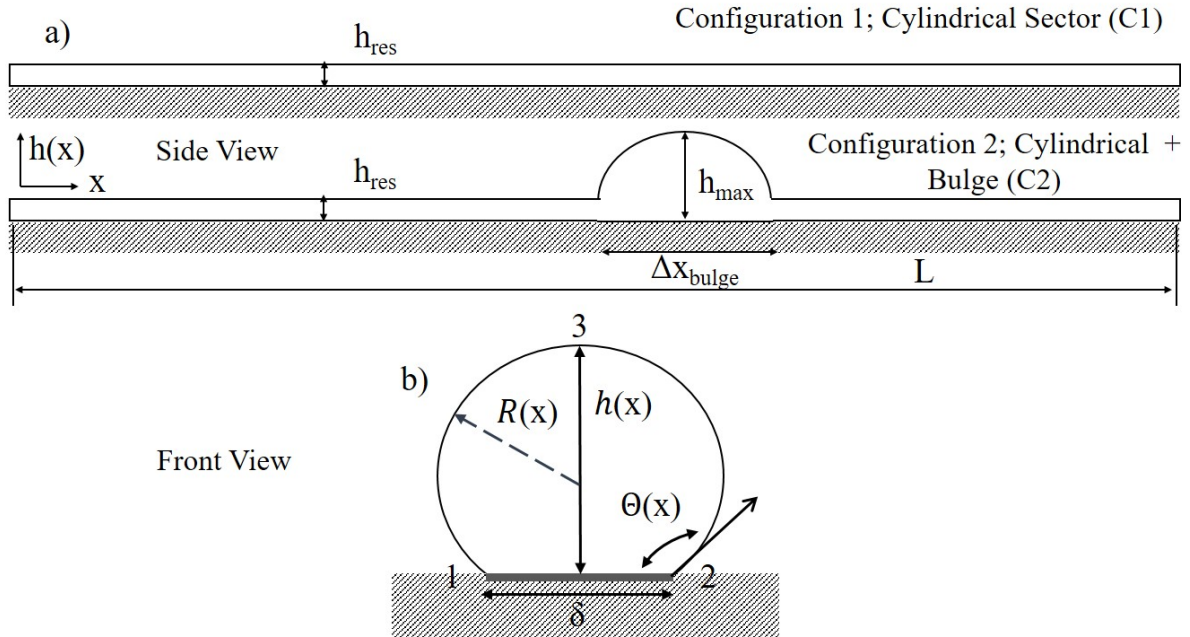


Figure 6. Model of liquid shape depicting two different configurations on a rectangular superhydrophilic track. a) Side view for Configuration 1, which is a part of a cylindrical sector and Configuration 2, which consists of a cylindrical sector over a reduced track length and the bulge. b) Straight-on view of liquid for Configurations 1 and 2; the outline is approximated by a circular segment.

The perimeter  $P(x)$  of the sector is then given by

$$P(x) = R(x)2 \cos^{-1}\left(1 - \frac{h(x)}{R(x)}\right) \quad (2.4)$$

Therefore from Equation 2.3 and Equation 2.4, the total lateral surface area  $A_{LG}$  is given by

$$A_{LG} = \int_0^L P(x)dx = \int_0^L R(x) 2 \cos^{-1}\left(1 - \frac{h(x)}{R(x)}\right)dx \quad (2.5)$$

The cross sectional area of the elemental cylindrical segment is denoted as  $A_{cc}$ . The volume of the cylindrical segment can be expressed by integrating the  $A_{cc}$  (Figure 6b) over the total length of the track ( $L$ ) and can be written as:

$$V = \int_0^L A_{cc}(x) dx \quad (2.6)$$

where,

$$A_{cc}(x) = R(x) \frac{P(x)}{2} - \delta \frac{R(x) - h(x)}{2} \quad (2.7)$$

Equation 2.5 and Equation 2.6 describe configuration 1 if we set  $h(x) = \text{constant}$ .

*Configuration 2:* This configuration is a combination of a cylindrical segment for part of the track length and the liquid bulge. To find a similar expression for configuration 2, we must consider that the integration domain changes, as well as  $h(x)$  does not remain constant along the tracks, unlike the previous configuration. As explained earlier, for a typical static case, Configuration 2 is depicted best in Figure 5c. Clearly, the residual volume segment conforms to Configuration 1 only over a reduced track length ( $L - \Delta x_{bul}$ ). The rest of the track is occupied by the bulge volume spanning over  $\Delta x_{bul}$  and constricted by track width  $\delta$ , in order to minimize the total liquid-gas interfacial surface area. A schematic of the model is shown in Figure 6a

and b. Considering the above factors, Equation 2.5 and Equation 2.6 can be reformulated for Configuration 2 as follows:

$$\text{Surface Area, } A_{LG} = \int_0^{x_1} P_{res}(x)dx + \int_{x_1}^{x_2} P_{bul}(x)dx + \int_{x_2}^L P_{res}(x)dx \quad (2.8a)$$

$$\text{or, } A_{LG} = \int_0^{L-\Delta x_{bul}} R(x) 2 \cos^{-1} \left( 1 - \frac{h(x)}{R(x)} \right) dx + \int_0^{\Delta x_{bul}} R(x) 2 \cos^{-1} \left( 1 - \frac{h(x)}{R(x)} \right) (x) dx \quad (2.8b)$$

$$\text{Volume, } V = \int_0^{L-\Delta x_{bul}} A_{cc,res}(x)dx + \int_0^{\Delta x_{bul}} A_{cc,bul}(x)dx \quad (2.8c)$$

where,  $h(x) = ax^2 + bx + c$  for  $x = x_1$  to  $x_2$  and  $h(x) = \text{constant}$  for  $x = 0$  to  $x_1$  and  $x_2$  to  $L$  and  $a, b, c$  are constants whose values depend on the boundary condition, as stated later in the text. Since  $\Delta x_{bul} = x_2 - x_1$  and the residual volume cross section is equal on either side of the bulge volume, Equation 2.8a reduces to Equation 2.8b.

A closed-form solution of the system of Equation 2.5, Equation 2.6 and Equation 2.8 analytically is not possible. As such, we include suitable free parameter ( $\Delta x_{bul}$ ) from the experimental observations to validate the results.

### 2.3.2 Assumptions

To find  $A_{LG}$ , we list several assumptions (below) to correlate the experimental data with the proposed model.

1. Mean curvature  $\kappa_{mean}$  is defined as  $\kappa_{mean} = (1/r_1 + 1/r_2)$ , where  $r_1$  and  $r_2$  are the two radii of curvature, one from the side view and one from the front view; see Figure 6.  $\kappa_{mean}$  must be constant at all points on the liquid interface for a stationary condition.

2. The cross section at any  $x$  is a section of a circle with chord length  $\delta$ , apparent contact angle  $\theta(x)$  and height  $h(x)$ .
3. Evaporation losses are neglected during the duration of the experiment.
4. Local energy barriers at the wettability-contrast line are neglected.

## 2.4 Results and discussion

Volume deposited on the superhydrophilic track surrounded by a superhydrophobic region to confine the liquid, conforms primarily to two different configurations, as shown in Figure 6. Initially for low volumes, the liquid conforms to a cylindrical segment. On depositing additional volume ( $V_{tot}$ ) on the same track, the liquid transitions from a fully-cylindrical configuration (1) to a cylinder plus bulge configuration (2). The distribution of total volume ( $V_{tot}$ ) contributing to  $V_{res}$  and  $V_{bul}$  is physically governed by two parameters: 1) the geometry (length  $L$ , width  $\delta$ ) of the track, and 2) the total interfacial energy of the system. As described earlier, formation of the bulge is based on surface energy minimization, which is further dependent on the total available surface area at the liquid-gas interface. The following section presents the experimental observations of the behavior of the liquid on the superhydrophilic track. A single case study for one track is explained in details to understand the physical phenomena behind the morphological evolution of the liquid.

### 2.4.1 Case study: $L = 50 \text{ mm}$ , $\delta = 1 \text{ mm}$

For better understanding of the total volume distribution between  $V_{res}$  and  $V_{bul}$ , a particular case is considered here. A wettability-patterned straight track, design similar to Figure 5a, is

used where  $L = 50 \text{ mm}$  and  $\delta = 1 \text{ mm}$ . 15 droplets with volumes ranging between  $\sim 4\text{--}5 \mu\text{L}$  are deposited one by one and the steady state configuration is imaged from the side (side view); see Figure 7a. A custom image-processing code (for details, refer to Appendix C) is used to track the shape and volume evolution of the input droplets. It is clear from Figure 7a that for the initial 5 droplets, there is no formation of bulge on the track. A close examination reveals that the bulge is starting to evolve upon depositing droplet 6 corresponding to total volume  $29.4 \mu\text{L}$  and well formed after the 7<sup>th</sup> droplet onward, corresponding to  $35.4 \mu\text{L}$ . The critical volume of bulge formation ( $V_{cr}$ ) is somewhere in between the 6<sup>th</sup>-7<sup>th</sup> droplet. Experimental  $V_{cr}$  for tracks with theoretical  $V_{cr}$  for different  $\delta$ , are compared later in Table I. Ideally, the location of the bulge formed can be anywhere along the length of the track between  $x = 0$  and  $x = L$ . However, the preferential location of formation as visualized in the experiments is at a width  $\delta(x)$  which is microscopically greater than the rest of the track. Such imperfections can be attributed to the fabrication defects of the experimental samples. It is to be noted that for repeat runs on the same track, the bulge formed at different places along the length of the track, although the bulge morphology remained constant from one run to another, ensuring repeatability. In Figure 7b, the height profile (side view) of the static liquid for increasing volume is plotted in red against the length of the track. To minimize unwanted errors due to end effects of the track, 5 mm from both ends of the track are neglected in the analysis. Red overlapped solid lines on black dashed lines demarcates the bulge volume and the residual volume, respectively. Three parameters, namely height of residual volume ( $h_{res}$ ), maximum height of bulge volume ( $h_{bul}$ ) and length of bulge ( $\Delta x_{bulge}$ ) are extracted from the image analysis; see Figure 6a. As

expected, adding more volume to the track which confines the liquid, the height of the liquid volume has to rise to accommodate the additional volume, as shown in Figure 7b.

Variation of  $h_{res}$ ,  $h_{bul}$  and  $\Delta x_{bul}$  with  $V_{tot}$ .  $h_{res}$ ,  $h_{bul}$  and  $\Delta x_{bul}$  are the raw data measured by analysing images from the experiments. Intuitively, it may seem that  $h_{res}$  should rise with increasing volume, but experimental observations prove otherwise. In Figure 7c,  $h_{res}$  (red) and  $h_{bul}$  (blue) are plotted against varying  $V_{tot}$  (measure using Figure 7d). Initially,  $h_{bul}$  is zero (no bulge has formed yet) and monotonically rises with increasing  $V_{tot}$  after the formation of bulge around  $V_{tot} \sim 20\mu L$ . The slope of the curve decreases, as the effect of gravity ( $Bo \rightarrow 1$ ) becomes comparatively more dominating than surface tension force for higher volumes.  $h_{res}$  on the other hand monotonically increases with a constant slope till the onset of bulge formation at critical volume  $V_{cr} \sim 20\mu L$ . Increasing  $V_{tot}$  further initiates the formation of the bulge, but  $h_{res}$  decreases and steadies at a constant value  $\sim 0.37 \text{ mm}$ . The reason of increasing followed by decreasing  $h_{res}$  can be hypothesized as drainage of liquid from the residual volume ( $V_{res}$ ) to the bulge volume ( $V_{bul}$ ) when the 1st bulge is formed, as elaborated in the following section. Drainage is possible when there is a momentary pressure difference between bulge and residual volume, before stabilization of the liquid. The onset of bulge formation is designated as the *bifurcation point*.

The length of the bulge volume is denoted by  $\Delta x_{bul}$ . For the residual volume, the height is approximately constant. The bulge starts with sharp variation in height. To identify the boundary between the bulge and the residual volume, the image processing algorithm detects this sharp variation of height. The algorithm demarcates the boundary and traces the height

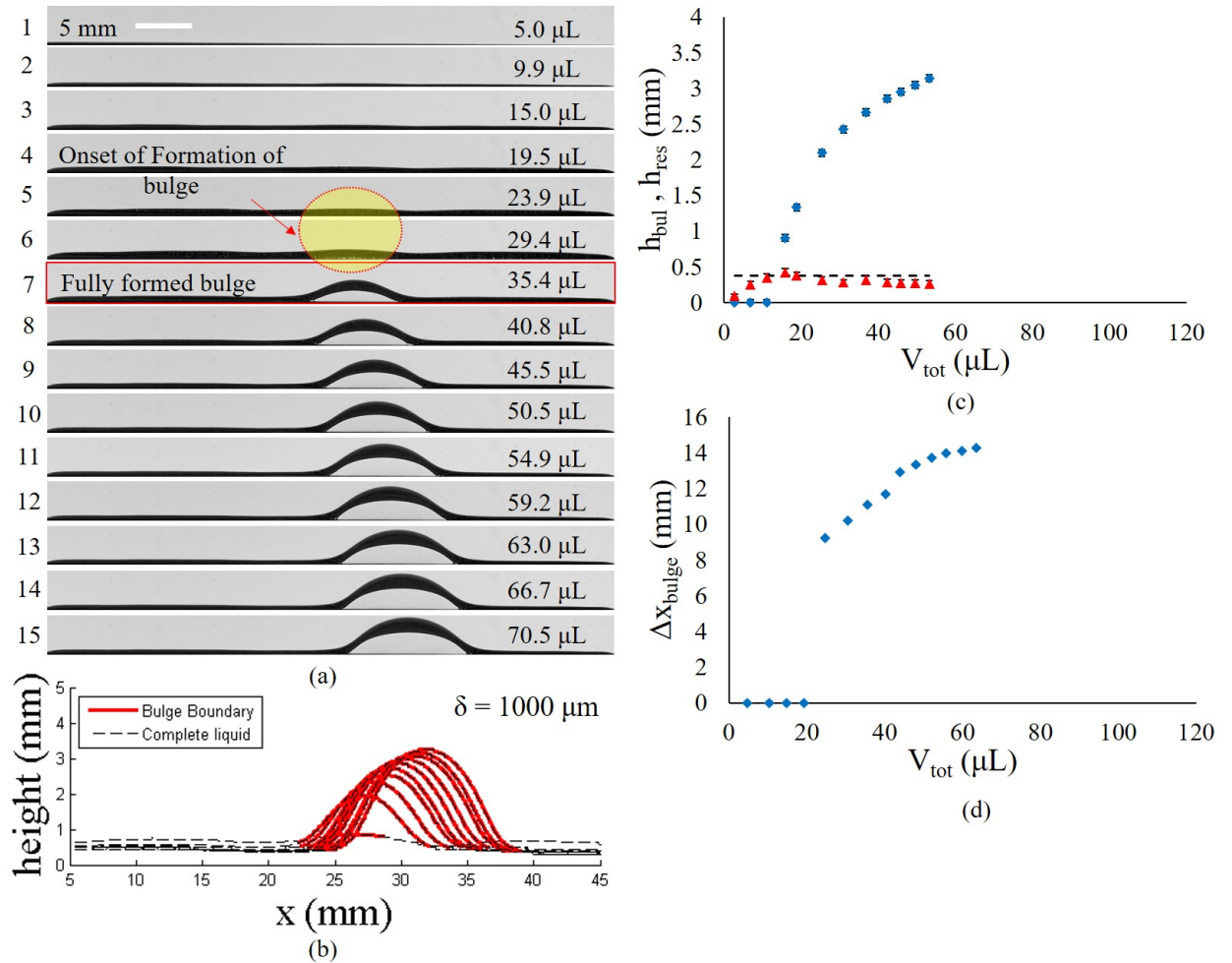


Figure 7. a) Image sequence showing side profile of liquid deposited gently on a superhydrophilic rectangular track one droplet at a time. Note the transition in morphology between 4<sup>th</sup> and 5<sup>th</sup> droplet. White scale bar is 5 mm. b) Height trace (black dashed line) and bulge boundary demarcation (red line) from image analysis of sequence in a. c) Height of residual liquid ( $h_{res}$ , red triangles) and maximum bulge height ( $h_{bul}$ , blue diamonds) plotted against total liquid volume ( $V_{tot}$ ). The black dashed line marks the critical height of the liquid where bifurcation takes place. d) Length of bulge  $\Delta x_{bul}$  variation with  $V_{tot}$ . Track dimensions for a, b, c and d are  $L = 50\text{mm}$ ,  $\delta = 1000\mu\text{m}$ .

profile of the bulge. See Figure 7b, where the red curve highlights the bulge boundary. From the experimental data,  $\Delta x_{bul}$  is plotted against  $V_{tot}$  in Figure 7d. Clearly it is zero till the bifurcation point, after which it sharply rises with gradually diminishing slope nearing a steady state. The trend of  $\Delta x_{bul}$  is similar to that of  $h_{bul}$  owing to gravity effects. On adding more volume, one may expect  $h_{bul}$  and  $\Delta x_{bul}$  to become parallel to the x-axis. Experiments with additional volume beyond  $\sim 80\mu L$  (for track width  $\delta = 1\text{ mm}$ ) were not performed because of  $Bo \rightarrow 1$  and the shape of the liquid will start experiencing gravitational effect. Knowing the  $h_{res}$  and  $\Delta x_{bul}$  trends is crucial, since these are the representative length scales of the principal ( $\kappa_1$ ) and secondary ( $\kappa_2$ ) radii of curvature of the bulge since the Laplace pressure inside the drop depends on  $\kappa_1$  and  $\kappa_2$ .

*Area minimization of liquid-gas interface  $A_{LG}$ :* From Equation 2.2 we know that in order to minimize the total surface energy of the system (solid-liquid-gas), the liquid needs to morph in such a way that the total liquid-gas interfacial surface area ( $A_{LG}$ ) gets minimized for a given volume ( $V_{tot}$ ).  $A_{LG}$  from each experiment is derived from the measured raw data of  $h_{res}$  and  $h_{bul}$  using Figure 6 and Figure 7. Since the cross section of the liquid on the track assumes a circular profile, one can use 3 points method to fit a circle. The 3 points for the experiments are the two corners of the chord of the circular cross section (width of track  $\delta$ ) and the height ( $h(x)$ ), labeled 1, 2 and 3 in Figure 6b. The total  $A_{LG}$  is found by integrating the perimeter of the circular cross section along the length of the track. Figure 8a plots  $A_{LG}$  vs  $V_{tot}$  calculated from the experiment for  $\delta = 1\text{ mm}$ . Red triangles and blue diamonds represent the variation of interfacial surface area for the residual volumes and the bulge volumes respectively. For detailed error analysis,

see supplementary information. The dotted line with black squares is the total  $A_{LG}$ , which is essentially the sum of the residual and bulge interfacial areas. The total  $A_{LG}$  linearly increases with increasing  $V_{tot}$ . However, at the bifurcation point, the slope of the curve changes. The rate of change of  $A_{LG}$  with respect to  $V_{tot}$  is lower. It is at this point the liquid volume on the track changes its morphology from Configuration 1 (no bulge) to Configuration 2 (with bulge). Let's consider a scenario where  $V_{tot}$  always maintained Configuration 1 without any morphology shift to Configuration 2, total  $A_{LG}$  will be higher than as observed in the experiments. The blue solid line plots total  $A_{LG}$  considering no shift in morphology at the bifurcation point. The error bars account for the uncertainties in scaling pixels to mm in image processing, as well as standard deviation in reading the height from the experimental data followed by propagation of error in calculating the area and volume. Configuration 2 after the bifurcation point is a low-energy state as compared to Configuration 1 (cylindrical morphology). In order to lower the surface energy, the liquid shifts from Configuration 1 to Configuration 2, which is evident from the change of slope of total  $A_{LG}$  in Figure 8a at bifurcation. This change in area  $\Delta A_{LG}$  while transitioning is representative of the surface energy saved. The absolute value of energy saved increases with increasing  $V_{tot}$ . An identical trend is observed for all tracks with varying  $\delta$ , as explained in a later section.

*Partition of  $V_{tot}$  into  $V_{res}$  and  $V_{bul}$ :* Knowledge of the division of total volume into bulge volume and residual volume with track geometry is essential in designing devices for several lab on chip (15), point of care or heat transfer applications (52). Additionally, for a pumpless liquid transport (15) scenario,  $V_{bul}$  is the control volume which is transported, and as such,

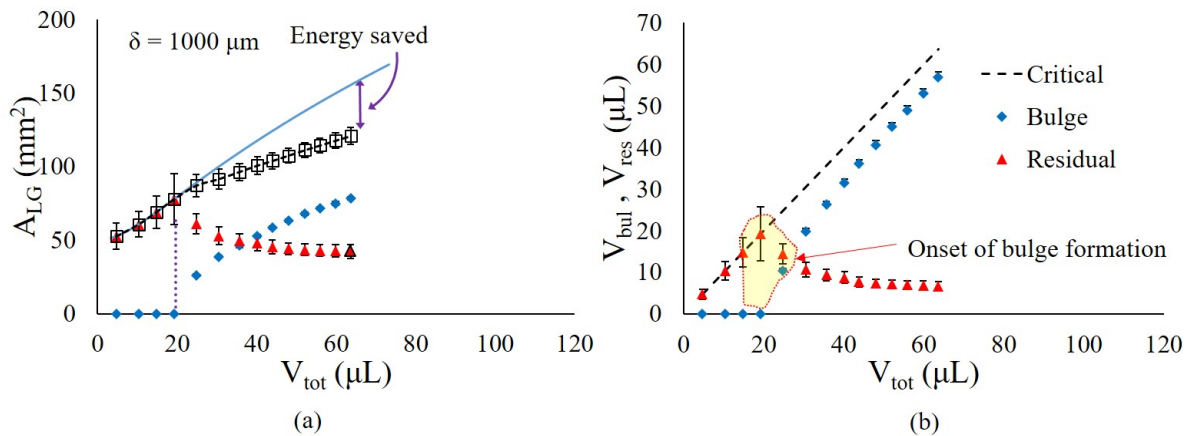


Figure 8. a) Variation of liquid-gas interfacial surface area with total volume of the liquid deposited on the track.  $A_{LG}$  for bulge (blue diamonds), residual volume (red triangles), total volume (open black squares with dashed line). The blue solid line is plotting theoretical  $A_{LG}$  assuming no transformation of the liquid from Configuration 1 (C1) to 2(C2) with increasing volume. The dotted purple line parallel to the y-axis is the theoretical critical volume ( $V_{cr} \sim \frac{\pi\delta^2L}{8}$ ) coinciding with the experimental total volume of bifurcation. b) Bulge volume ( $V_{bul}$ , blue diamonds) and residual volume ( $V_{res}$ , red triangles) plotted vs total liquid volume. The black dashed line is the summation of  $V_{bul}$  and  $V_{res}$  i.e.  $V_{tot}$ .  $V_{bul}$  runs parallel to  $V_{tot}$  after the bulge is fully formed.

better insight will enlighten understanding of such liquid-transport dynamics.  $V_{bul}$  and  $V_{res}$  are calculated quantities from experimental raw data. In a similar calculation like  $A_{LG}$ , the sectional area ( $A_{cc}$ ) of the circular segment is calculated by fitting a circle through the width  $\delta$  and the bulge height  $h_{bul}$  and using Equation 2.7. To find  $V_{res}$ ,  $A_{cc}$  is integrated over the residual volume length ( $L - \Delta x_{bul}$ ). Similarly,  $V_{bul}$  is estimated by integrating  $A_{cc}$  over the bulge length ( $\Delta x_{bul}$ ). It can be inferred from the plot in Figure 8b is that once the bulge is fully formed at  $\sim 35 \mu\text{L}$  for track width  $\delta = 1 \text{ mm}$ , any additional volume goes entirely to the

bulge. The  $V_{bul}$  runs parallel to the  $V_{tot}$  line. As a result, the residual volume remains constant, as indicated by the almost straight line parallel to the x-axis. It is to be noted that the peak value of residual volume ( $V_{res} \sim 25.6\mu L$ ) reduces and stabilizes to  $\sim 10.5\mu L$  once the bulge is fully formed, indicating pumping of liquid to the bulge after the bulge has formed. This observation is further corroborated from Figure 7 by the fact that the height of the residual volume increases and then decreases after formation of the bulge. Tracks with different width  $\delta$  showed similar trend with the bifurcation point shifting to the right.

#### 2.4.2 Model vs experiment

The subsection above reports the experimental observation of the liquid morphology on a superhydrophilic track ( $\delta = 1 \text{ mm}$ ) with varying volume deposited. The model, as described by Equation 2.5 and Equation 2.8b is correlated with the measurements from the experiment in Figure 9. The variation of  $h$  with  $x$  is constant for Configuration 1. However, for configuration 2, it varies with  $x$  for the bulge section, *i.e.* for length  $\Delta x_{bul}$ . The location of bulge formation along the track is dependent on the local variations due to imperfections of the track width  $\delta$ . Since the bulge morphology is independent of this location, for consistency, it is assumed in the model that the bulge is formed at the end of the track spanning over length  $\Delta x_{bul}$ . A parabolic curve is fitted to the bulge morphology, such that  $h(x) = ax^2 + bx + c$  for  $x = L - \Delta x_{bul}$  to  $L$  and  $h(x) = \text{constant}$  for  $x = 0$  to  $L - \Delta x_{bul}$ . The parameters  $a$ ,  $b$ ,  $c$  are obtained from the boundary conditions  $h(x) = h_{res}$  at  $x = L - \Delta x_{bul}$  and  $h(x) = h_{max}$  at  $x = L - \frac{\Delta x_{bul}}{2}$ . The black dashed line in Fig. 9 shows the area variation with volume for such

a configuration, where maximum  $\Delta x_{bul}$  is used from the experiment and  $h(x)$  is varied starting from lower limit  $h(x) = h_{res}$  to  $h_{max}$  from experimental values.

### 2.4.3 Parametric variation of track width $\delta$

Experiments to study the liquid shape morphology with varying track width ( $\delta$ ) were performed and are plotted in Figure 10a.  $h_{res}$  initially rises and stabilizes at a constant value. This behavior is consistent for all the tracks. The bifurcation point (the onset of bulge formation) is shifting to the right as  $\delta$  increases indicating that the critical volume ( $V_{cr}$ ) of bulge formation is increasing. The slope of  $h_{bul}$  decreases as  $\delta$  rises from 500  $\mu m$  to 1500  $\mu m$ . The flattening of the slope is attributed to the bulge volume becoming more prone to the effect of gravity, i.e.  $Bo \rightarrow 1$ , since the characteristic length scale  $\delta$  is increasing. In Figure 10b, the variation of  $A_{LG}$  is shown with increasing  $V_{tot}$  for the residual, bulge and total volumes. The blue line (cylindrical morphology) is plotted assuming that there is no transition from Configuration 1 to Configuration 2. The change in surface area due to this transition declines with increasing  $\delta$ . Since interfacial surface energy is directly proportional to the surface area ( $A_{LG}$ ), it is energetically more favorable for the liquid to transition earlier from configuration 1 to 2 for lower  $\delta$ . However, there is no significant difference in  $A_{LG}$  till the bifurcation point, irrespective of any configuration that the liquid follows. All the curves before the formation of the bulge, coincide on each other; see Figure 10b.

The experimental data point out that this bifurcation commences approximately at a height half the track width ( $h_{cr} \sim \delta/2$ ). The dashed black line in Figure 10a is equivalent to  $\delta/2$  for each track and the bifurcation point lies close to  $h_{cr}$  within the experimental error limit for all

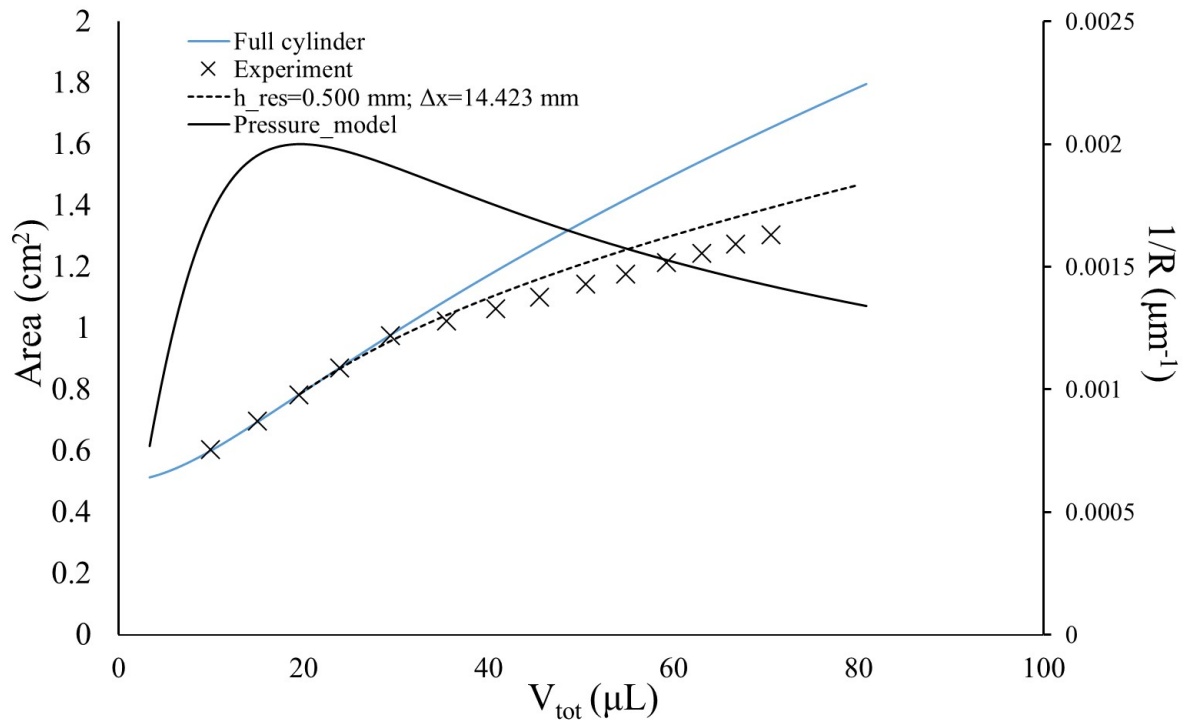


Figure 9. Composite plot showing comparison of experimental data and proposed model. In the primary axis, total  $A_{LG}$  is plotted for Configuration 1 (blue solid) and Configuration 2 (black dashed) from the model with increasing liquid volume. Black cross overlays the total  $A_{LG}$  from experimental data. The point of bifurcation from experiment matches well with the model. On the secondary axis, curvature of the liquid, which is an indicator of the Laplace pressure, is plotted with increasing volume for Configuration 1. Peak pressure point (where radius of curvature is maximum, i.e.  $\theta_{app} \sim 90^\circ$ ) approximately coincides with the experimental and theoretical bifurcation volume.

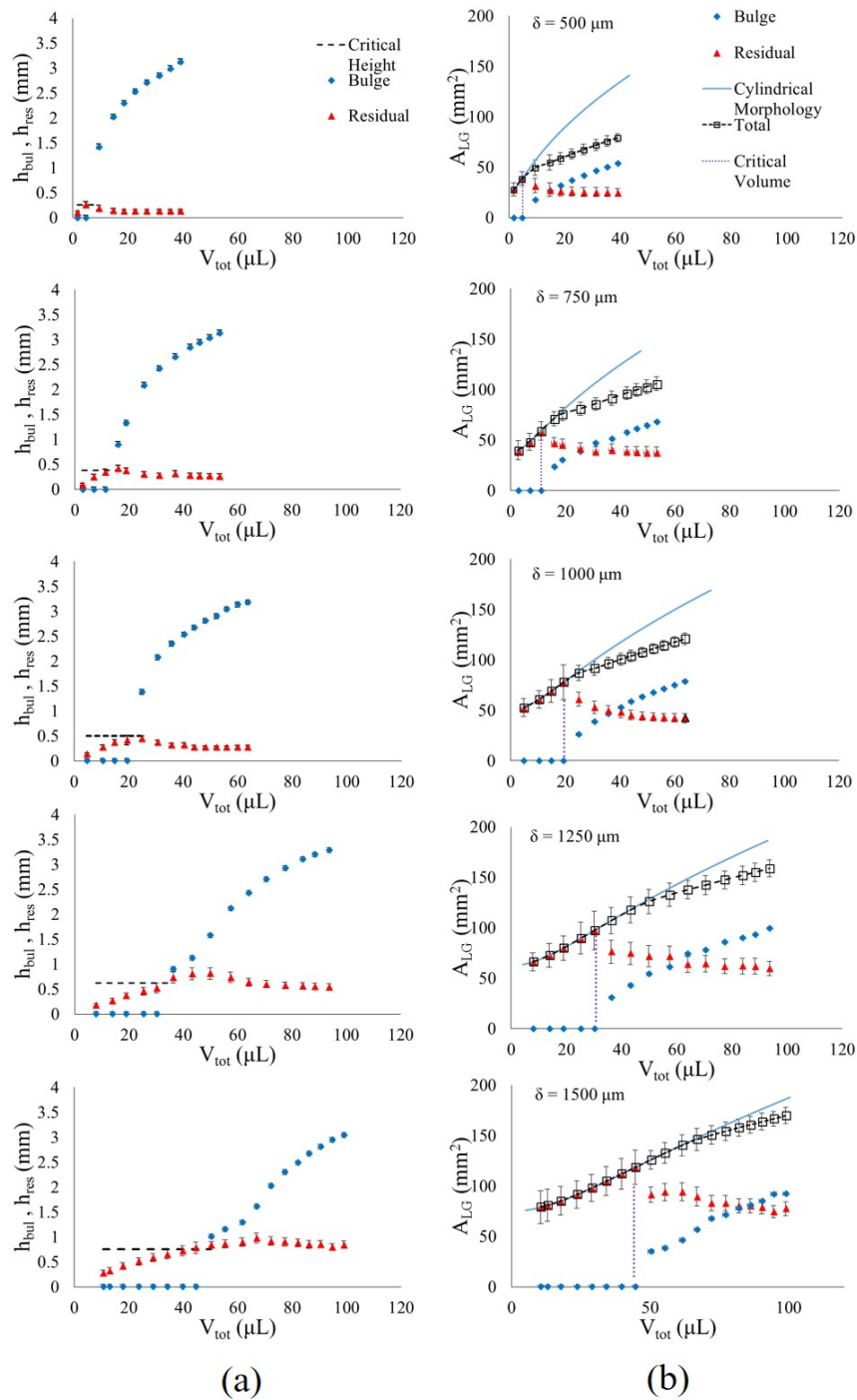


Figure 10. Plot showing  $A_{LG}$ ,  $h_{res}$  and  $h_{bul}$  with increasing  $V_{tot}$  for tracks of varying width ( $\delta = 500, 750, 100, 1250, 1500 \mu m$ ). a) The dashed line is the critical height for each track where  $h_{cr} = \delta/2$ .  $h_{res}$  initially rises till bifurcation and then decreases to a steady value, a similar trend for all track widths. The bifurcation point shifts to the right with increasing  $\delta$ . b) Total, bulge volume area is increasing and residual volume area  $A_{LG}$  is initially increasing till bifurcation and then decreasing with rising volume. Blue solid line is the theoretical  $A_{LG}$  considering Configuration 1 for increasing volume. Experimental  $A_{LG}$  deviates from theoretical value due to transition of liquid morphology from C1 to C2. The purple dotted line is the theoretical  $V_{cr}$  which coincides with experimental  $V_{tot}$  at the onset of bulge formation.

	$\delta = 500\mu m$	$\delta = 750\mu m$	$\delta = 1000\mu m$	$\delta = 1250\mu m$	$\delta = 1500\mu m$
$V_{tot}(\mu L)$ (experiment) (at onset of bulge)	4.67	11.05	19.24	30.01	44.57
$V_{cr}(\mu L)$ (theory)	4.91	11.05	19.64	30.69	44.19
Percentage difference (%)	-4.88	0	-2.03	-2.21	0.86

TABLE I

DEVIATION OF THEORETICAL AND EXPERIMENTAL  $V_{CR}$  FOR VARIABLE RECTANGULAR TRACK WIDTHS. PERCENTAGE DEVIATION IS WITHIN ADMISSIBLE EXPERIMENTAL ERROR LIMIT.

values of  $\delta$ . Volume corresponding to  $h_{cr}$  assuming a cylindrical configuration with a circular cross section is  $\sim \frac{\pi\delta^2 L}{8}$ , which is also the critical volume ( $V_{cr}$ ) of bulge formation. The purple dotted lines in Figure 10b depicts theoretical  $V_{cr}$  for each track and shpw excellent agreement with the experimental data. From a track design perspective, it is now possible to predict at what total input volume the bulge formation will occur. Table I refers to the values of experimental  $V_{tot}$  where bifurcation takes place and theoretical  $V_{cr}$  along with their respective error values. To estimate the distribution of total volume into residual and bulge volume,  $V_{res}$  is plotted against the  $V_{tot}$ , both normalized by  $V_{cr}$ . Normalized residual volume ( $\hat{V}_{res}$ ) and normalized total volume ( $\hat{V}$ ) is given by Equation 2.9a. The plots from all the experiments collapse onto each other. Thus, by knowing the  $V_{res}$  for a given  $V_{tot}$ , one can easily estimate the  $V_{bul}$ ; see figure Figure 11.

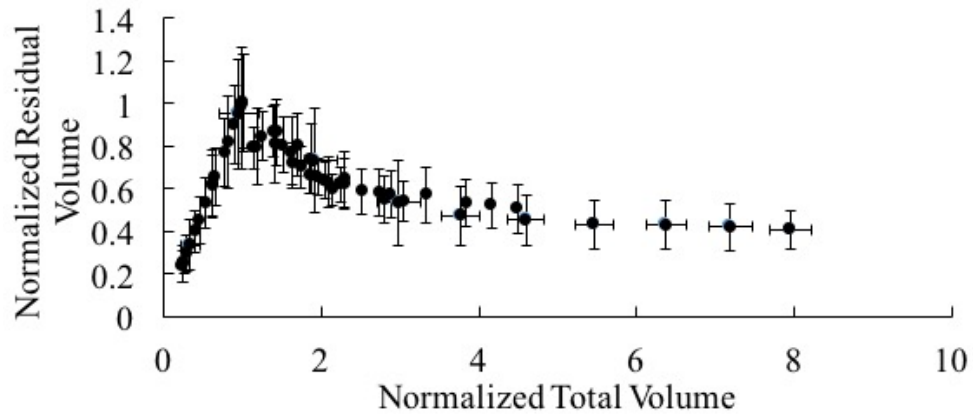


Figure 11. Normalized residual volume vs. normalized total volume for tracks with  $\delta = 500, 750, 1000, 1250, 1500 \mu m$  as per Equation 2.9a. The curves collapse on each other within the experimental error. Onset of bulge formation takes place at  $\hat{V}_{res} = 1$  and  $\hat{V} = 1$

$$\hat{V}_{res} = \frac{V_{res}}{V_{cr}} \quad (2.9a)$$

$$\hat{V} = \frac{V_{tot}}{V_{cr}} \quad (2.9b)$$

where  $V_{cr} = \frac{\pi \delta^2 L}{8}$

## CHAPTER 3

### RAPID PUMPLESS TRANSPORT

Previously published as *Ghosh, Aritra, Ranjan Ganguly, Thomas M. Schutzius, and Constantine M. Megaridis. "Wettability patterning for high-rate, pumpless fluid transport on open, non-planar microfluidic platforms." Lab on a Chip 14, no. 9 (2014): 1538-1550.* This chapter also formed the basis for a PCT patent application PCT/US2015/012302.

#### **3.1 Introduction**

Microfluidic systems on planar chips have gained popularity for handling miniscule volumes of liquids on the surface of open substrates. Open microfluidics offers a promising mode of digital microfluidics(53), which involves manipulating individual droplets without the need for dedicated components like microchannels, pumps, valves, sorters or mixers. Handling liquid on open substrates also minimizes the contact between the fluid and the channel walls, thus eliminating the risk of air-bubble clogging, fouling by debris and nonspecific surface adsorption of reagents. Besides, handling isolated droplets on the digital microfluidic platform minimizes cross-contamination between samples. However, achieving regular microfluidic tasks (e.g., sample drawing, metering, merging and dispensing) in a controlled fashion remains a challenge when using open microfluidic systems. The salient requirements of a successful liquid transport strategy include: (1) rapid pumpless transport; (2) metering and controlling the liquid being dispensed; and (3) merging and splitting nontrivial tasks. Discrete microfluidic liquid

transport technology has been achieved by electrowetting-on-dielectric (EWOD)(54), optoelectrowetting (OEW)(55), magnetic force(56), gravity(57; 58), thermocapillarity(59), or acoustic vibrations(60; 61). Surface wettability has played a supportive role in most of these applications by ensuring the desired droplet mobility and controllability. However, these active technologies require continuous power supply (or a desired orientation of the substrates in case of gravity-driven transport) and elaborate *on-chip/off-the-chip* interfacing arrangements (e.g., electrode array, permanent magnet assembly, sub-surface heating arrangement, etc.) which for some applications are necessary but make their implementation more difficult.

Capillary-force driven transport of liquid droplets using spatial gradients of surface wettability has shown promise for pumpless liquid transport on open substrates. Liquid droplets on such surfaces experience an unbalanced force in the direction of increasing wettability, leading to fluid mobilization on the substrate(62). Santos and Ondaruhu(40) demonstrated free running droplets confined on hydrophilic tracks delimited by hydrophobic regions. They used droplets containing surface active hydrophobizing agents, which modified the surface wettability at the droplet's receding end as it rolled over the substrate. Chen *et al.*(63) studied Marangoni-flow induced self-propulsion of aniline droplets with limited control over motion, velocity and volume of liquid transport. Several groups have demonstrated passive transport of liquid droplets on substrates by spatially altering the surface wettability through chemical patterning(31; 64), physical texturing(43; 42; 44), or a combination of both(65; 66). Bliznyuk *et al.*(39) used lithographically created, anisotropic patterned surfaces to generate surface tension gradients for actuating droplet motion. Their design yielded a maximum droplet speed

of  $\sim 14 \text{ mm s}^{-1}$ . Schutzius *et al.*(23) reported surface tension confined (STC) tracks that produced guided capillary transport of low surface tension liquids in a straight line with velocity approaching  $30 \text{ mm s}^{-1}$ . The fastest rate of pumpless droplet transport (velocities of  $50 - 400 \text{ mm s}^{-1}$ ) has been reported through the use of triangularly patterned, wettable tracks on superhydrophobic substrates, prepared through elaborate micropatterning and nanotexturing methods(67). Although this work demonstrated the capacity of rapid on-chip liquid transport, it did not perform any complex flow handling tasks that are desired on lab-on-a-chip (LOC) applications. Recently Alheshibri *et al.*(45) extended this approach on aluminum/copper wettability-patterned substrates. However the transport velocity obtained therein was an order of magnitude lower than that observed earlier by Khoo *et al.*,(67) while the maximum transport distance was limited to  $30 \text{ mm}$  (for wedge angle,  $\alpha = 4^\circ$ ), and the design(45) was restricted to metal substrates.

Given a primary source of liquid pumping, an equally important task remains in guiding and confining the mobile droplets as desired on the open substrate. A few notable studies in this regard include the one by Xing *et al.*(28), who reported guided transport of liquid on wettability-confined superhydrophilic tracks on superhydrophobic substrates using Laplace pressure differences. On-chip control of water droplets along arbitrarily curved wettability-confined tracks(57) or microgrooves<sup>6</sup> has also been reported. Microfabricated STC patches(68) and chemically patterned, triangular, superhydrophilic patches(69) on inclined substrates have also been used to guide water droplets. This former work(68) has been extended recently to produce more complex droplet shapes and to achieve static(70) and dynamic(71; 72) splitting of

droplets. Balu *et al.*(73) achieved advanced droplet manipulation tasks like merging, transfer, splitting and storage, but used multiple substrates and extensive physical maneuvering.

Although the above mentioned studies showed potential of harnessing wettability engineering for on-chip liquid transport, to date, such transport has required very elaborate surface engineering (e.g., micro- and nanofabrication)(65; 70), producing relatively low transport rates (the peak velocity mostly in the range of a few  $cm\ s^{-1}$ )(39; 23; 45) that were substrate limited, or achieved very simple modes of droplet movement(67). For low-cost open (surface) microfluidic applications, particularly for paper-based(74; 32) or textile-based(75) ones, a substrate independent, yet straightforward surface preparation approach is more desirable.

The present study uses a facile, substrate-independent wettability patterning method to produce tapered, superhydrophilic, microfluidic tracks that are capable of inducing controlled on-chip movement of aqueous liquid volumes with the characteristic size comparable to the capillary length  $\kappa^{-1} = \sqrt{\gamma/\rho g}$  ( $\gamma$  denoting the liquid surface tension,  $\rho$  is the density and  $g$  is the acceleration due to gravity), by overcoming viscous and other opposing forces (e.g., gravity). The concept is developed and demonstrated with coatings based on  $TiO_2$  powder, which, when present in optimum quantities within a hydrophobic polymer matrix, forms composites that are intrinsically superhydrophobic. Such composite coatings become superhydrophilic upon exposure to UV light. Thus, a masking process can facilitate spatially selective conversion from superhydrophobic to superhydrophilic behavior, which is used herein to fabricate open-air devices that can move fluid efficiently without power input. Simple design features of wettability patterning have been used on versatile substrates (e.g., metals, polymers or paper) to

demonstrate complex droplet handling tasks, some of which are in 3-D geometries. The present concept can be applied as building blocks for disposable microfluidic biosensors. Large liquid transport rates ( $\sim 150\text{--}350 \mu\text{L s}^{-1}$ ) and velocities (exceeding  $400 \text{ mm s}^{-1}$ ) make the substrates suitable for high-throughput pumpless microfluidic devices. The designs are capable of handling small denominations of liquid volume ( $\sim 1 \mu\text{L}$ ), and repeated disposal of smaller liquid droplets can lead to large ( $\sim 500 \mu\text{L}$ ) cumulative transport. While the lower volumes are applicable for common microfluidic tasks(28), the upper volume range is relevant for on-chip liquid storage(73) or some specialized microfluidic applications that require large-volume samples (e.g., in the interrogation well of an ultra-wide field fluorescence imaging device for undiluted whole-blood samples(76), which requires volumes  $\sim 1 \text{ mL}$ ). Applicability of the design on metal substrates, on the other hand, makes the technique attractive for diverse engineering applications involving a wide range of liquid handling tasks, e.g., rapid chip cooling(77), water management in fuel cells(78), or condensate removal from the liquid collecting plate in a phase change microthermal diode(79).

## **3.2 Materials and methods**

### **3.2.1 Materials**

The chemicals used comprise a fluoroacrylic copolymer dispersion (PMC) manufactured by DuPont (20 *wt.*% in water; Capstone ST-100), titanium(IV) dioxide nanoparticles (anatase,  $< 25 \text{ nm}$ , 99.7% trace, Sigma Aldrich) and ethanol ( $\sim 100 \text{ wt.}\%$ , Decon Labs). The following substrates were used: a mirror-finish aluminum plate (multipurpose polished aluminum alloy 6061, 2 *mm* thick, McMaster Carr), a transparency film for laser copiers (cross-linked

polyethylene terephthalate (PET, PP2500, 3M), and a white photocopier paper ( $80 \text{ g m}^{-2}$ , Paper One). The PMC copolymer serves as the primary component of the superhydrophobic surface. The  $\text{TiO}_2$  nanoparticles impart the required micro- and nanoscale roughness and promote hydrophilicity through well-known mechanisms(80) and possible photocatalytic degradation of hydrophobic chemistries upon exposure to UV radiation(81). All of the above materials were obtained off-the-shelf and are readily available in the marketplace.

### **3.2.2 Methods**

We used a facile and scalable approach to fabricate samples that juxtapose wettable and non-wettable spatial domains of various shapes and sizes. A typical example for synthesizing such wettability-patterned coatings is presented. First, a dispersion containing the hydrophobic PMC copolymer,  $\text{TiO}_2$  nanoparticles, and ethanol was prepared and subsequently spray deposited onto the substrates in order to generate a superhydrophobic surface. To synthesize the dispersion, a suspension of  $\text{TiO}_2$  and ethanol was first formed.  $1.5 \text{ g}$  of  $\text{TiO}_2$  was added to  $14 \text{ g}$  of ethanol and was then probe sonicated ( $750 \text{ W}$ ,  $13 \text{ mm}$  probe diameter, 40% amplitude,  $20 \text{ kHz}$  frequency, Sonics and Materials Inc., model VCX-750) by supplying  $1000 \text{ J}$  of energy. Next,  $2.5 \text{ g}$  of PMC solution ( $20 \text{ wt.}\%$  in water) was added and shaken mechanically at room temperature to form a stable dispersion. The above solution was sprayed on three different types of substrates (mirror-finish aluminum, PET films, and paper) using an airbrush (VL siphon feed,  $0.73 \text{ mm}$  spray nozzle, at  $276 \text{ kPa}$  (gage) air pressure, Paasche) to form a uniform coating. The spray-coated samples were then dried in a preheated oven at  $60 \text{ }^\circ\text{C}$  for 4 hours, ultimately forming a superhydrophobic surface suitable for wettability patterning.

Superhydrophilic patterns were formed on this superhydrophobic surface through selectively exposing the coated substrate to UV radiation (Dymax 5000 EC, 400 W, 390 nm UV source) using a photomask (a transparency film printed with black negative patterns using a common household laser printer) for 30 minutes (see Figure 12). The UV light passed through the transparent (unprinted) section of the mask and struck the coated superhydrophobic substrate. The presence of TiO<sub>2</sub> in the composite promoted photocatalytic conversion of the exposed domains, rendering them superhydrophilic(82). Complex pattern designs with features as fine as 200  $\mu\text{m}$  were obtained using this photomasking technique.

Scanning electron microscopy (Hitachi S-3000N) was performed for visualizing the roughness features of the spray-deposited surface. Experiments were conducted by first mounting the substrate on a horizontal micro stage. A high speed camera (Redlake MotionPro, mounted with Navitar TV ZOOM 7000 or OPTEM ZOOM 100 lens) was used to capture the rapid events, such as liquid bridging, de-bridging and droplet volume splitting. The substrates were illuminated by a cool light source (FOSTEC, 8375). The real-time fluid transport features were recorded using a standard DSLR (Canon Rebel T1) camera mounted with a macro telephoto zoom lens (Sigma 70 – 300mm). The water drops ( $\sim 4.7 \mu\text{L}$ ) were dispensed using a syringe pump (ColePalmer, 74900) through a 100  $\mu\text{m}$  inner diameter needle (Nordson EFD, 32GA GP). The needle was strategically placed above the substrate such that the drops fell on the desired location at low speed and the inertial effects remained negligible as compared to the capillary force.

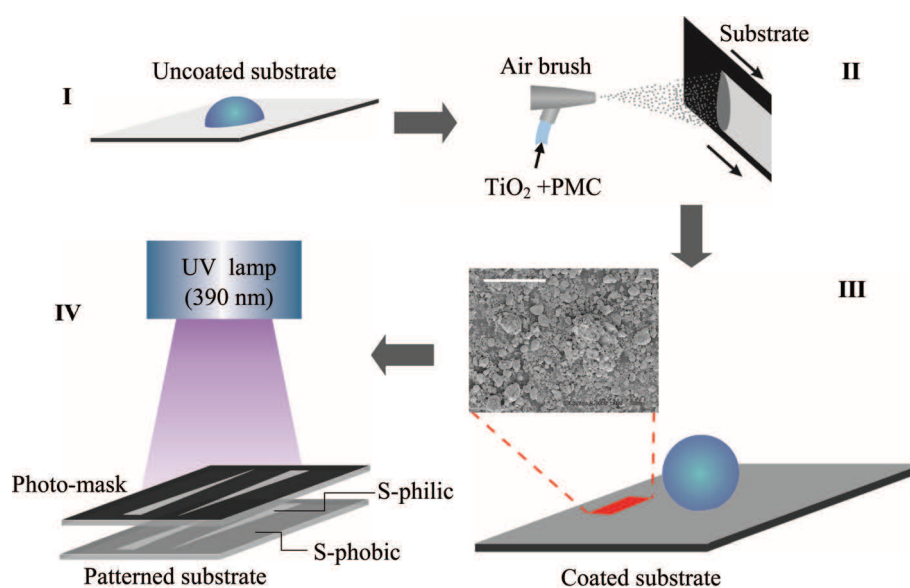


Figure 12. Salient steps of surface preparation. (I) Uncoated substrate (aluminum, PET film or regular white paper). (II) Spray-coating of a  $\text{TiO}_2$ -PMC aqueous suspension on the substrates. (III) Coated substrate, and SEM image (scale bar is  $100\mu\text{m}$ ) of the coated surface showing the different length scales of the deposited nanoparticle composite coating. Combination of PMC and the roughness imparted by the  $\text{TiO}_2$  particles renders the surface superhydrophobic (water beads). (IV) UV treatment of the superhydrophobic substrate through a patterned photomask (top) to form the superhydrophilic regions (bottom). Exposed regions turn superhydrophilic (S-philic) upon 30 minutes of exposure to UV, while the unexposed regions remain superhydrophobic (S-phobic).

### 3.3 Results and discussion

Scanning Electron Microscopy images of the coated substrate (see Figure 12) show the presence of multiscale roughness features ranging from a few hundreds of nanometers to a few tens of microns, as produced by the  $\text{TiO}_2$  nanoparticles. The parts of the substrate that were not exposed to UV radiation retained their hydrophobicity. The average equilibrium contact angle values (computed from at least 10 sets of data for each type of surface) are listed in Table II, while sample images of sessile drops on each substrate are given in Figure 36 in Appendix A. As-received samples of aluminum, paper and PET films exhibited average sessile contact angles of  $78.2^\circ \pm 2^\circ$ ,  $85.5^\circ \pm 4^\circ$ , and  $8.5^\circ \pm 2^\circ$ , respectively. The micron and submicron features of the coated surface did not differ with the nature of the substrate (e.g., Al plates, PET films or paper). Consequently, the superhydrophobic sections of the substrates exhibited contact angle values ranging from  $151^\circ$  to  $156^\circ$  at room temperature irrespective of the substrate (see Table II). The UV-exposed superhydrophilic tracks, on the other hand, exhibited contact angles lower than  $3^\circ$ , the exact value of which could not be measured. For paper substrates, prolonged exposure to water on the superhydrophilic regions produced capillary imbibition through the substrate itself, thereby making CA measurements difficult.

#### 3.3.1 Liquid transport along a wedge-shaped track

Different shapes of superhydrophilic patterns were examined. As the simplest building block of such patterns, a wedge-shaped superhydrophilic track (akin to a long and narrow tapered path) with a wedge angle  $\alpha = 3^\circ$  was initially chosen. Figure 13(a) shows time-lapsed images of liquid transport of a  $4.7 \mu\text{L}$  droplet deposited at the narrow (left) end of a wedge track on

	Uncoated Substrate	Coated Substrate (hydrophobic part)	Coated Substrate (hydrophilic part)
Aluminum	$78.2^\circ \pm 2^\circ$	$151.2^\circ \pm 2.3^\circ$	*
Paper	$85.5^\circ \pm 4^\circ$	$154.5^\circ \pm 2^\circ$	*
PET Film	$8.5^\circ \pm 2^\circ$	$156^\circ \pm 3^\circ$	*

TABLE II

SESSILE CONTACT ANGLE VALUES ON VARIOUS SUBSTRATES. CONTACT ANGLE DATA EVALUATED FROM SETS OF 10 READINGS. \* CONTACT ANGLES TOO LOW TO MEASURE.

a horizontal Al substrate (the photomask actually produced a trapezoidal shape; the droplet was deposited  $\sim 1 \text{ mm}$  to the right from its narrowest edge, which was  $\sim 770 \mu\text{m}$  wide). The superhydrophilic track width where the droplet was deposited is approximately  $820 \mu\text{m}$ , which is significantly narrower than the droplet diameter ( $\sim 2 \text{ mm}$ ). Therefore, the liquid spreading in the transverse direction (i.e., towards the hydrophobic regions on either side of the track) was constricted by the wedge boundary. After the droplet came in contact with the track ( $t = 0$  snapshot in Figure 13), a rapidly advancing film front was observed to propagate ahead of the droplet towards the wider end of the track. This was driven by hemiwicking through the microscale roughness features on the superhydrophilic track(25). The bulk of the fluid trailed behind the propagating front in the form of a liquid bulge with a progressive axial elongation. As the liquid front advanced further along the wedge track, the bulge disappeared gradually and the liquid took the shape of a semi-conical rivulet. Prior studies have been performed on wetting morphologies of static liquid volumes confined laterally on narrow superhydrophilic tracks patterned on a superhydrophobic background. Brinkmann and Lipowsky(48) have shown

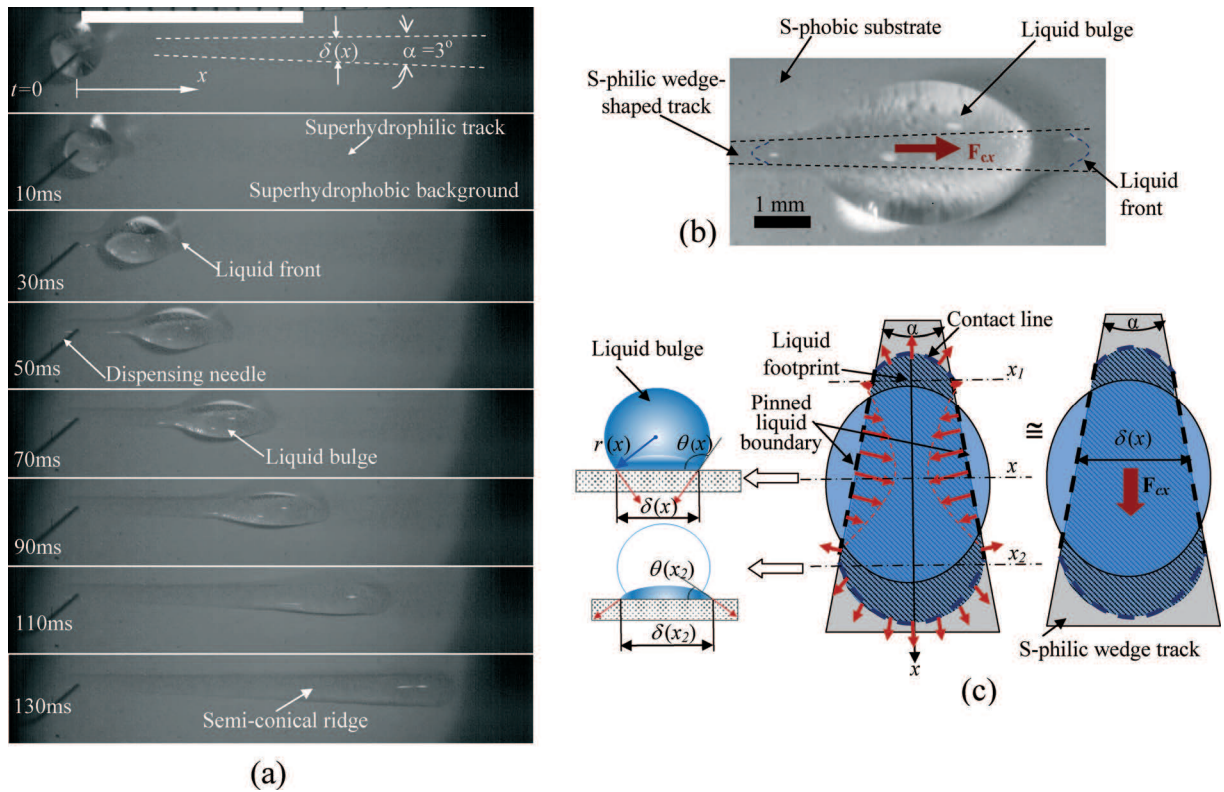


Figure 13. (a) Time-lapsed images (top view) of liquid transport through the wedge-shaped superhydrophilic track on a horizontal Al-substrate. The white bar at the top denotes 10mm. (b) Morphology of the liquid bulge, approximated as an ellipsoid of finite footprint on the wedge-shaped superhydrophilic track, moving along the track; (c) origin of the driving capillary force on the liquid bulge.

that the shape of such liquid accumulation on rectangular tracks depends on the ratio  $\Omega/\delta^3$  (where  $\Omega$  denotes the liquid volume and  $\delta$  denotes the superhydrophilic track width). Below a critical value of  $\Omega/\delta^3$ , the liquid assumes a semi-cylindrical shape (elongated along the track and confined by the wettability-contrast lines at the two sides of the track). This critical value depends on the equilibrium contact angles on the superhydrophobic and superhydrophilic

domains ( $\theta_{Sphobic}$  and  $\theta_{Sphilic}$ ). The liquid volume in Figure 13 is in a dynamic state, unlike in(48) where it was static. Nevertheless, similar bulge-like morphology was observed close to the point of deposition (i.e.,  $x \sim 0$ ) where  $\Omega/[\delta(x)]^3 = 4.7/(0.82)^3 \approx 8.52$ . The local track width  $\delta(x)$  increases linearly with the distance  $x$  along the wedge-shaped track. Therefore, for a given volume of the deposited droplet,  $\Omega/[\delta(x)]^3$  decreases with increasing  $x$ . For the image sequence in Figure 13(a), the liquid bulge morphology was observed up to  $x = 14.5 \text{ mm}$  (where  $\delta = 1.55 \text{ mm}$ ), corresponding to  $\Omega/[\delta(x)]^3 \approx 1.26$ . This can be reckoned as the critical value for the track considered here. The subcritical morphology here is a bounded semiconical shape, as opposed to a semi-cylindrical one on the rectangular track in (48).

The liquid along the wedge-shaped track is driven by the unbalanced capillary forces in the lengthwise direction, which push the droplet from a smaller wettable footprint (left) to a larger one (right). Over an initial length of  $15 \text{ mm}$ , the liquid bulge recorded an average velocity (measured as the displacement rate of the largest girth of the elongated liquid volume traveling along the track) of  $110 \text{ mm s}^{-1}$ . After the first droplet passed, the superhydrophilic channel became wet (presuffused). When an identical-sized droplet was deposited at the narrow end of the presuffused track, both the liquid bulge and the propagating front behaved in a similar manner, but they exhibited an even higher velocity ( $\sim 300 \text{ mm s}^{-1}$ ) in the first  $15 \text{ mm}$ .

The initial advancement of the liquid film on the track is akin to hemiwicking of liquid on a textured superhydrophilic track(25). However, the liquid bulge motion is strongly influenced by the Laplace pressure differential between its front and back. Figure 13(b) shows a close-up of the liquid bulge as it traveled from left to right along the wedge-shaped superhydrophilic track.

The elongated droplet has a footprint that leads at the front end and trails at the rear side of the bulk with very small contact angles (due to near-complete wetting of the superhydrophilic track). The apparent contact angle  $\theta(x)$  of the liquid bulge along the two straight edges of the footprint (where the liquid contact line is pinned) does not follow Young's equation; rather it is governed by the local track width and the liquid volume contained per unit length at that particular location of the track(22). Theoretically, this angle should be less than  $\theta_{Sphobic}$  and greater than  $\theta_{Sphilic}$  and would vary along the track length  $x$ . The net capillary force  $F_{cx}$  on the droplet may be obtained by taking the axial derivative of the total surface energy of the system, namely

$$F_{cx} = -\frac{d}{dx}[\gamma_{LS}A_{LS} + \gamma_{LG}A_{LG} + \gamma_{SG}A_{SG}] \quad (3.1)$$

where  $\gamma$  denotes the surface energy per unit interface area between the solid (S), liquid (L) and gas (G), and A is the corresponding surface area. Intuitively, the liquid has a propensity to move forward, as that leads to wetting of a larger area of the superhydrophilic track, resulting in a net lowering of the surface energy in the positive  $x$  direction. As seen in Figure 13(c), the liquid bulge experiences surface tension forces along the leading and trailing boundaries of the liquid footprint and also along the pinned sidelines. Clearly, the leading edge has a larger length than the trailing one due to the wedge shape of the track. Also, the top view of the droplet in Figure 13(b) indicates that  $\theta > 90^\circ$  for most of the section of the liquid bulge that touches the pinned sidelines. Thus, along these axially diverging contact lines, the net component of the surface force acts along the positive  $x$  direction. This propels the liquid droplet, a phenomenon not observed on a straight fixed-width hydrophilic track(48). The local

Laplace pressure at any section of the liquid bulge is  $\sim \gamma_{LG}/r(x)$ , where the local curvature of the liquid  $r(x) \approx \delta(x)/[2 \sin \theta(x)]$ . Both  $\theta(x)$  and  $\delta(x)$  vary along the length of the track (for small wedge angles,  $\delta(x)$  is proportional to the wedge angle  $\alpha$ ). Assuming a representative average contact angle  $\theta_{avg}$  over the length of the bulge, the net axial Laplace pressure gradient in the liquid bulge can be estimated as;

$$\frac{dP}{dx} \sim -\frac{d}{dx} \left[ \frac{\gamma_{LG}}{r(x)} \right] \sim -\gamma_{LG} \frac{d}{d\delta(x)} \left[ \frac{2 \sin \theta(x)}{\delta(x)} \right] \frac{d\delta(x)}{dx} \sim 2\gamma_{LG} \sin \theta_{avg} \frac{1}{\delta(x)^2} \alpha \quad (3.2)$$

This pressure gradient is responsible for driving the droplet to the wider portions of the wedge track. Equation 3.2 indicates that the capillary pressure gradient is proportional to the wedge angle  $\alpha$  and inversely proportional to the square of the local track width  $\delta(x)$ . However, evaluating the magnitude of the capillary force from this expression requires a priori knowledge of how the angle  $\theta(x)$  varies with  $x$ , which requires computational analysis(48). A separate experiment was therefore carried out (see Figure 14(a)) under a static scenario following the approach of Lorenceau and Quere(83) to calculate the capillary force on the droplet at the onset of the motion. The substrate was mounted on a tilt platform with a large enough inclination so that a droplet placed at the narrow end of the presuffused wedge does not move up. The tilt angle  $\beta$  was gradually reduced until the capillary force became comparable to the in-plane component of the droplet weight, so that the droplet moves up the plane. For a known droplet volume  $\Omega$  (the test was repeated with different volumes of dispensed droplets) and  $\beta$  measured

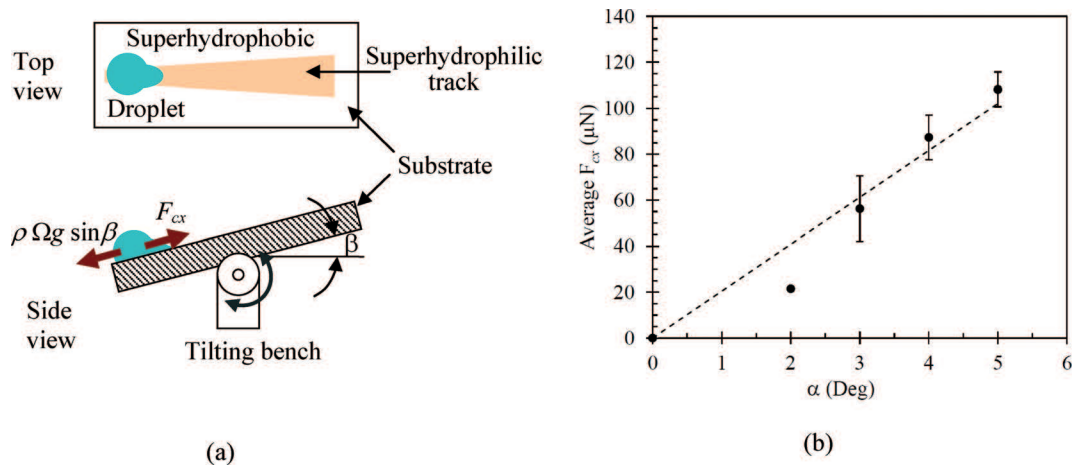


Figure 14. (a) Arrangement for measurement of the capillary force  $F_{cx}$  at the narrow end of the wedge at the onset of droplet motion. (b) Variation of  $F_{cx}$  with the wedge angle  $\alpha$  (error bar shows the standard deviation due to variability in droplet volume).

from the experiment, the capillary force (at the narrow end of the wedge track) can therefore be calculated as;

$$F_{cx} = \rho \Omega g \sin \beta \quad (3.3)$$

Figure 14(b) shows the variation of capillary force on the droplets with the wedge angle. Each data point represents about 100 readings taken with dispensed droplet volumes ranging from  $4.7 \mu\text{L}$  to  $23.5 \mu\text{L}$  (the readings of  $\beta$ , and hence of the  $F_{cx}$  did not vary much with  $\Omega$  - see Section A.2 and Figure 37 in Appendix A for details - while the error bars represent the standard deviation in readings). Clearly, the linear nature of the plot of  $F_{cx}$  against  $\alpha$  shows conformity to Equation 3.2. The capillary force for the case shown in Figure 13 (i.e.,  $\alpha = 3^\circ$ ) is found to be approximately  $56.3 \mu\text{N}$ , which would, in the absence of any restrictive forces, produce an

instantaneous acceleration of  $12 \text{ m s}^{-2}$  for a  $4.7 \text{ }\mu\text{L}$  droplet. The observed acceleration on a horizontal substrate could differ from this value since the actual bulge volume is slightly less than  $4.7 \text{ }\mu\text{L}$  (part of the liquid spread by hemiwicking). Also, in reality, the motion of the liquid bulge is resisted by contact angle hysteresis (CAH) between its advancing and receding fronts, as well as viscous forces(67). The effects of the first two factors (the loss of liquid from the bulge due to hemiwicking, and the restrictive force due to CAH) have competing influences on the droplet acceleration, while the viscous force on the droplet at the onset of its motion is negligible. Later in this section, we shall see that the predicted value of acceleration indeed matched closely with the observed initial acceleration of the liquid bulge on a presuffused track.

At the far downstream portion of the wedge track, the contact angles at the pinned sidelines may become less than  $90^\circ$ , thus having a contribution that resists the forward motion of the bulk liquid (see Figure 13(c)). This may lead to a flagging  $F_{cx}$  at the downstream portion of the tracks(45), forcing the droplet transport to cease. However, for the geometry considered in Figure 13 and the liquid volumes dispensed herein, the sustained forward movement of the droplets persisted until the droplets reached the wide edge of the track (travel path  $\sim 25 \text{ mm}$ ). Subsequent droplets (deposited afterwards at the same location) also exhibited a similar behavior on the presuffused track, although these moved faster. The track kept pumping the liquid from the narrower end and accumulating it at the wider end in the form of a growing bulge (the latter happens if the accumulated volume exceeds the threshold value discussed before). A separate study on a  $60 \text{ mm}$  long wedge-shaped track having  $\alpha = 4^\circ$  showed that the

track was able to hold  $235 \mu\text{L}$  of water in a rivulet shape before bulging out at its wider end (see Figure 38 in Appendix A)

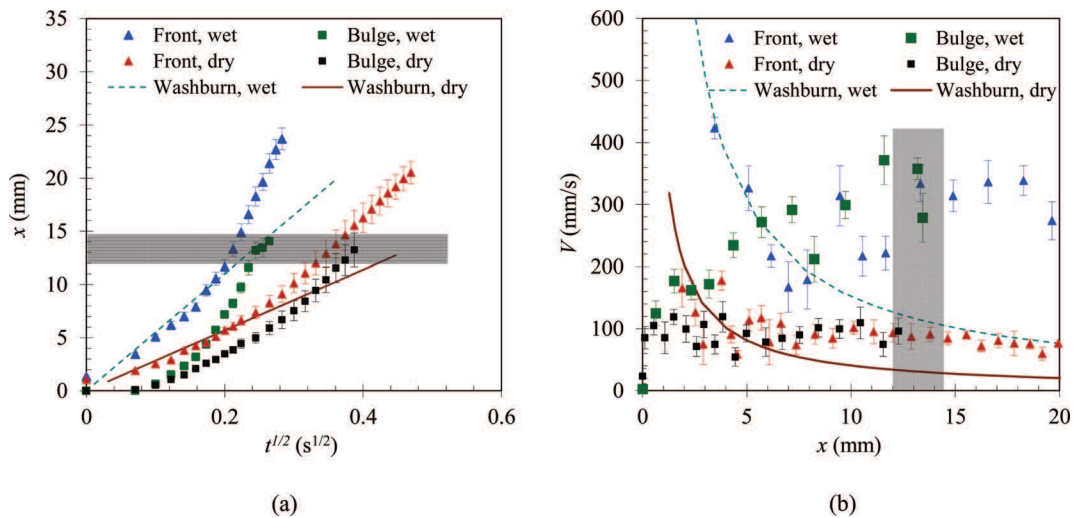


Figure 15. Transport of the liquid front and the liquid bulge along a wedge-shaped track with  $\alpha = 3^\circ$  (see Figure 13a). (a) Distance  $x$  from the dispensing location as a function of  $t^{1/2}$ , and (b) velocity as a function of position along the track. Comparison of the experimental data (symbols) with the Washburn model for wetting behavior (continuous curves) is also made. The gray bar denotes the spatial region in which the bulge volume shape transformed to the spread-out rivulet shape.

Figure 15 shows (a) the displacement-time (on  $x-t^{1/2}$  axes) and (b) the velocity-displacement profiles of the liquid front and the bulge on a dry track and on a presuffused track. Each plot represents readings averaged over at least six independent runs, while the error bars show the standard deviation. As seen in Figure 15, the liquid front begins to spread along the dry track

at a high speed ( $\sim 165 \text{ mm s}^{-1}$  at  $x = 1.9 \text{ mm}$ ) but it gradually slows down ( $\sim 90 \text{ mm s}^{-1}$  at  $x = 7 \text{ mm}$ ) as the liquid film spreads down the track. This propagation can be attributed to the capillary wetting of the textured philic track by the liquid. Typical capillary wetting would exhibit the Washburn profiles(23) for the displacement-time and velocity-displacement plots, following  $x = \sqrt{\gamma_{LG}d_{pore}t/4\mu}$  (straight line on the  $x - t^{1/2}$  plot) and  $V \sim \gamma_{LG}d_{pore}/\mu x$  (rectangular hyperbola on the  $V - x$  plot), respectively. The hemiwicking displacement and velocities for Washburn flow are also plotted in Figure 15 for water ( $\gamma_{LG} = 72.1 \text{ mNm}^{-1}$ , dynamic viscosity  $\mu = 0.89 \text{ mPas}$ ), assuming an estimated mean surface feature size (created by the  $\text{TiO}_2$  particles)  $d_{pore} = 40 \text{ }\mu\text{m}$ . Although the pore size was used as a fitting parameter, the optimal value is consistent with the size of aggregated  $\text{TiO}_2$  particles that create the surface texture. The observed displacement plot for the liquid front showed agreement with the Washburn profile for approximately the first  $5 \text{ mm}$  of travel (see Figure 15a) and exceeded the latter significantly in the downstream region. The liquid bulge, on the other hand, exhibits a relatively sluggish start due to its inertia, but it soon speeds up to closely follow up the liquid front. Beyond  $x \sim 7 \text{ mm}$  the liquid bulge is found to move at nearly the same velocity with the front, trailing it by  $\sim 2 \text{ mm}$ , until the bulge shape disappears. At this stage, the liquid bulge following the hemiwicking front acts as a source that offers the driving potential for the liquid front to propagate further ahead. This eventually causes the liquid front's velocity to exceed that predicted from the Washburn equation (Figure 15(b)).

On a presuffused track, the effective capillary pore diameter ( $d_{pore}$ ) is larger than that exhibited by the dry tracks since the finer microstructure features on the surface remain submerged,

leaving only larger surface apex features to influence hemiwicking (see Section A.4 in Appendix A). Thus, the initial velocity of the hemiwicking front on a presuffused track should be much larger. Indeed, as seen in Figure 15, the liquid front on a presuffused track recorded an initial velocity of  $\sim 424 \text{ mm s}^{-1}$ , which approximates a Washburn velocity profile corresponding to  $d_{pore} = 150 \text{ }\mu\text{m}$  (optimal value obtained by fitting the experimental data). As in the case of a dry track, the liquid bulge on a presuffused track also accelerated from rest, and gradually moved faster. The acceleration of the liquid bulge at the inception of the droplet motion was found to be  $dV/dt|_{t=0} = 12.3 \text{ m s}^{-2}$  (see Section A.5 in Appendix A). This is in excellent agreement with the acceleration ( $12 \text{ m s}^{-2}$ ) evaluated from the capillary force diagram (Figure 14b). Beyond  $x \sim 6 \text{ mm}$ , the liquid bulge velocity exceeded the velocity of the front but was not able to catch up within the available track length. The front velocity also picked up speed as it received better feed from the liquid bulge trailing right behind it. Figure 15 clearly indicates that the motion of the liquid front through the wedge-shaped superhydrophilic track follows the Washburn behavior only in the first few millimeters of the track length beyond which the advancing velocity is significantly bolstered by the liquid bulge trailing behind the propagating meniscus. A similar behavior was also observed when water droplets containing 10% ethanol (by wt.) were transported on the same wedge track; however, the average velocity was lower ( $\sim 83\%$  of that observed with pure water) due to the lower surface tension ( $47.5 \text{ mN m}^{-1}$ ) and higher viscosity ( $1.21 \text{ mPa s}$ ) of the ethanol-water mixture.

### 3.4 Liquid transport using complex pattern

#### 3.4.1 Droplet metering, merging and rapid transport

Having established the pumping capability of the individual wedge-shaped tracks, more complicated surface patterns comprising these tracks were designed to demonstrate multistep functionalities. It is apparent from the previous section that the wedge-shaped tracks transport the liquid towards the wider end either in the form of a bulge (early) or a semi-conical rivulet (late). If two such tracks are laid parallel to each other, and the  $\Omega/\delta^3$  ratio for the track ( $\delta$  being the track width at the wider end) is large enough to favor the bulge morphology, it is possible to generate two juxtaposed liquid bulges with the potential to interact with one another towards certain functionalities. For example, if the intervening space between the adjacent tracks is comparable to the lateral width of each liquid bulge, the menisci of the accumulated liquids at the wider ends of the tracks would merge to form a liquid bridge(84). The critical volume at which the liquid bridge occurs depends on the geometrical features of the tracks and their lateral spacing. This provides a design tool for metering precisely the volume of pumped liquid that eventually forms a bridge between the two tracks. The device design we attempt, therefore, comprises three wedge-shaped tracks; Figure 16(a). Tracks A and B are 21.5 mm long with a wedge angle of  $1^\circ$  spaced parallel to each other at an axis-to-axis pitch of 3.6 mm, while track C, 21.5 mm long with a wedge angle of  $10^\circ$ , is placed in tandem. A 1.5 mm.5 mm rectangular superhydrophilic strip D protrudes from track C between tracks A and B to facilitate the liquid draining process (as described below). Water droplets were dispensed one at a time using metering syringes placed over the narrow ends of tracks A and B and were transported

spontaneously to their wider ends, where  $\delta \sim 720 \mu m$ . Even with the first pair of droplets ( $4.7 \mu L$  each) deposited, the ratio  $\Omega/\delta^3 \sim 12.6$ , which is an order of magnitude higher than the critical value mentioned in section 3.3.1 This is corroborated by the observation of liquid bulges formed at the ends of tracks A and B and their growth until they attain the state shown in Figure 16(b). For the given spacing between tracks A and B on the aluminum substrate, the two bulges touched at their largest girth (see Figure 16(b) and (b1)) after each channel received 7 droplets of  $4.7 \mu L$  each (i.e., a total of  $65.8 \mu L$ ). Figure 16(c) and (c1) show the onset of liquid bridging caused by the merger of the two bulges. The bridge grew immediately due to coalescence of the two volumes (Figure 16(d, e) and (d1, e1)). The liquid bulges had an oblong shape (the axial extent nearly 2.5 times their lateral spread), as seen from the top in Figure 16(b-e); the end view of the same event is shown in Figure 16(b1-e1). The bridge height as recorded in Figure 16(b1-e1) may be treated as the characteristic bridge dimension during coalescence. Over the first 5 ms of bridge formation, the droplet bridge height grew with the square root of time (see Figure 41 in Appendix A), which is typical of a droplet coalescence scenario where capillary and inertial forces dominate(85). The liquid bridge eventually touched the intervening superhydrophobic surface (Figure 16(e1)) and rested on it in a Cassie (non-wetting) state(86), as is evident from the visible glossy texture underneath it (see the white arrow in Figure 16(e)). The curvature of the liquid bridge is seen to create a lens effect so that the microscale surface texture details of the superhydrophobic region become magnified, and thus more visible. The liquid bridge kept expanding axially due to the inertial effect at the expense of the lateral spread of the bulge when ultimately it touched the narrow end of

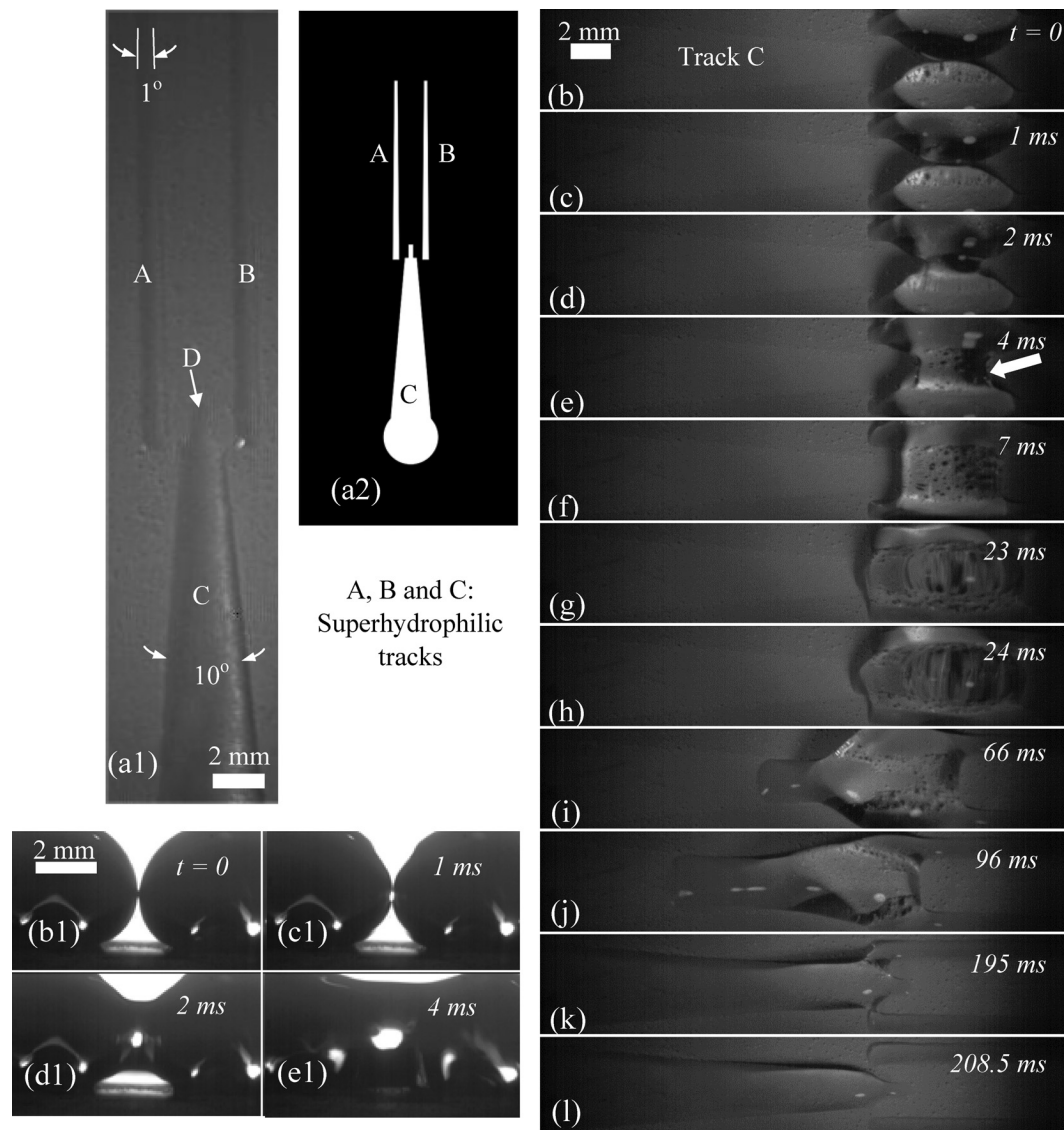


Figure 16. Patterned Al substrate (a1) and mask (a2) used for demonstrating a multi-step functional surface device capable of performing pumpless liquid bridging and draining. Snapshots of events on the liquid bridge circuit: (b, b1) liquid bulges at the wider ends of tracks A and B just before a liquid bridging event; (c, c1) onset of liquid bridging, (d-f) progression of liquid bridge formation; (g-h) liquid bridge touches the end strip D of track C; (i-k) progression of liquid pumping along track C; (l) de-bridging over D at the end of pumping. Starting from the onset of the liquid bridge touching strip D (frame (g)) to the de-bridged state (frame (l)), this procedure achieves an average pumping rate of  $357 \mu\text{L s}^{-1}$ . (b1)-(e1): End views of the bridge formation and growth events (top views in (b)-(e)) as seen from the downstream delivery side of the device.

strip D (see Figure 16(g)). The liquid then hemiwicked through the superhydrophilic strip and advanced onto track C when the final stage of pumping began (Figure 16(h)). The liquid in the bridge was pumped through track C from  $t = 24 \text{ ms}$  to  $t = 208.5 \text{ ms}$  (see Figure 16(h) through Figure 16(l)) until the pool drained completely and de-bridged from tracks A and B. With continual dispensing of droplets at the loading (narrow) end of tracks A and B, the cycle of bridging, spreading, pumping and de-bridging can be repeated as many times as needed. Between the events of the liquid bridge touching track D (Figure 16(g)) and the de-bridging (Figure 16(l)), the device pumped at an average rate of  $357 \mu\text{L s}^{-1}$  without any external power input. More importantly, the quantity of transposed volume, which can be controlled by altering the geometry of the tracks, is highly repeatable. The design performed equally well on the PET film and paper, as it did on metal. Figure 17(a) shows the different stages of a similar cycle of bridging, pumping and de-bridging on a horizontal paper substrate (the water was dyed red for better visualization). For the same dimensions of track patterns as in Figure 16 (Al substrate), the bridging of liquid accumulated on tracks A and B in Figure 17(a) occurred once after each track received 6 droplets (each measuring  $4.7 \mu\text{L}$ ), thus pumping approximately  $56.4 \mu\text{L}$  per cycle. A similar pumping behavior was also observed on the PET film. Figure 17(b) shows snapshots of liquid accumulation on a PET film substrate on track C after the device pumped for 1, 4, 7 and 10 continuous cycles. Figure 17(b3) and (b4) show that the drained liquid rests on track C showing a bulge morphology, with the liquid pinned on the wettability-contrast line along the periphery of the larger track. The maximum storage capacity of track C is limited by the track area and the value of  $S_{phobic}$ . If the liquid is suitably drained

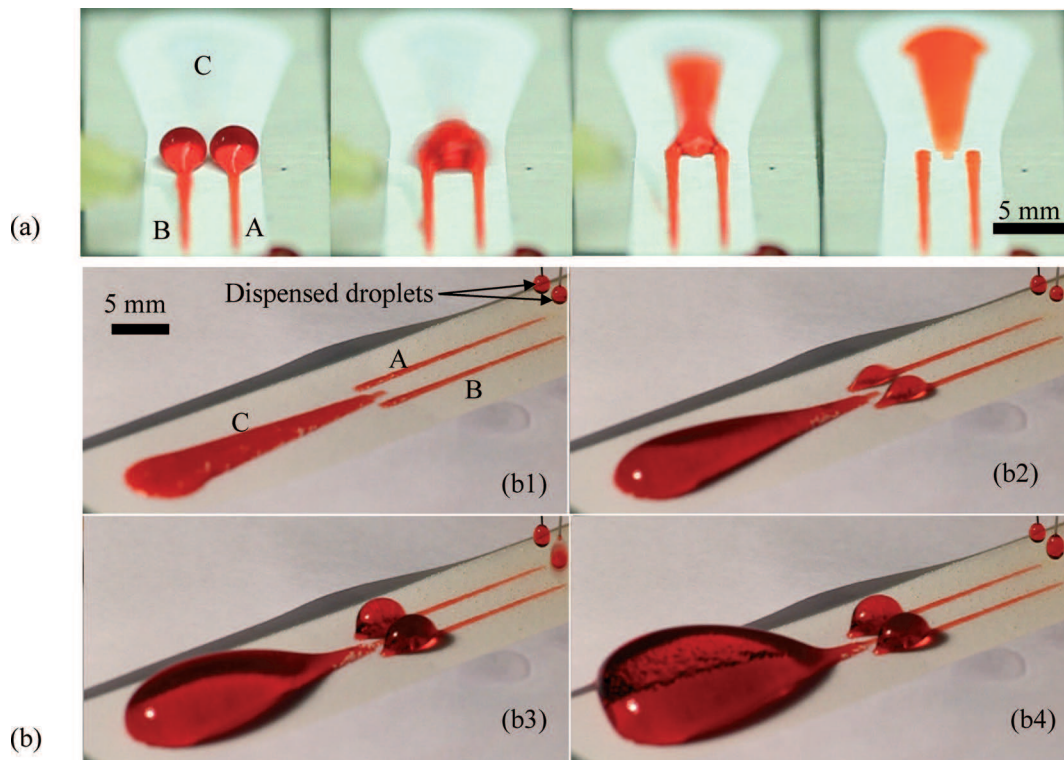


Figure 17. (a) Elevated end view sequence displaying liquid bridging and draining on the design of Figure 16(a) applied on a horizontal paper substrate. (b) Collection of liquid on the bridge circuit on a horizontal transparency (PET) film substrate after pumping for (b1) 1 cycle ( $\sim 56 \mu\text{L}$ ), (b2) 4 cycles ( $\sim 226 \mu\text{L}$ ), (b3) 7 cycles ( $\sim 395 \mu\text{L}$ ), and (b4) 10 cycles ( $\sim 564 \mu\text{L}$ ). The liquid (water) is dyed for better visualization.

out from the downstream end of track C (e.g., by providing a larger superhydrophilic well or by capillary wicking), the device will pump repeatedly for an indefinite period. On both aluminum and PET film substrates, the design was found to exhibit continual pumping at the same cycle volume until track C is filled up to a level that the contact line could no longer be pinned at the borders of the track. For the paper substrate, the repeatability was compromised by selective imbibition in the substrate itself through the philic track due to prolonged exposure to water. Therefore, for paper based substrates, long-term performance is not warranted. However, the paper-based substrate may be used as an ideal choice for inexpensive single-use microfluidic devices.

### **3.4.2 Droplet splitting in multiple equal volumes**

Droplet splitting is an important task in digital microfluidics, for example, when a given sample volume needs to be split for feeding a multiplexed microfluidic architecture. Figure 18(a) shows the design of a droplet splitter that has 3 identical wedge-shaped superhydrophilic tracks (23 mm in length, wedge angle  $40^\circ$ ), each laid radially outward from a common center at  $120^\circ$  angular spacing. The narrow ends of the wedge-shaped tracks are spaced 800  $\mu\text{m}$  from the center, which is marked by a 400  $\mu\text{m}$  circular hydrophilic spot to allow droplet anchoring during deposition on the substrate. Figure 17(b1)(b6) show the time-lapsed images of an event after a 4.7  $\mu\text{L}$  droplet was deposited on the central philic spot. As the droplet was dispensed on the substrate (Figure 18(b1)), the outer rim of its base touched the narrow ends of the radial tracks (Figure 18(b2)) upon impact; the liquid quickly spread along the superhydrophilic radial tracks, forming a liquid bridge that connected the three tracks and the central philic spot

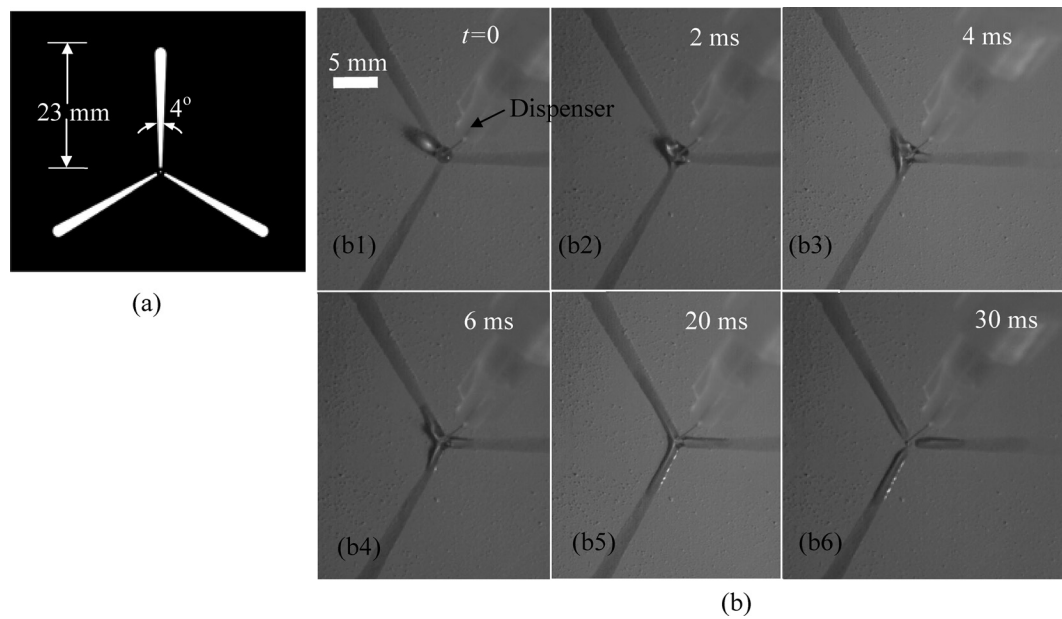


Figure 18. (a) Photomasking template for the droplet three-splitter design. (b) Time-lapsed snapshots of a complete cycle of droplet splitting on an Al substrate with 3 radially equispaced wedge tracks. The event achieves a collective average pumping rate of  $157 L s^{-1}$ .

(Figure 18(b3)). The pumping continued from the central spot with a liquid front propagating along each track (Figure 18(b4, b5)) until the central liquid volume de-bridged at the inner ends of the track (Figure 18(b6)), leaving a very small residual droplet at the central philic spot. The salient advantage of this design from the one proposed by Lee *et al.*(71) is that the residual central volume is much smaller than the original droplet volume, with no liquid bridging the split radial volumes. Thus, for an LOC application this design eliminates the possibility of cross-contamination. As observed from the timestamps in Figure 18(b), the droplet took 30 *ms* to fragment between the central spot and the three radial tracks - corresponding to

a pumping rate of  $\sim 157 \mu L s^{-1}$ . For a uniform split, each track in Figure 18 transported  $\sim 1.5 \mu L$  volume. The splitter design was also successfully tested on paper and a PET film (see Figure 42 in Appendix A). It is important to note that irrespective of the substrate, the uniformity of volumes collected at the end of each track is found to be very sensitive to the precision with which the original droplet is deposited on the central spot. Any eccentricity or bias in the position of the liquid dispenser leads to unequal liquid distribution (see Figure 42b). This feature can therefore be used as a tool for two-dimensional microfluidic position sensing. Splitter designs with a higher number of radial arms (with the same track size and distance of inner ends from the central phobic spot) are also demonstrated in Figure 42c in Appendix A where each splitter arm is shown to transport  $\sim 1 \mu L$  liquid per cycle.

### **3.4.3 Liquid transport up an incline**

The use of flexible substrates like paper and transparency (PET) films allows the ability to attain out-of-plane liquid transport. In order to realize such transport, the capillary force has to overcome gravity in part of the microfluidic circuit. The wedge-shaped superhydrophilic tracks on a superhydrophobic paper or PET film surface have already been found capable of producing rapid liquid transport on horizontal substrates. Figure 19 shows that the capillary force produced on the droplet by the wedge-shaped track is also strong enough to move the liquid up along an inclined substrate. Figure 19(a1-a3) show images of liquid being pumped up a ramp to an elevation of  $9 \text{ mm}$ . This corresponds to an approximate ramp tilt angle of  $13^\circ$  for the flexible PET film substrate, although the ramp appears slightly curved due to the flexibility of the PET film. Figure 19(a2 and a3) show a residual volume of liquid left behind on

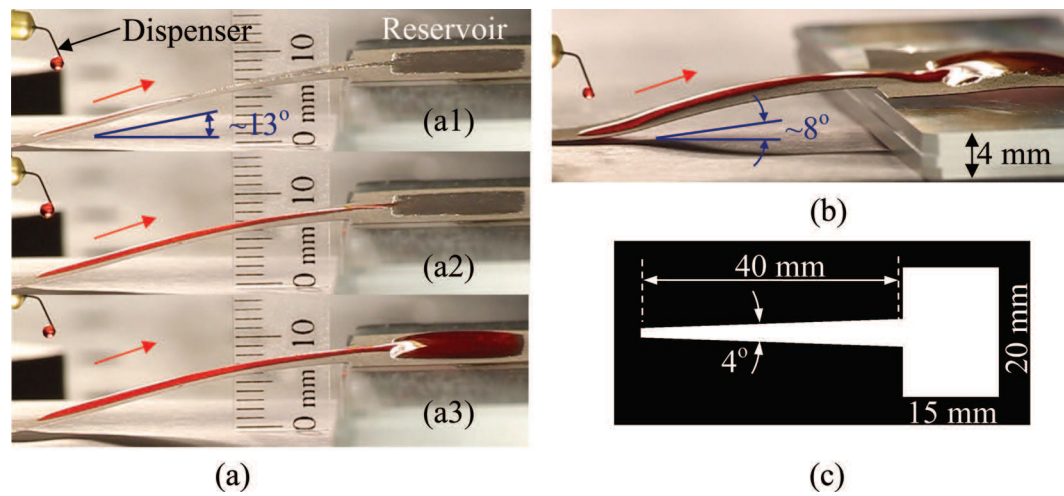


Figure 19. Transport of liquid up along an inclined superhydrophilic wedge-shaped track. (a) Snapshots of water (dyed for better visualization) moving up along a transparency (PET) film substrate to an elevation of  $9\text{ mm}$  after: (a1) one drop ( $4.7\ \mu\text{L}$ ), (a2) 5 drops ( $23.5\ \mu\text{L}$ ), and (a3) 40 drops ( $188\ \mu\text{L}$ ). (b) 25 droplets ( $117.5\ \mu\text{L}$ ) were pumped up a height of  $4\text{ mm}$  along an identical track on paper. (c) The photomasking template for the tracks used in (a) and (b).

the inclined superhydrophilic track after pumping a given volume to the reservoir on the top. After transporting a total of 50 drops ( $235\ \mu\text{L}$ ) of water up the ramp, the track was found to retain only  $14\ \mu\text{L}$ , a small portion of the total volume propelled to the top. Similar pumping was also observed on paper where the same design was found to transport  $117.5\ \mu\text{L}$  of water up a height of  $4\text{ mm}$  along a ramp angle of  $\sim 8^\circ$ ; see Figure 19(b). Figure 19(c) depicts the template design used for the PET and paper substrates.

Pumping of liquid against gravity by the wedge-shaped superhydrophilic pattern works well also for the liquid bridging/ draining circuit (Figure 16 and Figure 17). A PET substrate was used to create a three-dimensional platform where the substrate had two horizontal parts at two

different elevations, connected by an inclined section. Figure 20 shows selected snapshots as a liquid bridge formed between the two parallel wedge-shaped tracks A and B on the horizontal part (I) of the substrate, and then the bridged liquid was pumped along the third track C (II), laid on the inclined part of the substrate at  $13^\circ$  tilt up to a height of 4 mm. The bridging, draining and de-bridging modes of liquid transport on the non-planar substrate were similar to those observed on a horizontal surface (Figure 16 and Figure 17), with the only difference that the pumping rate for the inclined substrate was  $\sim 156 \mu\text{L s}^{-1}$  as opposed to  $357 \mu\text{L s}^{-1}$  on the horizontal plane. All of the cases presented in Figure 19 and Figure 20 showed pumpless transport, where the spatial difference of surface energy on the substrate is utilized to overcome the viscous resistance and gravity force. In principle, the technique works with a combination of up and down ramps, thus offering limitless possibilities for the construction of 3-D microfluidic arrangements that are capable of transporting liquid at considerable rates. The present examples demonstrate the prospect of complicated microfluidic networks (e.g., open channels in the form of crossovers) on microfluidic platforms for enhanced device functionality.

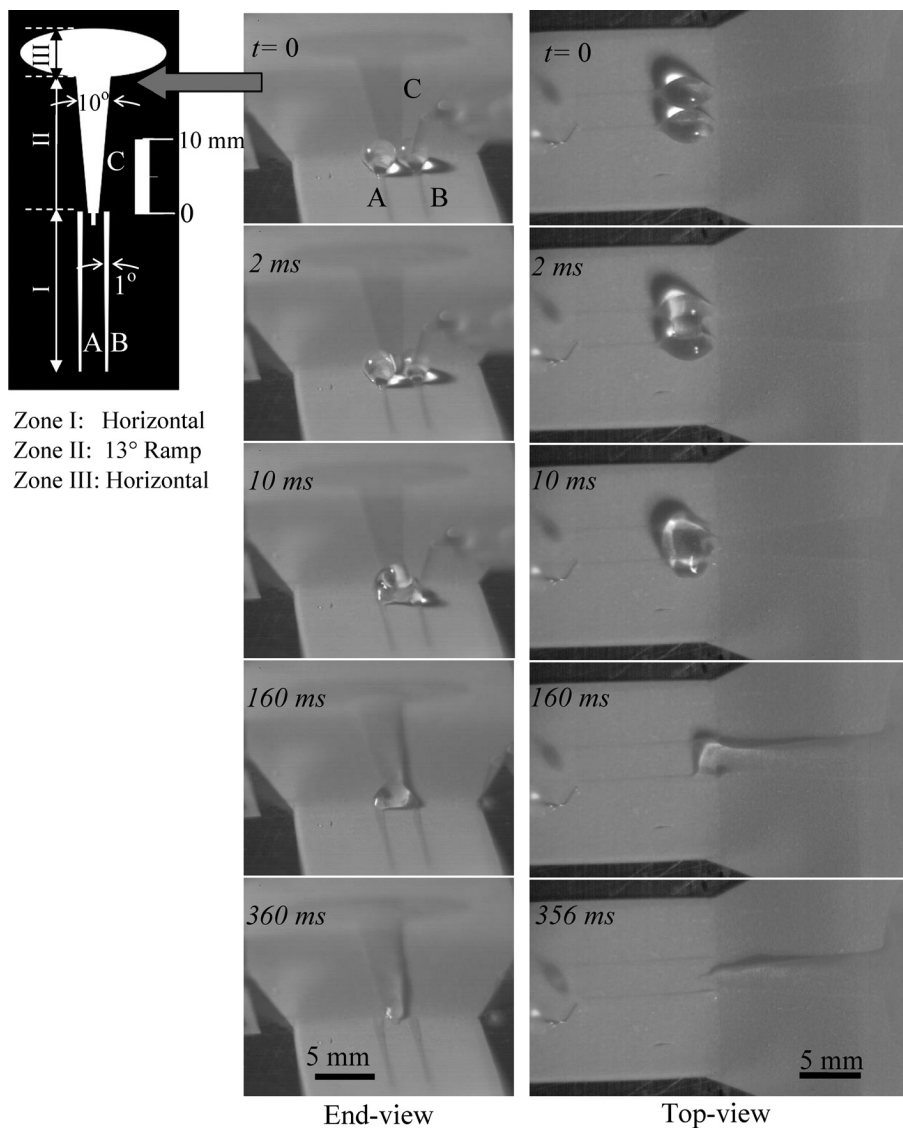


Figure 20. Snapshots of liquid transport up an inclined plane through a  $13^\circ$  upslope (height of  $\sim 4 \text{ mm}$ ) on a droplet bridging and draining circuit (inset at the top left corner) after dispensing  $56.4 \mu\text{L}$  of liquid. Elevated end view (left column) and top view (right column), as taken from two distinct runs under the same conditions. The needle dispenser can be seen on the left of each top-view image.

## CHAPTER 4

# PUMPLESS TRANSPORT AUGMENTING DROPWISE CONDENSATION

Previously published as *Ghosh, Aritra, Sara Beaini, Bong June Zhang, Ranjan Ganguly, and Constantine M. Megaridis. "Enhancing dropwise condensation through bioinspired wettability patterning." Langmuir 30, no. 43 (2014): 13103-13115.*

### 4.1 Introduction

The process of condensation not only is prevalent in nature, but also plays a critical role in a large spectrum of engineering applications, ranging from heat exchangers in power and process industries(87) and fuel cells(88), to electronics thermal management(89), heating ventilation and air conditioning (HVAC)(90) and water harvesting from the atmosphere(91). From a thermodynamic perspective, achieving high condensation heat flux under the minimum temperature difference between the dew point and the condensing surface is most desirable, because this improves the efficiency of energy conversion devices(92). Condensation heat transfer occurs in two primary modes, dropwise condensation (DWC) and filmwise condensation (FWC), the former offering an order of magnitude higher heat transfer coefficient (HTC) than the latter(93; 94). However, achieving sustained DWC in engineering applications has remained an elusive task despite intense research for over half a century.

The presence of a distinct interface boundary between the vapor and liquid phases and its interaction with the heat transfer surface (a thermally conducting solid substrate in most cases) offer a unique opportunity to alter DWC heat transfer by tuning the wettability of the underlying solid. An ideal condensing surface should provide sufficient sites for nucleation and rapid drainage of the condensate formed to expose pristine regions for re-nucleation and further drainage(95; 96). Droplet nucleation is favored on hydrophilic (water-loving) surfaces(97; 98), whereas hydrophobic (water-deploring) surfaces with moderately low contact angle hysteresis promote early shedding of condensate droplets under gravity, thus preventing or delaying the transition to FWC(96).

Extensive theoretical(99) and experimental(100) investigations have shown that liquid droplets on a condensing substrate pose a finite thermal resistance due to conduction through the liquid mass of the droplet. Rose(93) showed that reducing the size of the largest departing condensate droplets in DWC reduces the thermal resistance, thereby increasing the overall HTC. Gravity, as always, has been the perpetual resort for condensate drainage integrated into the condenser design by researchers(101), where the droplet size has to be  $\sim O(1 \text{ mm})$  before the droplet departs from the surface, reducing HTC significantly. Various methods(102) of enhancing DWC heat transfer by promoting condensate removal on superhydrophobic surfaces have been reported in the literature. Daniel *et al.*(103) showed condensate removal from superhydrophobic surfaces with chemically established spatial surface tension gradients. Miljkovic *et al.*(104) fabricated superhydrophobic condensing surfaces (silanized nanostructured CuO) capable of a 30% enhancement in HTC (as compared to Cu surfaces) by harnessing coalescence induced droplet

jumping as a means of condensate removal in a pure steam environment, and Boreyko and Chen(105) demonstrated self-propelling condensate ejection events in an ambient environment with a noncondensable gas. However, the droplet jumping phenomenon was found to cease under high nucleation density conditions (e.g., under a high degree of subcooling) leading to a flooding condensation mode associated with a significant deterioration in performance(102). Attempts have been made to augment this jumping mode of droplet departure using an electric field(106) or vibration(107). However, the extra energy incurred in creating the electrical or vibrational field counters the very motivation for boosting the net HTC in DWC. Increasing condensate droplet mobility is also achieved by impregnating the roughness structures on superhydrophobic surfaces with oils(108), but the choice of the impregnating liquid limits the range of application.

The ideal wettability of the surface needed for maximizing DWC depends on the condensing environment (e.g., gas-phase temperature, vapor mass fraction, etc.) and the extent of subcooling driving the condensation. Although extensive research efforts have been devoted to developing superhydrophobic surfaces for condensing and removing (via rolloff) smaller-diameter droplets as a means of promoting higher HTC, these approaches have not proven as consistently effective during steady state and may even under perform in both high heat flux applications (typical of condensing scenarios in pure steam environments)(93) or in mild environments (e.g., low heat flux or condensation in the presence of noncondensable gases) as compared to hydrophilic/superhydrophilic condensing surfaces(91). One logical step in designing an efficient surface for DWC is to use the benefits of both hydrophobic and hydrophilic

surfaces. Kumagai *et al.*(109) reported enhanced heat transfer using horizontal strips of organic promoter-coated surfaces to distribute DWC domains in an FWC background. They found an optimum range for the widths of FWC and DWC regions, for which the HTC was maximized. Similar results were also confirmed by Ma *et al.*(110), who enhanced HTC using coexisting dropwise-filmwise condensation (DFC). However, for condensation in the presence of noncondensable gases (NCG), the same group(111) found no observable improvement in HTC in such DFC systems. Varanasi *et al.*(97) showed that by using alternate hydrophobic and hydrophilic regions one can control the droplet nucleation spatially. Mishchenko *et al.*(112) demonstrated that superhydrophobic posts with hydrophilic tips can allow spatial control of the nucleation, growth, and coalescence of microscale water droplets. Enright *et al.*(113) further stressed that use of wettability-patterned surfaces is a promising route in enhancing DWC rates. Thickett *et al.*(114) used a porous network of hydrophilic beads and strands on a hydrophobic polystyrene background on a silicon substrate to quantify the dynamic condensation rates and their dependence on pattern features during DWC of water. A similar strategy has also been adopted by Bai *et al.*(115), who demonstrated fog harvesting using biomimetic islands of star-shaped superhydrophilic domains on a TiO<sub>2</sub>-coated glass substrate. Although they were able to demonstrate the augmentation of water collection using a wettability-patterned substrate, their study did not clearly identify the mechanism responsible for improved water collection so that future designs could be further improved. The same limitation applies to the reports of Chatterjee *et al.*(101) and Derby *et al.*(116), who compared the performance of two designs of hydrophilic patterns (island pattern and tree pattern) on superhydrophobic backgrounds under high heat

flux conditions. Except for the one-island design that offered a 7.6% improvement in HTC over the base case of a homogeneous superhydrophobic surface, they observed a degradation in DWC performance in all other designs. The reason for HTC improvement was attributed to a smaller departing droplet size, but no rationale for the success (or failure) was presented. Contrary to the above findings, Lee *et al.*(91) reported that a uniform hydrophilic surface exhibited better fog capture than a patterned one featuring hydrophilic patches on a hydrophobic background.

As mentioned earlier, the overall performance of DWC depends on several crucial factors, such as the nucleation density and rate, maximum size of the departing droplet, and rapid condensate drainage. Combining more than one or all of these factors to improve the DWC has not been demonstrated in the literature in general, though such a holistic approach has been discussed by Beaini and Carey(117). Also, the complexity involved in the fabrication and durability of the reported surfaces has been a major deterrent toward establishing widespread application in industry.

The objective of the present work is to design wettability-patterned surfaces capable of controlling all of the above three key factors (i.e., achieving optimal spatial nucleation, minimizing the departing droplet size, and facilitating rapid drainage of condensate) necessary for the enhancement of DWC in the presence of NCG. Our facile fabrication technique utilizes the intrinsic wettability of the metal substrate (mirror finish aluminum,  $\theta \approx 78^\circ$ ), thus requiring minimal surface modification and avoiding the use of any surface coatings. Suitably designed superhydrophilic ( $\theta \approx 0^\circ$ ) patterns limit the droplet size on the condensing surface. Extensive quantitative evaluation of the condensate collection rate and HTC are performed in

controlled humidity environments to investigate the specific influence of the wettability patterning on the droplet size and overall heat transfer improvement. Further design improvement has been achieved using wedge-shaped superhydrophilic tracks, which we have previously shown to induce pumpless, high-throughput liquid transport on open surfaces(15). We arranged these tracks in a nature-inspired vein network pattern found in banana leaves. Although leaf vein structures have been adopted earlier for the optimization of transport networks in internal flows (flow through enclosed channels and pipes)(118), they have not been attempted for optimizing transport on open surfaces. The fact that the superhydrophilic tracks exhibit filmwise condensation is harnessed in creating a liquid film curvature gradient that provides efficient capillary pumping along the tracks. Our present design simultaneously achieves the tasks of controlling the condensate droplet size on the condensing surface and at the same time rapidly removing the condensate from the active areas of droplet nucleation and growth, thus enhancing the overall condensation rate. The rapid rate of liquid removal is especially relevant for mitigating condensate blow-off on finned heat exchangers, such as air-handling units and HVAC systems. Condensate blow-off occurs when condensate travels with the air stream, landing downstream of the finned coils, in turn affecting both the efficiency of the heat exchanger and the undesired biological growth in the ducts. Instead, wettability patterning technologies may be implemented to ensure condensate drainage directly under the coils into the drain pan to avoid undesired condensate remaining in the occupied space(119; 120). Figure 21 summarizes some of the recent works on enhanced DWC and classifies them on the basis of the working fluid, environment, and condensate removal techniques.

ref	working fluid	ambient conditions (temp $T_\infty$ , pressure $p$ , gas/vapor flow velocity $V$ )	condensate removal method
9	air/water vapor	$T_\infty = 22$ °C, 70% relative humidity (RH)	coalescence-induced drop jumping, random sweeping on horizontal superhydrophobic surface
14	pure steam	$V \approx 4.5$ m/s	gravity-induced sweeping on vertical hydrophobic surface
15	pure steam	$V \approx 0.02$ – $5$ m/s, $p = 445$ kPa, $0.5$ °C superheat	gravity-induced sweeping on vertical wettability-patterned surface
17	saturated steam	$T_\infty = 100$ °C	capillary force by wettability gradient on horizontal surface
18	saturated steam	$17.5$ °C $< T_\infty < 27$ °C, $2$ kPa $< p < 3.6$ kPa	coalescence-induced jumping and gravity from horizontal superhydrophobic tubes
20	saturated water vapor both with and without NCG	$p \approx 2.7$ kPa, $15$ °C $\leq T_\infty \leq 82$ °C	electric-field-enhanced, coalescence-induced jumping on superhydrophobic horizontal surface (both against and with gravity)
22	saturated steam	$p = 60$ kPa, $T_\infty = 86$ °C	gravity-induced sweeping on lubricant-impregnated vertical surface (low hysteresis)
24	pure steam	$T_\infty = 100$ °C	gravity-driven drainage in dropwise filmwise coexisting mode over horizontally patterned regions on vertical tube
25	steam/air		gravity and sweeping by falling droplets on vertical wettability-patterned surface
28	humidified air	86% RH, $1.4$ L $\text{min}^{-1}$ ( $V \approx 0.41$ $\text{ms}^{-1}$ ); 79% RH, $9.8$ L $\text{min}^{-1}$ ( $V \approx 2.78$ $\text{ms}^{-1}$ )	gravity- and capillary-force-induced droplet removal from vertical wettability-patterned surface
30	wet steam	$p = 350$ – $400$ kPa, $0.2$ – $0.95$ dryness fraction	gravity- and capillary-driven condensate removal on wettability-patterned surfaces
31	steam–air mixture	$T_\infty = 85$ – $95$ °C	gravity-induced drainage from vertical mirror finish and wettability-patterned surfaces
39	saturated steam	$p = 1$ – $1.5$ bar	gravity, falling droplets on ion-implanted hydrophobic vertical condenser surface
45	air–steam mixture (air molar concentrations from 0.5–5%)	$\Delta T = 5$ – $40$ K, $V < 0.8$ $\text{ms}^{-1}$ , $p = 0.1$ and $0.16$ MPa	gravity-induced removal from a vertical surface
47	humid air (vapor mass fraction varying from 0.05 to 0.41 kg/kg of mixture)	$T_\infty = 65$ – $95$ °C, $V = 2$ – $12$ $\text{ms}^{-1}$	gravity-induced removal and falling droplets from vertical, hydrophobic surface
54	saturated water vapor	$T_\infty = 110$ °C, $V = 6, 12,$ and $18$ $\text{ms}^{-1}$	droplet sweeping due to vapor shear and gravitational forces on vertical superhydrophobic condensing surface

Figure 21. Recent Studies on Enhanced Dropwise Condensation (DWC), as Classified on the Basis of the Working Fluid, Ambient Gas Environment, and Condensate Removal Approach

## 4.2 Materials and methods

### 4.2.1 Materials

The only chemical used was hydrochloric acid (Sigma-Aldrich, 36% in 3 *M* aqueous solution). The substrate was a mirror-finish aluminum plate (multipurpose polished aluminum alloy 6061, 2 *mm* thick, McMaster Carr) coated with a protective polymer sheet, which was ablated as needed for the patterns using CO<sub>2</sub> laser cutting. Etching the exposed mirror-finish aluminum surface by HCl imparted the required micro and nanoscale roughness and promoted superhydrophilicity(121).

### 4.2.2 Sample preparation

We used a facile and scalable approach to fabricate samples with alternating regions of contrast wettability per the desired designs. A computer-aided design (CAD) file for each sample design was fed as a vector image into a computer controlled CO<sub>2</sub> laser, after which the laser (5% power at 6.7% speed) cut through the polymer cover sheet on top of the substrate (Figure 22a). The polymer sheet was then selectively peeled with tweezers (Figure 22b), and the entire substrate was immersed in the HCl solution for 15 min. After the acid bath, the substrate was washed with a copious amount of DI water to remove traces of acid, followed by boiling in DI water for 1 h (Figure 22c). This rendered the unmasked region superhydrophilic with a contact angle close to 0°. The remaining protective polymer cover was then peeled off to expose patterns of the underlying mirror-finish aluminum, whose intrinsic wettability established the mildly hydrophilic domains ( $\theta = 78.2 \pm 2^\circ$ , see Table III in Appendix B). This method circumvented the use of fluorinated chemicals, which have generally been used by others

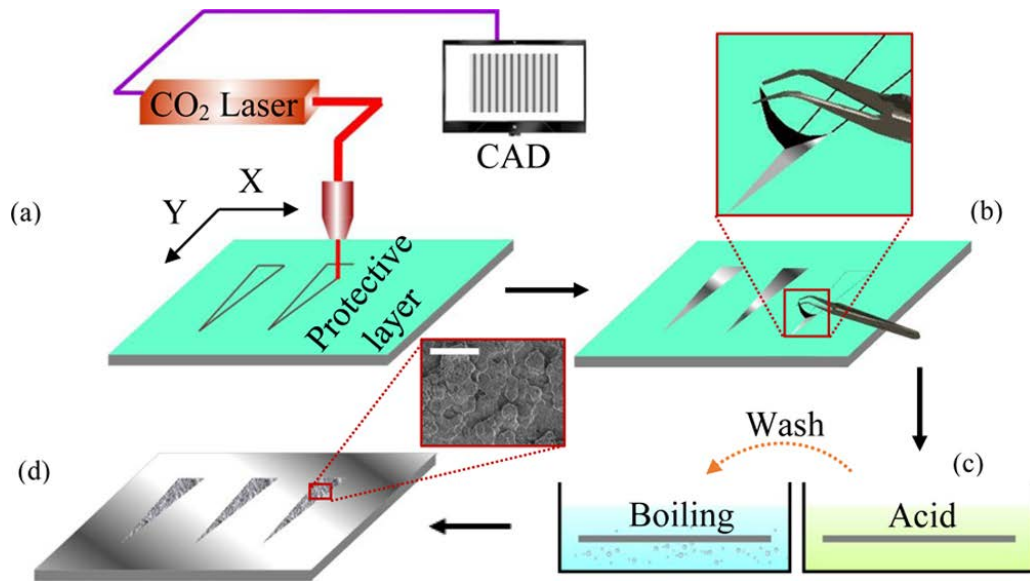


Figure 22. Schematic of the sample-fabrication process. The protective polymer sheet on the aluminum substrate (as purchased) is laser cut using a precise CAD design (a) and then selectively peeled off, exposing selected regions of the aluminum underneath (b). (c) The substrate is subsequently exposed to selective chemical etching (in a 3 M HCl acid bath for 15 min), followed by passivation via boiling in water (1 h). (d) Finished sample with a wettability-patterned region after the polymer mask has been removed. The exposed region (wedge-shaped in this case) became superhydrophilic, while the rest of the sample remained hydrophilic (intrinsic wettability of aluminum) with  $\theta \approx 78.2^\circ$ . The inset in (d) shows a scanning electron micrograph of the superhydrophilic triangle region. The scale bar in the inset denotes  $100 \mu\text{m}$ .

for treating surfaces for enhanced DWC(114). The final outcome of the entire process was a wettability-patterned substrate with alternate superhydrophilic and hydrophilic mirror-finish domains (Figure 22d).

### 4.2.3 Characterization

Surface characterization was performed by measuring water contact angles and conducting scanning electron microscope (SEM) imaging in regions of interest in the sample. We used a custom-built goniometer with a CCD camera (Pulnix, model TM-9701) mounted with an OPTEM ZOOM 100 lens. Droplets ( $5 \mu\text{L}$ ) were backlit by a cold light source (FOSTEC, 8375) to avoid heating the liquid. Standard image analysis software (IMAGE-J) was used to calculate sessile droplet contact angles as well as advancing and receding angles.

### 4.2.4 Experiments and image analysis

Condensation experiments were conducted in a temperature- and humidity-controlled environmental chamber (ESPEQ, SH-641) at various dry bulb temperature (DBT) and relative humidity (RH) settings. Care was taken to preclude possible contamination, such as that due to hydrocarbons(122). Figure 23 shows a schematic of the experimental setup. The sample was mounted vertically using thermally conductive adhesive tape (McMaster Carr, 6838A11) on the cold plate of a Peltier cooler (TeTech, CP-061). The subcooling of the sample surface was maintained by setting the Peltier cooler at a temperature of  $0 \text{ }^\circ\text{C}$ . The temperature readings from the sample surface were higher than the Peltier set temperature owing to the thermal resistance of the Peltier base plate and the contact resistance between the sample and the underlying Peltier base plate. The sample surface temperature was monitored by four K-type thermocouples (bead diameter  $0.13 \text{ mm}$ , Omega) inserted into  $800 \mu\text{m}$  diameter holes drilled in the sample plate beneath (and parallel to) the condensing surface and secured in place with thermally conductive silver paste (Omegatherm 201, Omega). The temperature was recorded

in real time using a data acquisition system (Omega, USB 2400 series) at a 1  $Hz$  sampling frequency. Experiments were repeated under similar conditions for the control case (mirror-finish bare aluminum surface) and the wettability-patterned surfaces. Condensate that drained from the vertical plate was collected over a specified time period and weighed in a commercial digital balance with an accuracy of 0.01  $g$ . Submillimeter-scale and millisecond duration events of condensation dynamics were imaged at 2000 fps using a high-speed CCD camera (Phantom Miro 310) with an OPTEM ZOOM 100 lens; suitable illumination for high-speed imaging was provided by a light source (FOSTEC, 8375). The realtime condensate droplet distribution was recorded using a standard DSLR (Canon Rebel T1) camera mounted with a macro telephoto zoom lens (Sigma 70 – 300  $mm$ ). Image processing was done using MATLAB analysis scripts.

### **4.3 Results and discussion**

#### **4.3.1 Control of condensate droplet size: Proof of concept**

We hypothesize that by providing a wettability-patterned substrate comprising juxtaposed regions of high and low wettability, a sustained mechanism for the control of droplet growth and condensate drainage can be achieved. Although the less-wettable hydrophilic/mirror-finish aluminum (with  $\theta \approx 78^\circ$ ) area of the surface offers the favored sites for droplet nucleation and growth in a dropwise manner, the more wettable regions (chemically-etched superhydrophilic domains) exhibit filmwise condensation and offer a path for condensate drainage; see Figure 24a.

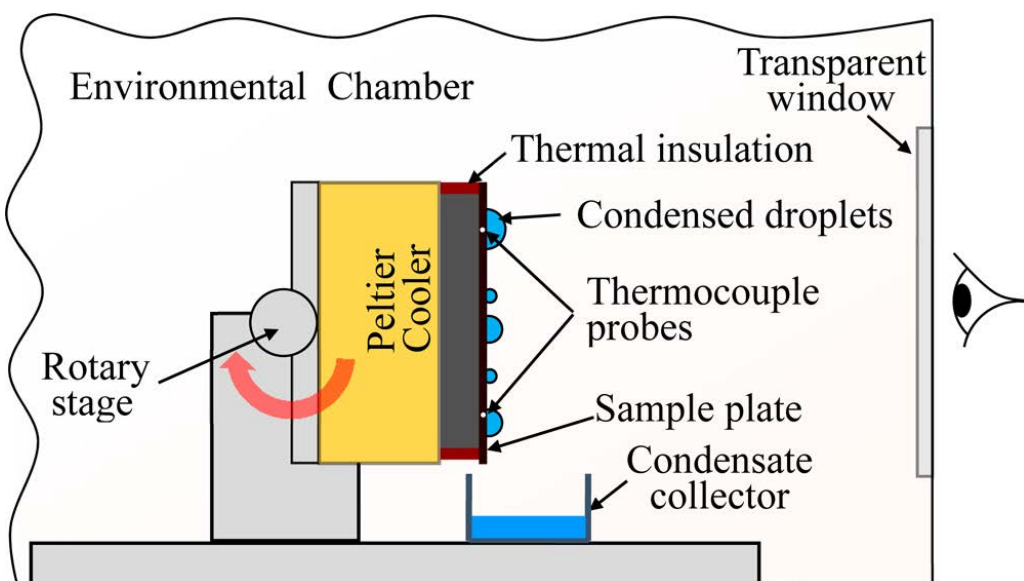


Figure 23. Condensation experiment setup. Test samples are mounted on a computer-controlled Peltier cooler, which maintains the substrate surface temperature at a set point. The sample is exposed to controlled humidity and temperature in an environmental chamber. Droplet coalescence and shedding events are visualized through a heated (to prevent fogging) glass window (right) using high-speed photography.

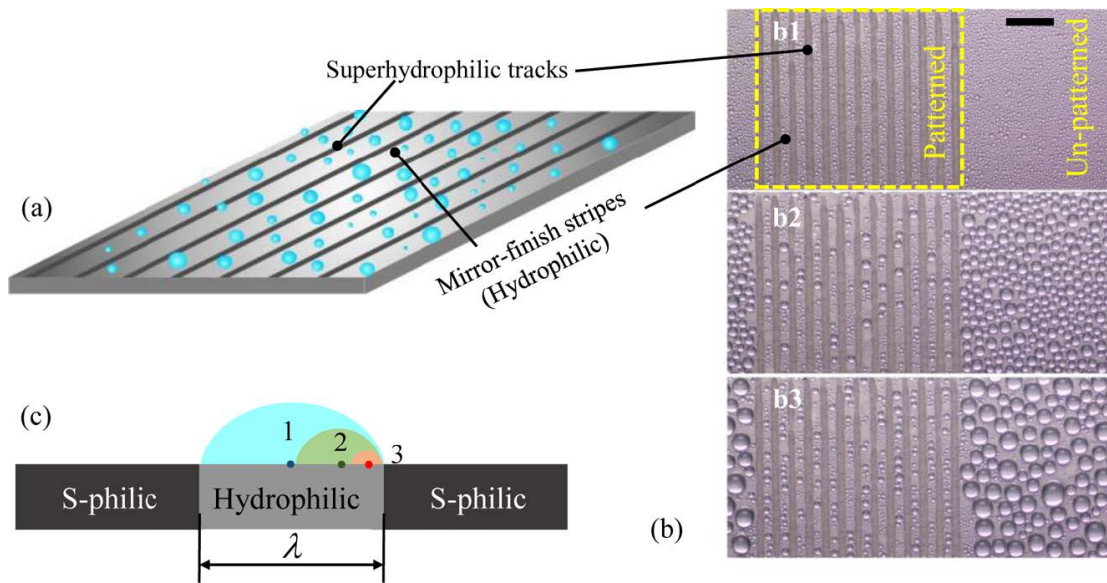


Figure 24. (a) Schematic of DWC on the wettability-patterned substrate. (b) Comparison of condensate drop size evolution with time on the patterned (left) and unpatterned (right) regions of the substrate. The patterned region featured equally spaced  $800 \mu\text{m}$  wide mirror-finish (mildly philic) parallel stripes separated by  $300 \mu\text{m}$  superhydrophilic (S-philic) tracks. The period between recorded images is  $10 \text{ min}$  (top to bottom). The unpatterned region exhibits a much greater droplet size than does the patterned region. The scale bar (black) denotes  $3 \text{ mm}$ . (c) The largest condensate droplet size (shown in different colors) depends on the location of initial nucleation (dark dots) on the mildly philic region. The closer the point of nucleation to the wettability contrast line, the smaller the size of the departing droplet (absorbed into the adjacent film covering the S-philic track).

To test our hypothesis, we compare the condensation behaviors on both unpatterned mirror-finish (control) and wettability-patterned (superhydrophilic-hydrophilic) surfaces in a controlled environment of 20 °C DBT and 80 % RH. As the plate temperature was brought below the dew point temperature (16.5 °C in this case), condensate droplets started to appear on the less-wettable mirror-finish parts of the substrate; no droplets were seen on the superhydrophilic tracks of the patterned substrate because the condensate spread quickly as a result of hemiwicking(25). With the passage of time, the droplets on the unpatterned surface grew in size; neighboring droplets merged as they touched, subsequently shedding off by gravity when they grew beyond a threshold size ( $\sim$  capillary length of water), where the weight of the liquid exceeded the pinning force due to contact angle hysteresis. Departed droplets left behind a pristine region on the condensing surface, where fresh nucleation and regrowth of condensate droplets could take place anew. This cyclical phenomenon of nucleation and droplet growth followed by droplet removal is referred to as droplet rejuvenation. All of these features are standard traits of DWC(123). However, the unique feature in the present case was that the maximum droplet sizes appearing on the wettability-patterned surface were smaller than their counterparts on the unpatterned surface. Figure 24b shows the time evolution of the condensate droplets on the unpatterned and patterned regions at  $t = 0$  (b1) as well as after 10 *min* (b2) and 20 *min* (b3). Droplets on the striped surface are visibly smaller than those on the unpatterned surface in Figure 24b2, b3. Moreover, the droplet rejuvenation frequency was found to be higher for the patterned surface than for the unpatterned (control) plate. It is important to note that the present environmental conditions combined with the low cooling rate ( $\sim 1 \text{ kW m}^2$ ) did

not cause a transition from DWC to FWC on the polished aluminum (Figure 45 in Appendix B). The duration of each test was typically between 2 and 10 h, and each sample was tested repeatedly with reliable performance over 150 h of cumulative operation.

Droplet departure from the less-wettable domains (where DWC occurs) is expected to take place primarily by way of liquid drainage along the superhydrophilic tracks. The schematic in Figure 24c shows that the departing droplet size is largely dependent on the location of its initial nucleation site on the mirror-finish strip of width  $\lambda$  interspaced between two successive superhydrophilic tracks. A droplet nucleated from the center of the mirror-finish region is likely to grow until its base periphery touches a superhydrophilic track on one or both ends; the liquid is then pumped rapidly into the superhydrophilic track because of the capillary pressure of the droplet. Clearly, a droplet nucleated closer to the wettability transition line (demarcating the superhydrophilic and hydrophilic strips) would be swept into the superhydrophilic region after attaining a radius smaller than when nucleated closer to the center of the hydrophilic strip. For example, droplet 1 in Figure 24c (the darker dot denotes its initial nucleation site), which originated near the central axis of the mirror-finish strip, would reach the superhydrophilic strips at a larger drop radius as compared to droplets 2 and 3, which nucleated off of the axis and closer to the wettability transition line. As soon as a growing droplet touches the edge of the liquid-occupied superhydrophilic region, the capillary pressure difference between the curved droplet and the liquid in the superhydrophilic track leads to rapid pumping of the droplet content into the liquid film, which is maintained by the combined effects of FWC and hemiwicking. Condensation of liquid on the existing film takes place at a much lower

rate because homogeneous nucleation on the film is less favored compared to heterogeneous nucleation on a solid(124). Nonetheless, the liquid film plays a critical role in droplet removal and drainage of the liquid.

Figure 25 a shows what follows after a water droplet is placed on top of the wettability contrast line on a horizontal substrate; the  $5 \mu L$  droplet is found to transit across the wettability contrast in about  $35 ms$ , corresponding to a volume flow rate of  $\sim 134 \mu L s^{-1}$ . Considering that this occurs across a wettability-contrast line span of  $\sim 2 mm$  length, this represents a very high transport rate. In a condensing scenario, such rapid transport offers an effective mechanism of surface rejuvenation and condensate drainage (Figure 25 b1-b4), where a condensate droplet is seen to touch the superhydrophilic line on the vertically mounted condenser plate and then is pumped away because of the capillary pressure difference. Theoretically, this mode of capillary pumping on the wettability-patterned surface would produce a maximum possible droplet diameter equal to the width  $\lambda$  of the mirror-finish stripe. However, careful observation of Figure 24 b and Figure 25b reveals that the theoretical maximum droplet diameter represents only a small subset of the droplets that grow in the DWC tracks. In fact, the maximum droplet size reached for most droplets growing in the DWC stripes before being sucked into the FWC domains was considerably smaller than this theoretical value, suggesting that other mechanisms of droplet removal may also be at play.

High-speed imaging of the condensate departing from the mirror-finish regions of the vertically mounted condenser plate revealed that neighboring droplet coalescence often led to lateral spreading/bulging of the coalesced condensate, allowing it to reach the edge of the superhy-

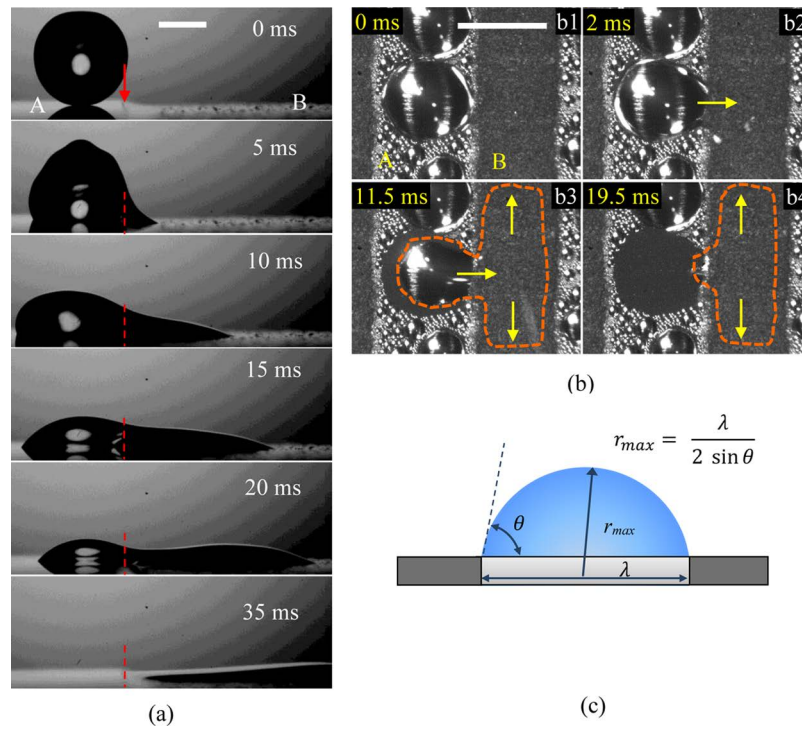


Figure 25. (a) Typical dynamics of the capillary-driven motion of a drop placed across the wettability transition line (shown by the red arrow and dashed line) that separates the mirror-finish (A) and superhydrophilic (B) domains. The same mechanism affects condensate removal by capillary pumping along the superhydrophilic track. (b) A droplet growing (b1) on the hydrophilic DWC region (A) adjacent to a superhydrophilic track (B) eventually reaches the edge of the track (b2). Capillary pressure in the droplet pumps the liquid (b3, b4) rapidly into the adjacent liquid film occupying region B. The white scale bars in the top image denote 1 mm both in (a) and (b). (c) Relation between the theoretical maximum droplet diameter and the width  $\lambda$  of the hydrophilic track.

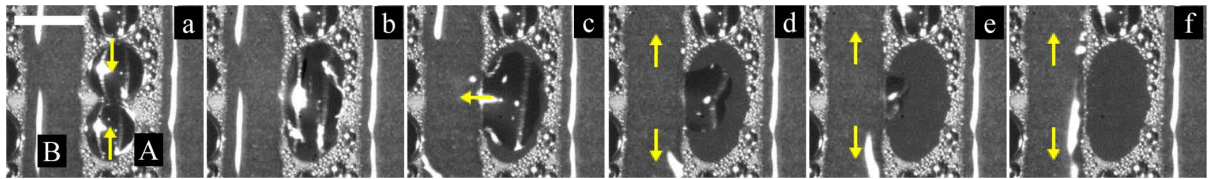


Figure 26. (a) Condensate removal induced by droplet coalescence. Two isolated neighboring droplets (frame a) grow on the hydrophilic region (A) until they touch and coalesce (frame b); inertia of the liquid in the coalescing droplets leads to lateral widening of the new droplet, which then touches the adjacent superhydrophilic (B) track. The liquid is then pumped into the superhydrophilic track by capillary pressure (frames c-f). The white scale bar denotes  $1\text{ mm}$ . Images are captured every  $5\text{ ms}$ . Yellow arrows indicate the direction of condensate flow. After the droplet is drained into the liquid film (f), the pristine surface left behind offers new sites for sustained nucleation.

drophilic track prematurely, thus being drawn into it before any of the two coalescing droplets attained a larger size. Figure 26 shows such an event, where two individual drops of size  $\sim 800\ \mu\text{m}$  grow from the central region of the superhydrophilic strip (Figure 26a) and coalesce (Figure 26 b) before either of them reaches the strip edge. Momentum resulting from the surface energy minimization during coalescence led to transverse spreading of the coalesced droplet (Figure 26c), which brought the new droplet into contact with the superhydrophilic region on its left, thus draining it subsequently (Figure 26c-f). In this case, the two initial droplets were removed before they could grow further to the size of the full strip width  $\lambda$  ( $1200\ \mu\text{m}$  in this case).

#### 4.3.2 Dimensioning patterns for drop size control

Having established the ability of the patterned substrate to reduce the maximum size of departing droplets in the DWC domain, we then quantified and evaluated the control of droplet

size distribution by varying the dimension of the stripe patterns. We chose eight different widths of the mirror-finish stripes, namely,  $\lambda = 400, 600, 800, 1000, 1250, 1500, 2000,$  and  $2500 \mu m$ , covering the practical range for sustained heterogeneous nucleation and DWC. For the first four cases, the intervening superhydrophilic tracks were  $300 \mu m$  wide, and for the rest, the superhydrophilic tracks were  $400 \mu m$ . This was done to accommodate the extra liquid drained from the larger condensing areas with higher  $\lambda$ . A  $12 mm \times 3 mm$  superhydrophilic patch was etched at the bottom of each design (Figure 27) to accumulate the drained condensate. All of the substrates were tested in a condensing environment at  $20 \text{ }^\circ C$  DBT and 80% RH over a duration of 1 h.

Figure 27a shows images that exemplify the variation in droplet size for different values of  $\lambda$ . Droplets grown on the mirror-finish unpatterned surface (Figure 27a) are considerably larger than those observed on the mirror-finish stripes of the patterned regions. The maximum size of the departing droplets from the patterned region was found to increase with  $\lambda$ . To quantify this effect, we recorded still images every 1 min for 30 minutes in a steady condensation scenario and analyzed them using MATLAB. The maximum droplet size in each mirror-finish stripe of the patterned region was calculated through image processing. Only visibly larger droplets were measured in each image, which also included many smaller droplets (that were disregarded in these measurements). The detailed procedure for evaluating  $D_{max}$  is described in Appendix B. More than 150 droplet diameters were measured for each value of  $\lambda$ , and data distributions are drawn in Figure 27b. The box plot presents the median, lower, and upper quartiles (25th and 75th percentiles, respectively) of the data. The space-time averaged largest droplet diameter

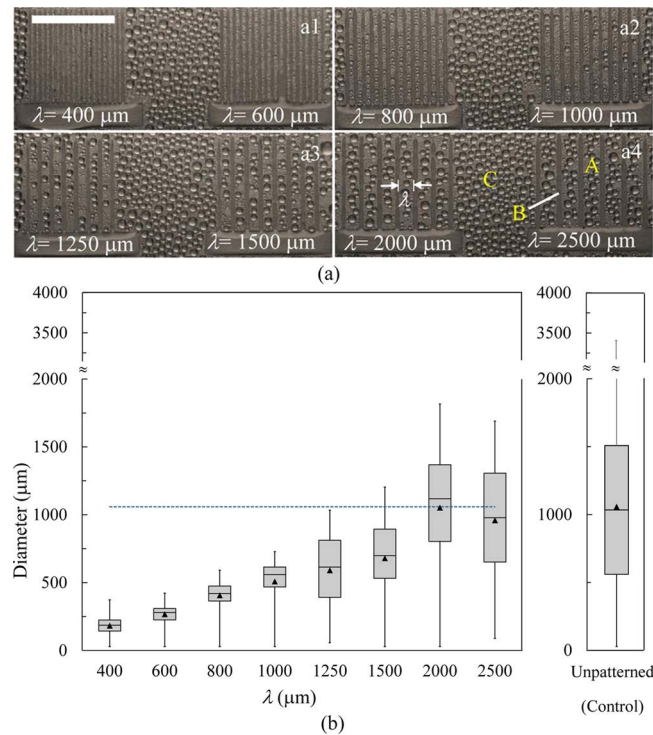
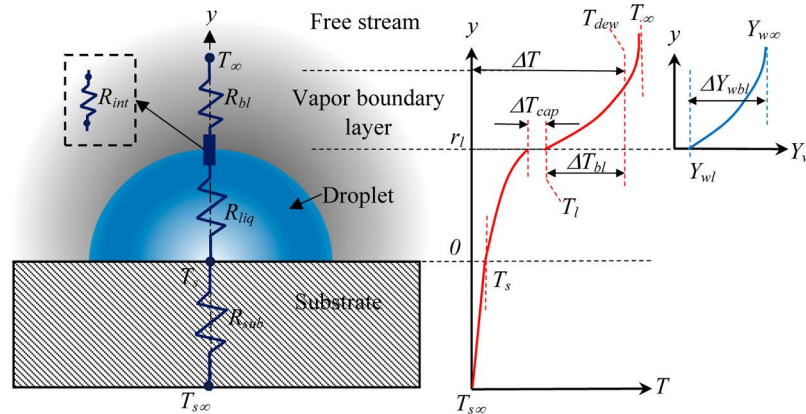


Figure 27. (a) Droplets on patterned condensing surfaces comprising hydrophilic strips (A) of width  $\lambda$  interspaced by superhydrophilic tracks ( $300 \mu\text{m}$  wide in a1 and a2,  $400 \mu\text{m}$  wide in a3 and a4) (B). Region C denotes an unpatterned mirror-finish Al region (similar to A). The scale bar denotes  $11 \text{ mm}$ . (b) Variation of the maximum droplet diameter (averaged over the hydrophilic strips of the patterned surface during a period of 30 min of steady condensation) with  $\lambda$ . The box plot presents the median, lower, and upper quartiles (25th and 75th percentiles, respectively) of the largest droplets recorded at 1 min intervals over the duration of each experiment. The black triangle represents the time-averaged value of the largest departing droplet diameter ( $D_{max}$ ) over the same period. The dashed horizontal line represents the corresponding  $D_{max}$  for the unpatterned region (control surface). Each data point results from more than 150 measurements.

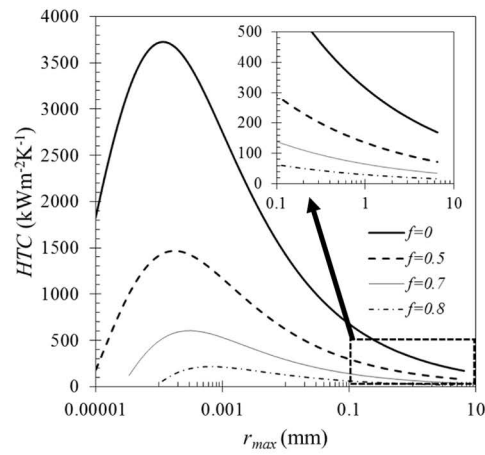
( $D_{max}$ ) for each  $\lambda$  is also plotted in Figure 27b (black triangles). A linear relationship with  $\lambda$  of up to 2000  $\mu m$  is observed for both the median and the time-averaged  $D_{max}$  values in Figure 27b, indicating that the time averaged maximum droplet size is about 42% of the philic strip width. Beyond  $\lambda = 2000 \mu m$ , the change in  $D_{max}$  tapers off. For comparison, the plot for the unpatterned mirror-finish regions (control surface) is also shown separately on the right of Figure 27b. The corresponding  $D_{max}$  is shown by the dashed horizontal line, which was  $\sim 1058 \pm 296 \mu m$ . The comparison of Figure 27b provides clear evidence that the maximum droplet size in the DWC regions can be effectively controlled with suitably patterned wettability domains. All images featured the same resolution (1 mm  $\approx$  107 pixels), and the smallest discernible droplet was  $\sim O(10 \mu m)$ .

### **4.3.3 Dependence of DWC heat transfer rate on departing drop size: Theoretical basis**

The implicit role of the departing droplet size in HTC is better understood from the classical thermal resistance model of DWC that typically considers the heat transfer across a single hemispherical condensing droplet(93). Figure 28 a shows the principal thermal resistances in DWC, which comprise  $R_{liq}$ , the thermal conductive resistance offered by the condensate liquid drop,  $R_{int}$ , the interfacial resistance due to mass transfer across the liquid-vapor interface,(125) and  $R_{sub}$ , the substrate thermal resistance due to droplet recalescence, i.e., the rejection of the latent heat of condensation(126). The temperature difference  $\Delta T = T_{dew} - T_s$  driving condensation is partially offset by the subcooling  $\Delta T_{cap} = 2T_{sat}\sigma_w/r\rho_w h_{fg}$  required to condense on a convex liquid droplet of radius  $r$ (127). The condensation heat flux is strongly affected



(a)



(b)

Figure 28. (a) Thermal resistance model of a condensate droplet under the water vapor + NCG condition (left) and representative temperature ( $T$ ) and vapor mass fraction ( $Y_w$ ) plots along the radius of the droplet (right). (b) Variation of the DWC heat transfer coefficient with the maximum departing droplet size following the Rose model and various values of  $f = \Delta T_{bl}/\Delta T$ , representing the extent of temperature difference occurring across the vapor + NCG boundary layer. The inset in (b) is a blowup over the range of droplet radii that can be controlled by wettability patterning.

by the presence of noncondensable gases (NCG)(128). The presence of air or other NCG adds a diffusion resistance ( $R_{bl}$ ) to the vapor-air boundary layer(129) and alters the relative contributions of latent and sensible heat transfer(130).

Although the process of condensate droplet nucleation, growth, and ultimately shedding is a transient phenomena, the drop-size distribution over a finite area of condensing surface follows a statistically time-invariant pattern. Droplets of different size coexist on the condensing surface, ranging from a few nanometers ( $r_{min}$ ) to  $\sim 1 \text{ mm}$  ( $r_{max}$ ). The smallest viable droplet size is obtained from thermodynamics as  $r_{min} \approx 2T_{sat}\sigma/\rho_w h_{fg}\Delta T$ (124). For a nonpatterned substrate, the largest radius  $r_{max}$  of a droplet that can be dislodged by gravity from an inclined (at an angle of tilt  $\alpha$ ) condenser surface depends on the liquid surface tension  $\sigma$ , contact angle  $\theta$ , and contact angle hysteresis (the difference between the advancing and receding angles,  $\theta_a$  and  $\theta_r$ , respectively) and varies as(131);

$$r_{max} = \left[ \frac{3\sigma}{\rho g \sin \alpha} \frac{(\cos \theta_r - \cos \theta_a) \sin \theta}{(2 - 3 \cos \theta + \cos^3 \theta)} \right]^{1/2} \quad (4.1)$$

Considering the values  $\theta_a = 106.8^\circ$ ,  $\theta_r = 72.8^\circ$ , and  $\theta = 78.2^\circ$  for the mirror-finish surface (Table V in Appendix B),  $\alpha = 90^\circ$  (vertically-mounted plate),  $\sigma = 72 \text{ mN m}^{-1}$  for water at room temperature, the theoretical upper limit of droplet size in the mirror-finish region of the plate in Figure 24b is  $\sim 3 \text{ mm}$  (the observed largest radius in Figure 27a is about  $1.6 \text{ mm}$ ). The overall condensation heat flux on the substrate can be evaluated by integrating the heat flux through each droplet base (as obtained from the thermal resistance model described in Figure 28a) over the entire spectrum of droplet sizes ( $r_{min} < r < r_{max}$ ). A rough estimate of

the HTC for pure steam condensation can be obtained from the thermal resistance model of Rose(132) and the condensate drop size distribution model of Le Fevre and Rose(133), ignoring the minor limitations of the models(134) as(134),

$$HTC = \frac{1}{\Delta T} \frac{1}{3r_{max}^{1/3}} \int_{r_{min}}^{r_{max}} \left\{ \frac{\Delta T - \left( \frac{2\sigma T_{sat}}{r\rho_w h_{fg}} \right) - \Delta T_{bl}}{\left[ \frac{2r}{3k_w} + \frac{T}{\rho_v h_{fg}^2} \left( \frac{\gamma+1}{\gamma-1} \right) \left( \frac{R_g T}{2\pi} \right)^{1/2} \right]} \right\} r^{-2/3} \quad (4.2)$$

The term  $\Delta T_{bl}$  in the numerator of the integrand is introduced to account for the influence of NCG, which is not considered in the original expression of Rose (93). Early experiments in the literature have suggested that the HTC may degrade by up to 30% during DWC with a mere 0.5% in volume concentration of an NCG(130). Typically, in a humid air condensing scenario, the NCG mass fraction increases from the free stream toward the droplet surface (with a corresponding decrease  $\Delta Y_{wbl} = Y_{w\infty} - Y_{wl}$  in vapor mass fraction), and a radially inward temperature drop ( $\Delta T_{bl} = T_{dew} - T_l$ ) is established around each droplet (Figure 28a). Both  $\Delta Y_{wbl}$  and  $\Delta T_{bl}$  vary across the concentration and thermal boundary layers over the condensing droplet and are functions of the vapor mass flux, droplet radius, and free stream convective conditions(135). The vapor condensation mass flux, however, is negatively influenced by  $\Delta T_{bl}$  (because it acts to reduce the available temperature difference driving the condensation); see the numerator in Equation 4.2. Therefore, an estimation of  $\Delta T_{bl}$  and the corresponding condensation rate would require an elaborate solution of the coupled energy and water vapor species equations(136). One plausible simplification can be adopted by assuming a fractional reduction

of the effective driving temperature difference, which we denote as  $f = \Delta T_{bl}/\Delta T$  to evaluate the integral in Equation 4.2.

Figure 28b shows the typical variation in HTC as computed from Equation 4.2 as a function of the maximum departing droplet size for a representative subcooling  $\Delta T = 10 K$  and for four different  $f$  values ranging from zero (i.e., pure steam) to 0.8 (corresponding to the  $\Delta T_{bl}$  formed across the vapor-NCG boundary layer around a  $830\mu m$  radius droplet condensing in an environment of  $Y_{w\infty} = 0.011$  at an average condensation mass flux of  $0.003 kg m^{-2} s^{-1}$ ; see Appendix B). A larger value of  $f$  may also ensue if a greater percentage of NCG exists in the free stream. The trend in the HTC curves in Figure 28b matches that in the literature for DWC(137). In Figure 28b, the HTC is found to increase with  $r_{max}$  for droplet radii below  $0.1 \mu m$  ( $r_{max} = 0.5D_{max}$ ) primarily because of the influence of the capillary temperature depression ( $\Delta T_{cap}$ ) across the curved droplet interface and the interface thermal resistance. For  $r \geq 0.1 \mu m$ , HTC decreases progressively with  $r_{max}$  because of the increased contribution of the condensate thermal resistance. The inset of Figure 28b shows the range over which  $r_{max}$  can be controlled (e.g., by altering the widths  $\lambda$  of the mirror-finish strips) from  $100 \mu m$  (the mean droplet radius for  $\lambda = 400 \mu m$ ) to  $\sim 2.8 mm$  (capillary size of water). The plots indicate that HTC can be improved by nearly 200% by reducing  $r_{max}$  from  $2.8 mm$  to  $110 \mu m$ . Figure 28b also indicates that the HTC becomes progressively larger as the condensate droplets are removed at smaller  $r_{max}$  values.

However, in practice, the resolution of wettability patterns below  $\lambda = 400 \mu m$  becomes a practical issue. The foregoing theoretical analysis is useful only as an order of magnitude

estimate of heat transfer improvement by exerting droplet size control. In practice, the extent of  $\Delta T_{bl}$  is influenced by the macroscopic flow parameters over the condensing plate(138), the thermal and vapor boundary layer profiles, and the spatial variation of the droplet distribution on the condensing surface. Therefore, an accurate estimation of the HTC warrants carefully designed experimentation.

#### 4.3.4 Water collection tests

To quantify the benefit of controlling the maximum droplet size in improving DWC heat transfer, condensation experiments were performed under two controlled environment conditions: (1) condition C1: 20 °C DBT, 80% RH (dew point  $\sim$  16.5 °C), (2) condition C2: 35 °C DBT, 80% RH (dew point  $\sim$  31 °C). The experimental conditions and results are summarized in Table III. Condensate collection was recorded in 2 to 3 h spells of multiple runs. We tested the performance of the wettability-patterned surface with straight stripes of mirror-finish (less wettable) regions with  $\lambda = 1200 \mu m$  interspaced by  $800 \mu m$  wide superhydrophilic tracks. The patterning pitch (distance between two consecutive philic strips) was so chosen that the overall ratio of hydrophilic to superhydrophilic areas was 3:2. For the mirror-finish plate (control), condensate collection rates were  $0.69 \pm 0.01$  and  $1.61 \pm 0.01 L m^2 h^{-1}$  for operating conditions C1 and C2, respectively. The overall heat transfer in the presence of NCG has both sensible and latent components(139). Although the driving temperature difference for the sensible part is the difference between the ambient DBT ( $T_{\infty}$ ) and the substrate temperature ( $T_s$ ), the latent part is caused by the difference between the ambient dew point temperature ( $T_{dew}$ ) and  $T_s$ . The sensible component was not measured in the present configuration because its contribution

would remain the same for the bare and patterned substrates under identical  $T_\infty$  and  $T_s$ . The average surface temperatures of the bare plates for conditions C1 and C2 were  $2.2 \pm 0.4$  and  $18.2 \pm 0.5$  °C, respectively, whereas those for the patterned plate remained within  $\pm 0.5$  °C of the respective control cases. This corresponded to  $(T_\infty - T_s)$  values of  $\sim 18$  and  $17$  K, respectively for conditions C1 and C2. The advective sensible heat flux resulting from this temperature difference is estimated to be on the order of  $0.01 \text{ kW m}^{-2} \text{ K}^{-1}$  (considering forced convection over the  $12.5 \text{ cm} \times 85 \text{ cm}$  flat test specimen and a free-streamflow velocity of  $\sim 1 \text{ m/s}$ ), thus being much smaller compared to the latent component of heat flux. In evaluating the latent heat transfer coefficient, it may be noted that the difference between the ambient dew point and the substrate temperature is responsible for driving the net water vapor flux toward the substrate and subsequent condensation on it. Therefore, the latent contribution of the overall HTCs(140) is evaluated by;

$$HTC = \frac{\dot{m}_w h_{fg}}{T_{dew} - T_s} \quad (4.3)$$

Table III\* (i) Patterned with straight lines, and (ii) bioinspired interdigitated wettability patterns. The patterned surfaces performed better than the control surface for both environmental conditions. The interdigitated pattern is more effective in the harsher situation (C2) compared to the straight-line patterned sample. The improvement is solely attributed to the geometric shape of the wettability patterning of the substrate.

The  $\dot{m}_w$  value in Equation 4.3 was obtained from the water collection data, whereas the pertinent subcooling  $\Delta T = T_{dew} - T_s$  was calculated from the average dry and wet bulb thermometer readings and the thermocouple readings over the duration of each experiment. The

	C1	C2
dry bulb temperature ( $^{\circ}C$ )	20	35
relative humidity (%)	80	80
$T_{dew}$ ( $^{\circ}C$ )	16.5	31
plate temp, $T_s$ ( $^{\circ}C$ )	$2.2 \pm 0.4$	$18.2 \pm 0.5$
$\Delta T = T_{dew} - T_s$ ( $^{\circ}C$ )	14.3	12.8
ambient vapor mass fraction(kg of water/kg of air)	0.012	0.03
HTC improvement w.r.t control (straight line)	20%	7%
HTC improvement w.r.t control (interdigitated pattern)	19%	12.7%
condensate collection rate improvement over control surface for straight-line pattern( $L m^{-2} h^{-1}$ )	17.4% (0.8135)	3.1% (1.6698)
condensate collection rate improvement over control surface for interdigitated pattern( $L m^{-2} h^{-1}$ )	18.9% (0.8212)	12.4% (1.8151)

TABLE III

SUMMARY OF CONDITIONS (CASES C1 AND C2) AND EXPERIMENTAL RESULTS (CONDENSATION HEAT TRANSFER COEFFICIENT AND CONDENSATE COLLECTION RATE) COMPARING THE PLAIN ALUMINUM, MIRROR-FINISH UNPATTERNED CONTROL CASE WITH TWO PATTERNED CONFIGURATIONS\*

$\Delta T$  values for the control case were 14.3 and 12.8 K, respectively, and the corresponding average HTC values were  $30.6 \pm 1.0$  and  $78.8 \pm 1.9 W m^{-2} K^{-1}$ . Although the  $\Delta T$  value for condition C1 was slightly higher than that for C2, the latter yielded a faster water collection rate (and HTC) as a result of a larger (by 2.5-fold) ambient vapor mass fraction (0.012 kg/kg for C1 as opposed 0.03 kg/kg for C2). For the wettability-patterned substrate, both the condensate collection and the latent heat transfer coefficient increased by  $\sim 18\%$  (over the control case) for condition C1. However, for C2, the  $\sim 3.5\%$ . This reduction in heat transfer improvement may be attributed to a greater degree of difficulty in rapidly draining the condensate under higher condensation rates (which suggests an optimization process for determining which pat-

tern works best). Figure 29 shows a comparison of droplet morphology on the patterned surface after 2 h of condensation in each of the two cases. Clearly, the droplets for C2 (Figure 29 b) appear to be larger than those observed for C1 (Figure 29 a). The zoomed-in view for C2 in Figure 29b2 indicates that several droplets even tend to deviate from a circular footprint, growing on the mirror finish stripes longitudinally between the superhydrophilic tracks. These tracks meant for draining the condensate by hemiwicking and capillary pumping were probably at their maximum condensate drainage capability for condition C2, leading to a reduction in the droplet drainage rate from the less wettable (DWC) regions. Apparently, for condition C2, several condensate droplets that grew to touch the superhydrophilic tracks exhibited only partial drainage (leaving residual droplets behind on the less-wettable strips, as shown by the red arrows in Figure 29b2) and offered reduced rejuvenation compared to that in Figure 29a2. Thus, the drainage capacity of the superhydrophilic tracks emerges as the rate-limiting factor at a high humidity ratio (and also high heat flux).

There are two important features to note in this context. The observed heat transfer improvement was realized in spite of two adverse factors: first, the presence of noncondensable gases, which raised the thermal resistance that masked off any improvement resulting from limiting the maximum droplet size(129), and second, the deployment of  $\sim 40\%$  of the substrate for the superhydrophilic tracks (where the FWC has taken place), leaving only 60% of the entire area for DWC. The patterned substrate in Figure 29 offers an  $\sim 10.7m$  long wettability transition line (across which the liquid droplets are swept away from the DWC regions) on the  $\sim 108\text{ cm}^2$  plate area. Designing these tracks to be wider could be an option to increase their

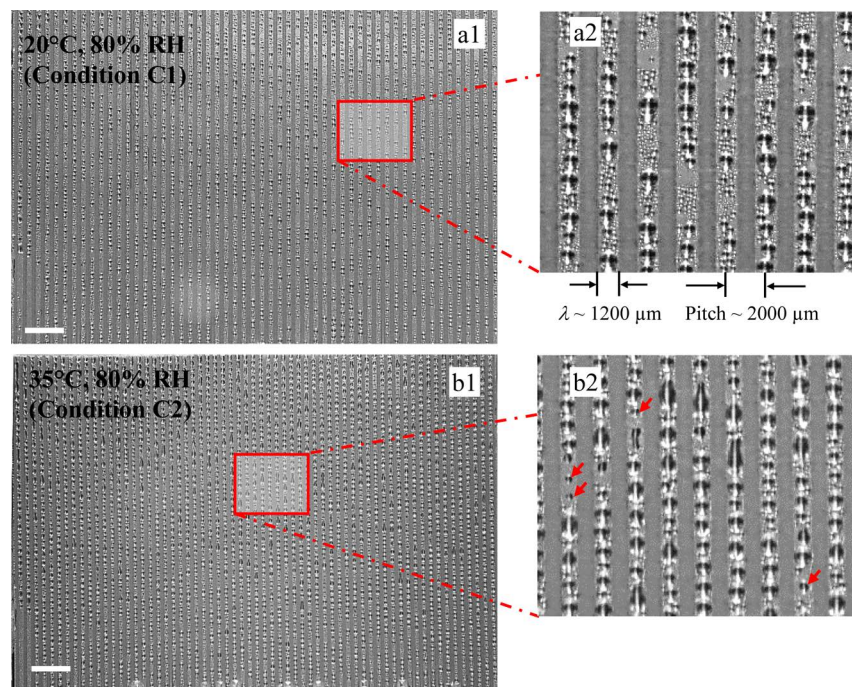


Figure 29. Substrates with straight-line wettability patterns were tested in the condensation chamber for two different conditions, namely, C1 ( $20\text{ }^{\circ}\text{C}$  DBT,  $80\% \text{ RH}$ ) (a1) and C2 ( $35\text{ }^{\circ}\text{C}$  DBT,  $80\% \text{ RH}$ ) (b1). (a2, b2) Zoomed-in images of a1 and b1, respectively. The dimensions of the simple line design are marked in a2. A greater presence of water vapor in the atmosphere for b1 is substantiated visually by observing a greater number of droplets in b2 as compared to the number of droplets in a2. Red arrows in b2 show residual droplets after incomplete capillary pumping into the adjoining drainage routes. Scale bars in a1 and b1 denote  $10\text{ mm}$ .

condensate drainage capacity, at the expense of decreasing the available area (where sustained heterogeneous nucleation and DWC take place) and the length of the wettability transition line per unit area of the substrate. The latter two effects are detrimental enough (to the overall condensation rate), so we chose not to explore the widening of the superhydrophilic tracks to buttress condensate drainage.

#### **4.3.5 Design considerations for optimal collection**

Sustaining dropwise condensation and maximizing HTC requires balancing the trade-offs between the allocated areas on the sample for sustained droplet nucleation and maximum size control and the superhydrophilic tracks intended for consistent and efficient drainage of the condensate absorbed from the adjoining DWC domains. The foregoing discussion provides evidence that controlling the maximum droplet size using hydrophilic-superhydrophilic patterns on the condenser plate surface indeed can lead to an enhancement in the condensation heat transfer rate. However, the discussion also highlights the need to ensure adequate drainage of condensate using the minimum possible area for the superhydrophilic tracks. Our prior work<sup>(15)</sup> has demonstrated that designing the superhydrophilic tracks with a small tapering angle gives them the ability to achieve rapid pumpless transport of liquid on wettability-patterned surfaces. The same design is hypothesized to work for transporting condensate away from the present condensing surfaces.

Figure 30a shows a wedge-shaped superhydrophilic track on the condensing surface transporting the collected condensate from the narrow end to the wider one (with the latter ending at an elliptic well). The fact that the superhydrophilic track facilitates FWC is actually har-

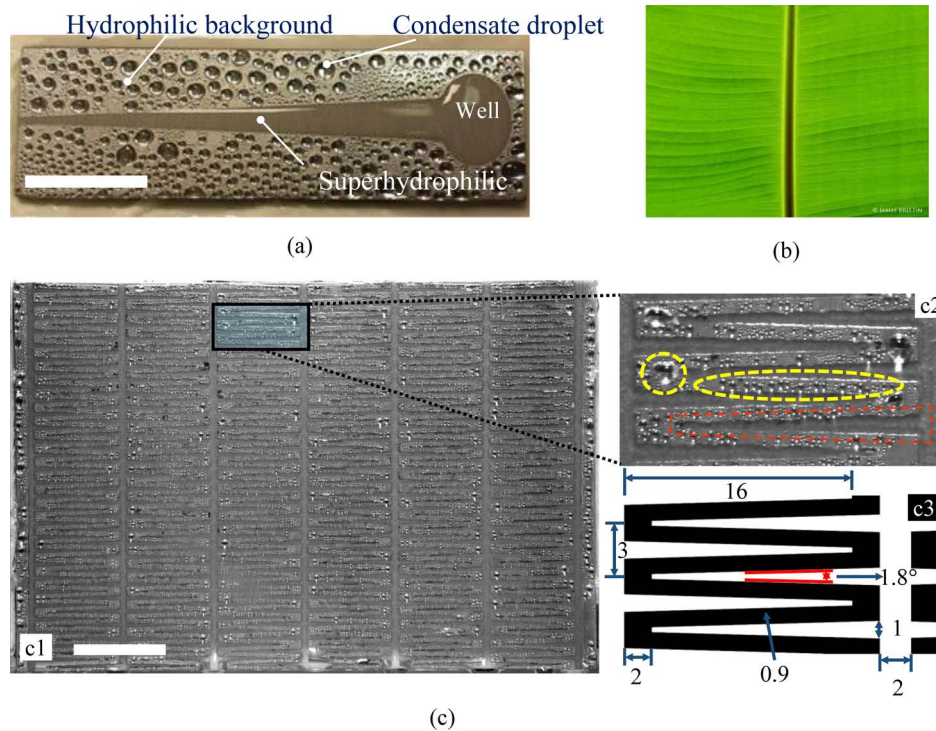


Figure 30. (a) Wedge-shaped superhydrophilic track aiding the pumpless transport of condensate from the narrow end to the wider end. The bulged puddle on the elliptic superhydrophilic well at the broad end of the wedge holds the condensate drained through this track. The area around the track is mildly hydrophilic and promotes DWC, as seen in this image. (b) Typical vein structure of a banana leaf. (c1) Condensation on an interdigitated wettability-patterned design inspired from the leaf vein network layout (image taken after 3 h of condensation under the same environmental conditions as in Figure 29a). The inset (c2) shows the condensate droplet distribution on the hydrophilic bands; one superhydrophilic tapered wedge track is highlighted in red; note the difference in droplet size in the two yellow-highlighted philic regions, which have different lateral widths. (c3) Key dimensions of the interdigitated design of the plate shown in c1. White scale bars denote 20 mm. All dimensions, except the wedge angle, in c3 are in millimeters. Image (b) was reprinted with permission from J. Brittin ([www.jamesbrittin.com](http://www.jamesbrittin.com)).

nessed in creating a liquid film curvature gradient that allows efficient capillary pumping along the tapered track. See (15) for a detailed explanation of this effect. The liquid pooled at the track end (collection well, produced by patterning an elliptic superhydrophilic region) provides evidence of condensate pumping. For a large condensing surface, the ideal design should offer a suitable network of these wedges for sustained condensate drainage. In an effort to improve the performance of the present condensing surfaces, we take inspiration from the vein arrangement of plant leaves, which presents a typical 2D network that offers an optimal liquid (sap) transport system. Considering the closest analogy to the parallel-striped wettability patterns presented in the foregoing sections, we adopt a simple leaf venation pattern that is usually found in banana leaves; see Figure 30b. To compare the condensation performance against the parallel-striped wettability-patterned plate of Figure 29, the ratio of the DWC (philic) area to the FWC (superhydrophilic) area was kept the same, i.e., 3:2. However, because of its pattern, the bioinspired design had a larger net available length of the wettability transition,  $\sim 11.9 m$  (compared to  $10.7 m$  for the parallel stripe design) for the same plate area. This offered a greater possibility of droplets being drained to the superhydrophilic tracks. To compare the efficacy of the bioinspired wettability pattern on the overall DWC, we exposed the surface to a condensing environment similar to the one for the straight-line pattern. Droplet distribution on the hydrophilic strips of the bioinspired interdigitated pattern is shown in the inset Figure 30(c2). However, in the tip region of each wedge track, where the local width of the philic region was larger, condensate droplets appeared consistently smaller than the control case (bare aluminum plate). Figure 30(c3) shows the key dimensions of the design.

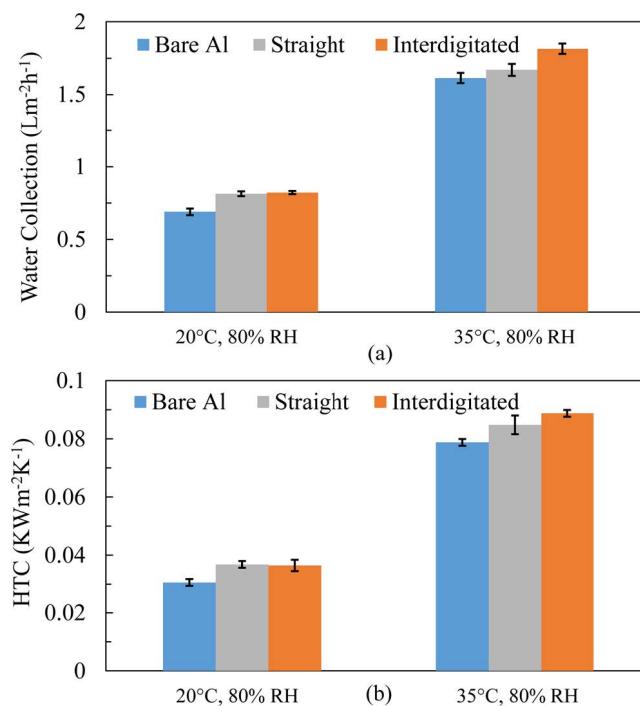


Figure 31. Bar graphs showing the relative improvement in condensation in terms of (a) condensate collection rate, and (b) latent heat transfer coefficient (HTC) for two different ambient environments for the unpatterned control case (bare Al), straight-line, and bioinspired interdigitated wettability patterns. Both patterned surfaces performed better than the control surface for 20 °C DBT 80% RH (C1) and 35 °C DBT 80% RH (C2) conditions. In the harsher situation (C2), the interdigitated pattern is more effective compared to the straight-line patterns. The improvement is solely attributed to the geometric shape of the wettability patterning of the substrate.

Figure 31 compares the condensation and heat transfer performance of the bioinspired interdigitated pattern design to those of the control case (the unpatterned mirror-finish Al plate) and the straight-line patterned substrates. Each data point in Figure 31 is obtained from at least five 2-5 h runs; the error bars denote the standard deviation. The interdigitated pattern demonstrated an overall  $\sim 19\%$  improvement in the condensate collection rate and an  $\sim 20\%$  improvement in HTC compared to the control case for  $20\text{ }^{\circ}\text{C}$  DBT  $80\%$  RH. This performance was comparable to the straight-line pattern case. However, for the  $35\text{ }^{\circ}\text{C}$  DBT  $80\%$  RH condition, the bioinspired interdigitated pattern showed an  $\sim 12.5\%$  improvement in water collection and HTC over the base case. This translated to an extra  $\sim 9\%$  improvement in water collection and  $5\%$  improvement in HTC by using the bioinspired interdigitated patterns instead of the straight-line patterns. Therefore, the bioinspired design would be preferable under more adverse condensing conditions (higher humidity ratio and heat flux), where other types of wettability patterns (or unpatterned substrates) would lower the DWC performance as a result of inadequate condensate drainage and larger departing droplet sizes.

## CHAPTER 5

### PARAMETRIC STUDY OF ENHANCED DROPWISE CONDENSATION ON WETTABILITY-PATTERNED SURFACES

Previously published as *Mahapatra, Pallab Sinha, Aritra Ghosh, Ranjan Ganguly, and Constantine M. Megaridis. "Key design and operating parameters for enhancing dropwise condensation through wettability patterning." International Journal of Heat and Mass Transfer 92 (2016): 877-883.*

#### **5.1 Introduction**

Condensation of vapor has critical engineering importance due to its widespread applications in numerous industrial processes, such as water harvesting(141), dehumidification(142), HVAC(143), power generation(144), chemical production, water desalination(145). Upon rejecting the latent heat to the subcooled condenser surface, the vapor phase condenses around thermodynamically favored nucleation sites on the surface, in turn forming condensate droplets (dropwise condensation, DWC). The nucleation density is higher for surfaces that are more wettable (i.e. hydrophilic), or exposed to higher vapor mass concentrations, or subject to larger subcooling(146). The DWC mode prevails on a pristine metal (e.g., Al or Cu) surface at low heat flux, or during the initial stages of condensation. However, for most engineering applications, particularly at high heat flux, the condensate droplets eventually coalesce and end up forming a continuous film on the surface, leading to filmwise condensation (FWC). Higher nu-

cleation density exacerbates the transition from DWC to FWC, making a wettable surface more vulnerable to FWC. Between the two modes of condensation, DWC typically exhibits an order of magnitude higher heat transfer coefficient (HTC)(94; 124; 146; 147) than the FWC mode at similar operating conditions. This happens primarily because much of the condensing surface that is covered with the liquid film cannot offer new heterogeneous nucleation sites; moreover, the liquid film poses a considerable thermal resistance(148). Heat transfer rates in both filmwise and dropwise mode decrease substantially in the presence of non-condensable gases (NCG)(149). Water condenses from the humid air when the surface temperature is maintained below the dew-point temperature (i.e. saturation temperature corresponding to the vapor partial pressure). In an idealized DWC scenario, droplets grow around a nucleation site until they are shed by gravity, exposing pristine surface for fresh nucleation (this process is called surface rejuvenation). It has been shown(52) that superhydrophilic tracks can be used to transport the liquid rapidly from the dropwise condensing surfaces. Due to widespread application in the industry, several attempts have been made by researchers over the last eight decades to enhance DWC heat transfer and abate or delay the onset of FWC(94; 150; 151; 152; 153).

The wettability of the condensing surface plays a critical role in DWC(154). Recent advances (154; 96; 108; 155) in surface science have renewed research interest in tuning the surface wettability to promote and sustain DWC. Superhydrophobic surfaces have been a popular choice in this regard, since the high droplet mobility (i.e. low contact angle hysteresis) on these surfaces favors gravity-induced shedding of condensate. Shedding a condensate droplet at a smaller size is advantageous for DWC, since droplet improving the HTC(153; 108; 138; 104; 93; 137). Using

theoretical arguments, Dietz *et al.*(156) proposed that a vertically-oriented superhydrophobic surface should yield about a 100% increase in the DWC heat transfer coefficient compared to a vertically-oriented non-textured hydrophobic surface. Superhydrophobic surfaces under low subcooling can even induce self-propelled jumping droplets, which in turn aid the removal of condensate formed on such low-energy surfaces(105). However this phenomenon is not observed at higher surface subcooling(102). In a pure-steam environment, Miljkovic *et al.*(104) showed a 30% enhancement by using coalescence-induced droplet jumping on a superhydrophobic copper surface.

Although superhydrophobic surfaces score better in DWC than surfaces with higher wettability (e.g., hydrophobic, hydrophilic or superhydrophilic), their performance is not ubiquitously superior. For instance, superhydrophobic surfaces have a higher thermodynamic barrier to nucleation compared to more wettable surfaces, a factor that may lead to poor condensation rates(93; 137). Thus, DWC heat transfer performance of superhydrophobic surfaces can in fact be lower than hydrophobic surfaces(157). Different types of surfaces have been proposed to overcome this issue, such as hydrophilic-hydrophobic patterned surfaces(101; 158), hybrid surfaces(108; 97; 159), wettability gradient surfaces(103), grooved surfaces(160), etc. Hou *et al.*(159) developed a flat, SiO<sub>2</sub> hybrid surface with high wettability contrast that showed  $\sim 63\%$  enhancement in HTC as compared to a flat hydrophobic surface both in all-vapor and NCG environments. Zhu *et al.*(161) demonstrated that DWC HTC on a copper surface can be enhanced by  $\sim 125\%$ , as compared to the flat surface with identical chemical composition, by using ribbed nano needles at ambient temperature  $\sim 22^\circ C$  and relative humidity (RH)  $\sim 80\%$ .

Other studies(162; 163) have also found that the surfaces of some plants and animals(164) are able to harvest water from the atmosphere. Several attempts have been made to mimic the mechanisms observed in nature(114). Leaf vein structures were used earlier(52) to show the effective transport of liquid droplets. Hydrophilic-hydrophobic patterned surfaces were used for fast droplet drainage by manipulating their size distribution, which eventually enhanced the heat transfer. Chatterjee *et al.*(165) used a hydrophilic pattern on a superhydrophobic background and observed  $\sim 7.6\%$  enhancement in heat transfer over the base case of a homogeneous superhydrophobic surface. Ghosh *et al.*(52) used bio-inspired wettability-patterned superhydrophilic tracks on a hydrophilic surface to promote capillary-driven condensate drainage and enhanced DWC heat transfer by reducing the departing droplet size on the hydrophilic regions of the condenser plate. They demonstrated a 19% performance improvement for the patterned surface in comparison to the all-DWC surface in a vapor-NCG environment. Although Ghosh *et al.*(52) demonstrated HTC improvement and attributed this to the reduced drop size, their study did not examine the relative influence of dedicating part of the condenser surface to the FWC mode (the tracks). Therefore, the actual source of DWC improvement was not clear. In this follow-up study, we decipher the relative role of the competing effects by altering the FWC and DWC area ratios in different wettability patterns. Peng *et al.*(158) achieved a 23% improvement in the condensate collection rate compared to DWC using vertically striped patterns in a steam environment.

Due to its moderately high equilibrium contact angle ( $\sim 78^\circ$ ) and low contact angle hysteresis(52), a mirror finished aluminum alloy surface exhibits dropwise condensation. These surfaces

are known for their reproducibility and stability(123). On the other hand, a superhydrophilic surface offers much higher nucleation density and has a tendency to form a film, which can be used for liquid drainage. The extent to which each factor contributes depends on the % – *age* of NCG in the ambient and the degree of surface subcooling. Therefore, in order to design an efficient wettability-patterned surface, one needs to clearly identify the relative influences of these promoting and retarding factors. The objective of the present work is to optimize the area allocations for DWC and FWC on a wettability-patterned substrate for enhancing the overall condensation performance in an NCG environment. Heat transfer enhancement is assessed by comparing the HTC's on the wettability-patterned surfaces with a mirror-finish (control) surface that did not undergo any surface treatment. The experiments are performed at two representative humidity ratios (HR). The optimal design has been reached by modifying the earlier design(52) of bio-inspired wettability-confined superhydrophilic tracks on a hydrophilic background, and properly controlling the maximum droplet size by changing the fractional area of superhydrophilic tracks to facilitate rapid condensate drainage. The mirror-finish aluminum is used for DWC, while the FWC zone is created by superhydrophilizing the metal surface. The present method has the additional advantage that the sample preparation process is facile, scalable and does not require a clean room environment.

## **5.2 Experimental procedure**

We used a mirror-finish aluminum plate (multipurpose polished aluminum alloy 6061, 2 mm thick, McMaster Carr) which is provided by the manufacturer with a protective (removable) polymer sheet adhered to the metal with a mild adhesive. CO<sub>2</sub> laser beam irradiation was

employed to draw patterns on the polymer coating, which was then selectively peeled to expose the underlying mirror-finish aluminum surface to chemical etching by hydrochloric acid (Sigma Aldrich, 37% in 3 *M* aqueous solution). The acid corroded the exposed regions of mirror-finish aluminum, thus creating the superhydrophilic domains (sessile contact angle close to  $0^\circ$  for water). The sample was then passivated for 30 *min* in boiling water to impart durability to the superhydrophilic domains. Finally, the remaining protective coating was peeled off, exposing the mirror-finish background of the patterned superhydrophilic tracks. The mirror-finish aluminum is slightly hydrophilic with sessile contact angle  $\sim 78.2 \pm 2^\circ$  for water. The detailed sample preparation procedure is described chapter 4. In addition, an all-superhydrophobic control surface was prepared by immersing the etched (superhydrophilic) aluminum plate in a 2 *wt.%* solution of 1H, 1H, 2H, 2H-Perfluorodecyltriethoxysilane (Sigma Aldrich, 97%) in ethanol (Decon labs, 200 proof) for 1 h. The samples were left overnight to dry, resulting in a superhydrophobic Al surface with sessile water contact angle  $161.2^\circ \pm 2^\circ$ .

The wettability-patterned condensing surfaces were tested in an environmental chamber (ESPEQ, *SH* – 641) at two different conditions of dry bulb temperature (DBT) and RH. Thermally conductive adhesive tapes (McMaster Carr, 6838A11) were used to mount each sample vertically on a Peltier cooler (TeTech, *CP* – 061). Four K-type thermocouples (bead diameter 0.13 *mm*, Omega) were inserted into 800  $\mu\text{m}$  diameter holes, drilled in the plate beneath the condensing surface. The temperature was recorded with a data acquisition system (Omega, USB 2400 series) with a sampling frequency of 1 Hz. Condensate that drained from the lower edge of a vertical plate was collected for over 24 h, and weighed in a digital micro-

balance with an accuracy of 0.01  $g$ . Every experiment was conducted several times to obtain a data point at each parametric condition (condenser surface design, or condensing environment parameter).

### 5.3 Results and discussion

#### 5.3.1 Pattern design for enhanced condensate transport

In chapter 4, the description of the bio-inspired interdigitated pattern was provided in detail. It was shown that the interdigitated patterns performed better than the straight line patterns in terms of both condensation rate and HTC. Properly designing the dropwise condensing hydrophilic and filmwise condensing superhydrophilic zones achieved the improvement of heat transfer coefficient. Figure 32a shows the design of the interdigitated pattern used in our earlier work(52)(base case), while an improved staggered pattern of the superhydrophilic tracks is shown in Figure 32b.

In the base case (Figure 32a), the superhydrophilic wedge-shaped tracks are laid *in line* on either side of the central vein. The tapered track drives spontaneous capillary pumping from narrow to wide portions of the wedge due to the liquid film curvature gradient created on the superhydrophilic domains(15). As the wedge-tracks lay directly opposite to each other about the central vein, the momentum of condensate pumped by each wedge track forces the liquid onto the opposing wedge track, thus causing viscous losses, and in turn reducing the efficiency of the drainage process. This mechanism not only impedes the drainage in the second track, but also increases the transport time of the condensate from the first wedge-track into the central vein. To overcome this problem and facilitate condensate drainage from the wedge

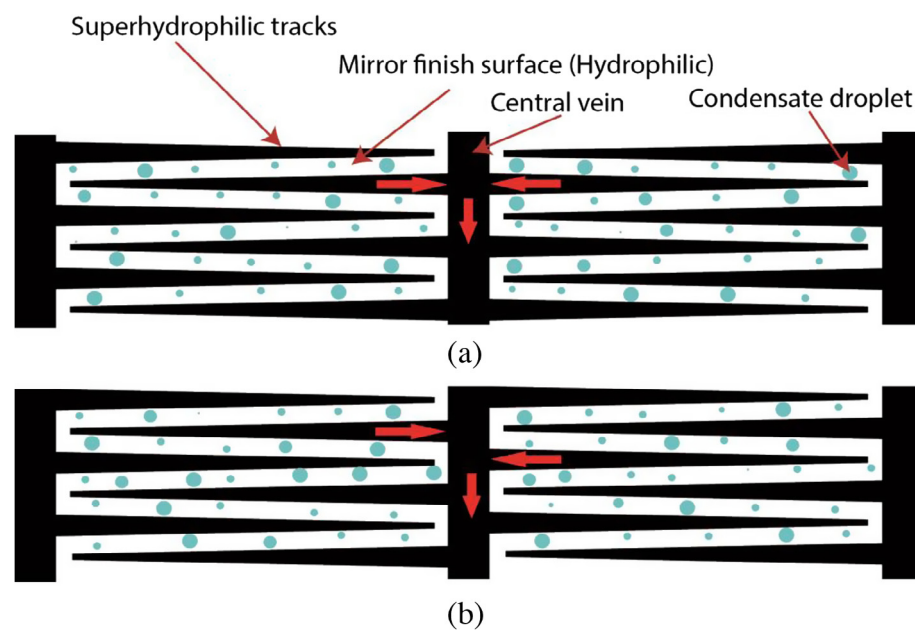


Figure 32. Two designs of periodically-patterned samples for condensation experiments. (a) Interdigitated design where the superhydrophilic tracks are arranged in-line on either side of the central drainage vein (base case), and (b) staggered design of the tracks. The latter facilitates more efficient drainage of the lateral wedge tracks into the vertical drainage vein.

tracks on either side of the central vein, the revised design places the wedges in a staggered fashion, as shown in Figure 32b. While both the base case (Figure 32a) and the new staggered design (Figure 32b) have the same FWC area ratio of 46.4% of the overall plate, the heat transfer enhancement is 12.1% and 15.9%, respectively, as compared to the control (mirror-finish) surface in a condensing environment of 20 °C (DBT) and RH of 80%.

It is important to note that a patterned surface requires a certain percentage of condensing area for laying the superhydrophilic drainage tracks, where a liquid film of the draining condensate prevails. On one hand, the superhydrophilic tracks limit the largest departing droplet size on the mirror-finish areas, thereby promoting DWC heat transfer(52). On the other hand, the liquid film covering these drainage tracks offers poor FWC HTC. To determine the effects of these two conflicting mechanisms, condensation experiments are also performed on an unpatterned condensing surface that contains monolithic DWC and FWC spatial domains, with area fractions representing both designs shown in Figure 32. One portion of the unpatterned surface consists of the mirror-finish aluminum (DWC domain), with the rest having been etched superhydrophilic; see vertical band on right side of Figure 33a.

Condensation of water droplets on the unpatterned and patterned surfaces for different area ratios of DWC and FWC domains were studied next in order to identify the design best suited for optimal performance. Droplets form on the mirror-finish surface, as the plate temperature is brought below the corresponding dew point temperature. These droplets grow upon sustained condensation and coalescence. For the interdigitated wettability-patterned surfaces, the growing condensate droplets eventually touch the boundaries of the superhydrophilic wedge-tracks,

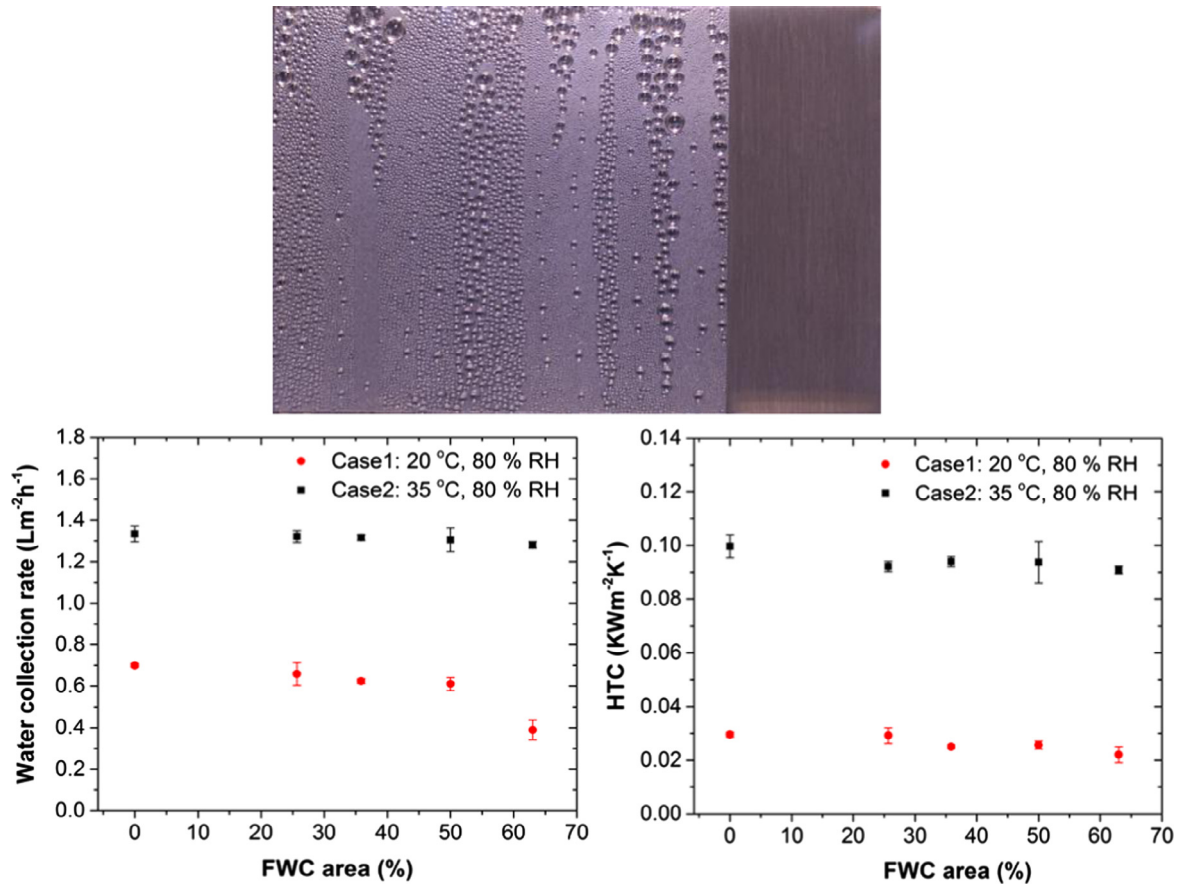


Figure 33. (a) Example of an unpatterned condensing surface with 75% dropwise area (left) and 25% filmwise area (right). The scale bar (in white) denotes 10 *mm*. Variation of (b) water condensate collection rate, and (c) HTC with FWC area fraction (expressed as percentage of the total condensing surface). As FWC area ratio decreases, the corresponding DWC area ratio increases, thus enhancing heat transfer coefficient as well as water collection rates.

where they are drained. The superhydrophilic wedge tracks transport the liquid through hemiwicking (due to the underlying surface texture) as well as capillary pumping (due to Laplace pressure gradient from the narrow to the wide end of the wedge). The mechanism of this rapid pumpless transport is explained elsewhere(15). For the unpatterned surface containing distinct DWC and FWC domains, the droplets grow large enough until they are shed by gravity. Thermal resistance to the dropwise condensation is largely dependent on the maximum droplet radius. The theoretical upper limit of the maximum droplet radius in a mirror-finish vertical plate is of the order of the capillary length scale (less than  $2.7\text{ mm}$  for water). For the patterned surfaces, on the other hand, the maximum droplet radius depends on the interspacing (width of the DWC strip) between the adjacent wedge tracks.

All the experiments have been performed at two different environmental conditions: Case 1 (**C1**): DBT of  $20\text{ }^{\circ}\text{C}$  and RH of 80%, Case 2 (**C2**): DBT of  $35\text{ }^{\circ}\text{C}$  and RH of 80%. The overall heat transfer during condensation in the presence of non-condensable gases has sensible and latent heat components. The latent heat part of the HTC can be calculated from the measured condensation rate by Equation 2.3, as caused by the difference between the dew-point temperature ( $T_{dew}$ ) and substrate temperature ( $T_s$ ). The sensible part (driven by the difference between the ambient DBT ( $T_1$ ) and  $T_s$ ) of the overall heat transfer coefficient remains more or less the same for all the unpatterned and patterned surfaces. Therefore, the sensible component of the overall heat transfer coefficient is not considered in the present calculations. The experimental conditions and the measured performance of each surface are summarized in Table IV.

	C1	C2
dry bulb temperature ( $^{\circ}C$ )	20	35
relative humidity (%)	80	80
$T_{dew}$ ( $^{\circ}C$ )	16.5	31
plate temp, $T_s$ ( $^{\circ}C$ )	$2.3 \pm 0.5$	$22.4 \pm 0.3$
$\Delta T = T_{dew} - T_s$ ( $^{\circ}C$ )	14.2	8.6
$T_{\infty} - T_s$ ( $^{\circ}C$ )	17.7	12.6
Humidity ratio(kg of water/kg of air)	0.012	0.03
HTC improvement w.r.t control surface (straight line pattern)	20%	7%
HTC improvement w.r.t control surface (interdigitated pattern)	19%	12.7%
Enhancement over mirror finish aluminum:		
Condensate collection rate	$\sim 30\%$	$\sim 15\%$
HTC	$\sim 34\%$	$\sim 18\%$
Enhancement over superhydrophilic aluminum:		
Condensate collection rate	$\sim 55\%$	$\sim 21\%$
HTC	$\sim 23\%$	$\sim 26\%$
Enhancement over superhydrophobic aluminum:		
Condensate collection rate	$\sim 95\%$	$\sim 60\%$
HTC	$\sim 75\%$	$\sim 76\%$

TABLE IV

SUMMARY OF CONDITIONS (CASES C1 AND C2) AND COMPARISONS OF CONDENSATION HTC AND CONDENSATE COLLECTION RATE ON THE PATTERNED SURFACES AGAINST THE CONTROL CASES OF MIRRORFINISHED ALUMINUM (DWC ONLY), SUPERHYDROPHILIC SURFACE (FWC ONLY), AND SUPERHYDROPHOBIC SURFACE (DWC ONLY).

### 5.3.2 Effect of FWC fractional area ratio

As is evident from the previous discussion, the heat transfer as well as the water collection rate would depend on the respective areas occupied by the DWC and FWC zones. Figure 33 shows the effect of FWC area on the heat transfer and condensation performance on the unpatterned surfaces. More specifically, Figure 33a shows a photograph of the dropwise and filmwise condensing areas. During dropwise condensation, droplets of different sizes are present on the condensing surface ranging from barely visible sizes to  $\sim 1 \text{ mm}$ . During condensation, due to cyclic nucleation, growth and coalescence, shedding (for unpatterned surface) or draining (for patterned surface) of droplets, polydispersity in the droplet size is evident. The droplet size distribution for a finite size of the surface is reported to be time invariant(100). The minimum ( $r_{min}$ ) and maximum ( $r_{max}$ ) droplet sizes on the surface are dependent on the temperature difference driving the condensation process, surface tension ( $\sigma$ ), density of water ( $\rho_w$ ), latent heat ( $h_{fg}$ ), tilt angle of the surface ( $\alpha$ ), as well as the contact angles ( $\theta$ ). they are given by the following equations.

$$r_{min} = \frac{2T_{sat}\sigma}{h_{fg}\rho_w(T_{dew} - T_s)} \quad (5.1)$$

$$r_{max} = \left[ \frac{3\sigma}{\rho_w g \sin \alpha} \frac{(\cos \theta_r - \cos \theta_a) \sin \theta}{(2 - 3 \cos \theta + \cos^3 \theta)} \right]^{1/2} \quad (5.2)$$

For the mirror-finish aluminum surface (DWC), from Equation 5.2 the theoretical maximum droplet radius is  $\sim 3 \text{ mm}$ , while the experimentally measured maximum came up to  $\sim 1.6 \text{ mm}$ . Figure 33a shows a typical unpatterned surface that exhibits DWC (left, mirror-finish) and FWC

(right, superhydrophilic) domains side-by-side. Figure 33b and c show the water collection rate and heat transfer coefficient, respectively, for different FWC area percentages. The 0% FWC case in Figure 33b and c corresponds to DWC on the mirror-finish surface (control surface), while the higher FWC area cases indicate that a larger fraction of the condenser plate has been appropriated for droplet collection and drainage. In Figure 33b and c, each result is obtained from five 2 – 4 *h* of runs and the error bars denote the standard deviation from the mean value. The full mirror-finish surface (0% *FWC*) demonstrates maximum heat transfer coefficient and water collection rate, as the condensation mode is completely dropwise. At higher FWC area, condensate collection and HTC decrease due to the increased contribution of filmwise condensation. As seen in Figure 33b and c, the water collection rates and HTC values decrease by 44.3 and 25.2% respectively, as the FWC area percentage is increased from zero to 63% for Case 1. At higher humidity content (Case 2) the water collection and HTC figures decrease only by 4 and 8.9% respectively, as the FWC area percentage is increased from zero to 63%. It must be noted that the water collection rates are much lower for the all-superhydrophobic surface as compared to the mirror-finish sample. Despite fostering DWC with smaller departing droplet diameter, the superhydrophobic surface offers a large surface energy barrier to nucleation, eventually impeding the water collection. For the all-superhydrophobic surface in Case 1, water collection rate was  $0.46 \text{ L m}^{-2} \text{ h}^{-1}$  and HTC was  $0.02 \text{ KW m}^{-2} \text{ K}^{-1}$ , whereas, for Case 2 the corresponding values were  $0.96 \text{ L m}^{-2} \text{ h}^{-1}$  and  $0.06 \text{ KW m}^{-2} \text{ K}^{-1}$ , respectively.

Having identified the relative influence of rendering a given fraction of unpatterned condenser surface superhydrophilic (i.e., replacing the corresponding DWC area fraction), we now investigate the same on a surface with interdigitated patterns. HTC and water collection rates for the patterned surfaces in different DWC area percentages are plotted in Figure 34. Here we changed the number of wedges and altered the interspacing between two consecutive wedges to vary the intervening DWC area. In Figure 34a, a typical staggered wedge-shaped pattern is shown. From Figure 34b and c it is apparent that the condensation heat transfer performance increases with the FWC area fraction at low value, attains a maximum at an intermediate FWC area fraction, and finally decreases with further rise in FWC area percentage. For both Cases 1 and 2, distinct optimum superhydrophilic area fractions exist that mark the simultaneous maxima in water collection rate and HTC. For a substrate with very small FWC area percentage, the widths of intervening mirror-finish strips are larger. Therefore, DWC occurring on the mirror-finish part produces larger departing droplet size(52). At higher FWC area fraction, the width of the hydrophilic strips (and hence the departing droplet diameter) is smaller, but the dropwise condensing area also becomes relatively smaller. Thus, condensation is dominated by the filmwise mode. Both these factors combine to decrease condensation performance on either side of the optimum FWC area fractions.

The spacing between the two wedge-shaped tracks at 46.4% of FWC area is 0.87 *mm* whereas, at 25.7%, the spacing is 2.85 *mm*. For Case 1 ( $DBT = 20\text{ }^{\circ}C$ ,  $RH = 80\%$ ) the enhancement of HTC and water collection rate become maximum for FWC fractional area of 29.9%. For the higher vapor content Case 2 ( $DBT = 35\text{ }^{\circ}C$ ,  $RH = 80\%$ ) both maxima HTC

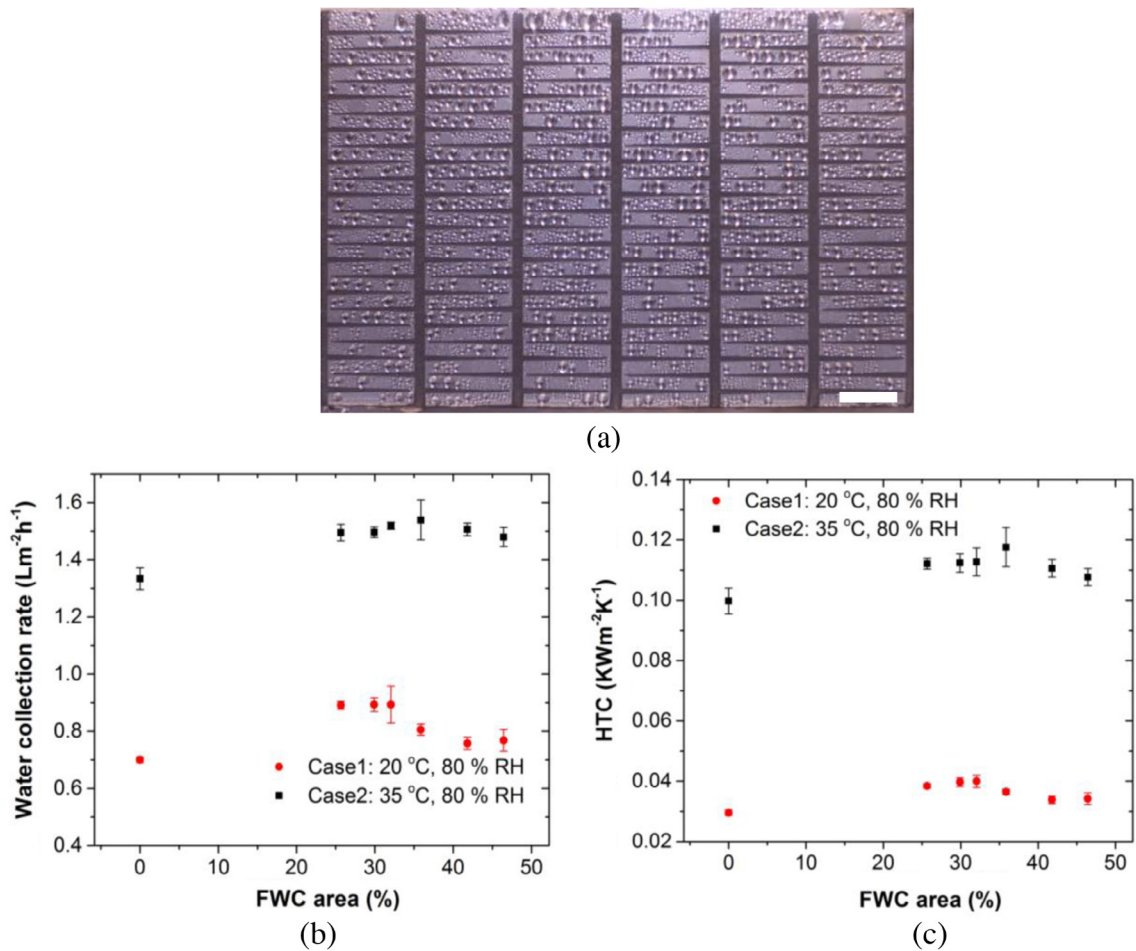


Figure 34. Enhancement in (a) water collection rate, and (b) HTC for different FWC fractional areas under two distinct environmental conditions (Cases 1 and 2). For Case 1, the maximum enhancement in HTC is observed for FWC area of 29.9%. The maximum enhancement in HTC is  $\sim 34.4\%$  and  $\sim 30.5\%$  in water collection rate. For Case 2 (higher vapor content), the maximum enhancements in HTC (18%) and in water collection (15.4%) were observed for FWC fractional area of 35.9%.

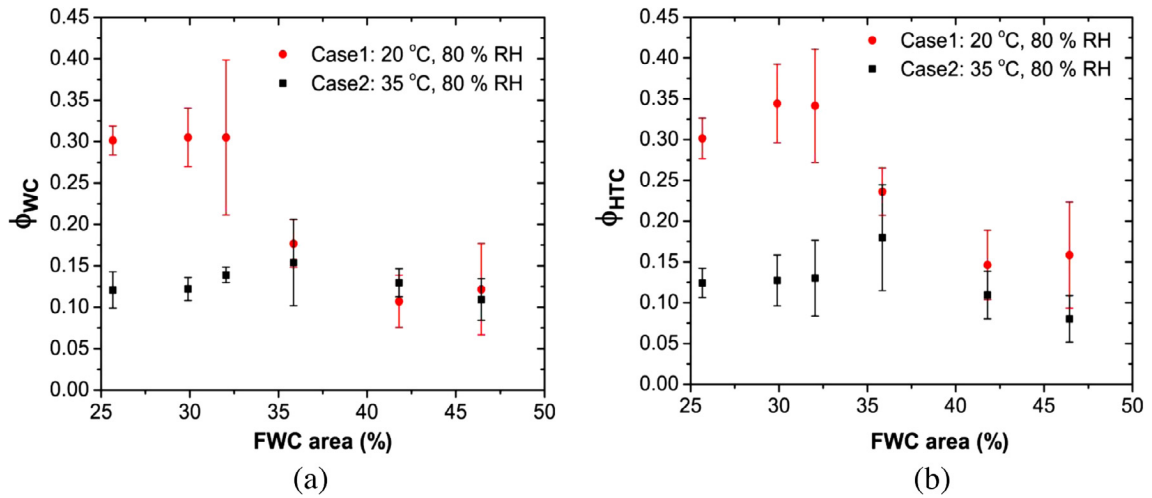


Figure 35. Enhancement in (a) water collection rate, and (b) HTC for different FWC fractional areas under two distinct environmental conditions (Cases 1 and 2). For Case 1, the maximum enhancement in HTC is observed for FWC area of 29.9%. The maximum enhancement in HTC is  $\sim 34.4\%$  and  $\sim 30.5\%$  in water collection rate. For Case 2 (higher vapor content), the maximum enhancements in HTC ( $\sim 18\%$ ) and in water collection ( $\sim 15.4\%$ ) were observed for FWC fractional area of 35.9%.

and water collection rate are higher than in Case 1, with the highest water collection rate and HTC found at FWC area fraction of 35.9%.

Sustained dropwise condensation combined with efficient removal of the liquid condensate from the DWC zone requires a tradeoff between the FWC and DWC area fractions. The present design of the staggered arrangement of the tracks provides a long wettability transition line that facilitates sweeping of liquid by way of the superhydrophilic tracks. Figure 35 compares the

enhancement factor ( $\phi$ ) at different FWC fractional areas. This factor is defined with respect to the all-DWC (control) case, i.e.

$$\phi = \frac{I_{pattern} - I_{control}}{I_{control}} \quad (5.3)$$

In Equation 5.3,  $I$  denotes either the water collection (WC) rate or heat transfer coefficient (HTC). For Case 1, the patterned surfaces with 29.9% of FWC area demonstrate maximum enhancements of  $\sim 34.4\%$  in HTC and 30.5% in water collection. At the highest FWC area (46.4%) considered in the present work for the patterned surfaces, the improvements in HTC and water collection are 15.9% and 12.2%, respectively. For Case 2, the maximum enhancement in HTC is observed for FWC fractional area of 35.9%. The maximum enhancement in HTC is 18% and 15.4% in water collection. It is important to note that the enhancement factor depends on the respective control surface. Thus, when compared against the all-superhydrophobic surface, Case 1 has enhancements of 95.1% and 75.8%, for DWC rate and HTC, respectively. For Case 2, the corresponding enhancements are 60.3% and 76.9%, respectively. These improvements also depend on the environmental conditions and design of the patterned surfaces; the latter determines the shedding droplet diameter as well as the efficient droplet transport through the hydrophilic tracks. At higher condensation rates, as in Case 2, the maximum heat transfer enhancement is observed at a higher FWC area percentage as compared to Case 1. This happens because the increased condensate volume flow rate warrants more superhydrophilic (FWC) track area for transporting the liquid. The results clearly indicate that the design of

optimized wettability patterns for enhancing heat transfer performance varies with the operating conditions.

## CHAPTER 6

### CONCLUSIONS AND RESEARCH OUTLOOK

#### 6.1 Shape of liquid on wettability-patterned tracks

The shape of a liquid volume on a wettability-patterned track is studied experimentally and a semi analytical model is developed to explain the counter-intuitive shape transition of the liquid with increasing volume on a rectangular track. The liquid tends to minimize its net interfacial surface energy and stabilizes with a shape (cylindrical or cylindrical plus bulge) that corresponds to the minimum liquid-gas interfacial surface area. The experimental observations are corroborated by the semi-analytical calculations. An important conclusion drawn from the data is that the liquid shift morphology when the volume deposited on the track of certain width ( $\delta$ ) corresponds to the maximum Laplace pressure, i.e. the height of the liquid at every  $x$  is half the track width  $\sim \delta$ . That particular volume is denoted as the critical volume of bulge formation, where  $V_{cr} \sim \frac{\pi\delta^2L}{8}$ . Formation of bulge (transformation from Configuration 1 to Configuration 2; see Figure 5) is delayed (higher  $V_{tot}$  is required) for increasing track width. The residual height of the liquid deposited on the track for different  $\delta$  collapse on a single curve when normalized by  $V_{cr}$ . Knowledge of  $V_{cr}$  with respect to track geometry sets a basis of design for wettability patterns and fulfills specific liquid volume requirements in an application or a device. The understanding of the liquid behavior on wettability-patterned tracks from this chapter 2 is important in figuring out the next leg of the work as described in Chapter 3, where

a diverging track ( $\delta$  varying with  $x$ ) is used to transport the liquid from one end to the other, unlike the rectangular tracks where the droplet remains stationary. The diverging track further forms the basis of rapid pumpless transport as explained in subsequent chapters.

## 6.2 Rapid pumpless transport

We developed a facile, substrate-independent, wettability patterning method and demonstrated controlled transport of liquid at large volume flow rates ( $\sim 350 \mu L s^{-1}$ ) on flat and inclined substrates. Wedge-shaped superhydrophilic planar tracks laid on a superhydrophobic background were used as the building blocks of the designs. Liquid dispensed at the narrow ends of a superhydrophilic wedge track gets transported to the wider ends by hemiwicking and Laplace pressure-driven flows. The driving capillary force increases linearly with the wedge angle of the tracks. However, the travel distance diminishes with the wedge angle. Thus, balancing the rapid transport rate and distance presents an optimization problem. The motion of liquid on the wedge track, in the form of a wetting front followed by an advancing liquid bulge, was found to surpass the classical Washburn type, yielding velocities exceeding  $400 mm s^{-1}$ . The liquid transport speed increased on prewetted tracks. More complex manipulations involving liquid metering, merging and dispensing were achieved by patterning two closely spaced parallel wedge tracks in tandem with another similar track of larger wedge angle. A juxtaposed pair of liquid bulges accumulated at the ends of two parallel dispensing tracks coalesced once a specific volume of liquid was accumulated, and the merged droplet was transported downstream through the third track spontaneously by capillary action, eventually detaching the liquid from the original dispensing tracks. The events of droplet bridging, pumping and de-bridging are

highly periodic and precise in terms of the dispensed droplet volumes. The design is capable of pumping liquid volumes ranging from 1  $\mu L$  (5-split design) to over 500  $\mu L$  (through repeated disposal of smaller liquid droplets, avoiding any back-flow). Both the single-wedge and the droplet-bridging designs demonstrated the additional capability of moving liquid up along inclined substrates without any external power input, thus providing a means of transport in 3-D microfluidic systems. A radially outward array of wedge tracks was also designed to create a droplet splitting arrangement. Droplets carefully deposited on a central philic spot were quickly and equally split amongst the tracks that transported the liquid outward with minimal cross-contamination between the split volumes. For a three-split design, a pumping rate of  $\sim 150 \mu L s^{-1}$  was recorded. The surface functionalization methods and track designs were found to work equally well on metal, paper and polymer film substrates. The concept can be implemented for pumpless liquid transport in a variety of engineering applications ranging from paper-based microfluidic devices to 3-D microfluidics or for condensate management in fuel cells.

### **6.3 Pumpless transport augmenting dropwise condensation**

We have developed and demonstrated a strategy to spatially control condensate nucleation and maximum droplet size, and facilitate pumpless liquid drainage in DWC using various wettability patterning designs on the condensing surface to ultimately harness benefits for the condensate collection rate and latent heat transfer coefficient. A facile method employing selective chemical etching and metal passivation has been shown to achieve the desired wettability contrast patterns, although the concept is not restricted only to this patterning method. The

space and time-averaged maximum droplet size were shown to scale linearly with the width of the less wettable strips on the substrate and was considerably smaller than this width. Under higher-humidity conditions, wedge-shaped superhydrophilic tracks, laid in an interdigitated pattern inspired by the vein network of banana leaves, were used to carry away the condensate pumplessly. An overall improvement in condensate collection (up to 19% compared to the control case of bare aluminum) was achieved by using the bioinspired wettability pattern design. The observed effect of wettability patterning is particularly significant in light of two factors: (i) the improvement was observed even after deploying  $\sim 40\%$  surface area of the plate sample for the superhydrophilic tracks (which do not play much of a role in DWC because the condensate forms a liquid film there), and (ii) the actual improvement (in minimizing the condensate liquid thermal resistance to DWC by reducing the maximum droplet size) was heavily masked by the presence of noncondensable gases (NCG).

#### **6.4 Parametric study of enhanced dropwise condensation on wettability-patterned surfaces**

We have demonstrated a facile and scalable wettability-patterning approach to promote condensate removal on a vertical metal plate during condensation in a controlled vapor environment also containing non-condensable gases (air). The approach does not apply any coatings on the metal condenser plate, thus circumventing the adverse effects of added thermal resistance. The experiments were performed at two representative dry bulb temperatures and relative humidity, viz. 20 °C DBT and 80% RH (Case 1) and 35 °C DBT and 80% RH (Case 2). Spatially-distributed wettability domains (hydrophilic, superhydrophilic) on metal were de-

ployed to promote dropwise condensation on the former, and rapid condensate removal on the latter, thus enhancing overall condensation heat transfer over the entire patterned surface. A staggered arrangement of tapered superhydrophilic wedges, offering long wettability transition lines and capillary-driven condensate drainage helps in rapid removal of the condensate from the metal substrate. For Case 1, the 29.9% fractional area (FWC to total surface) design resulted in a maximum enhancement of 34.4% in HTC and 30.5% in water collection rate, as compared to a mirror finish surface (all-DWC). For Case 2, the maximum enhancement figures were 18% in HTC and 15.4% in water collection rate, when the FWC area occupied 35.9% of the plate. The optimum area ratio shifted towards higher FWC fractions with rising vapor mass content in the atmosphere. The maximum figures of enhancement in water collection rates and HTC by the patterned surface for Case 1 were 95.1% and 75.8%, respectively, when compared against all-superhydrophobic control surfaces exposed to identical ambient conditions. For Case 2, these enhancements were 60.3% for WC rates and 76.9% for HTC. We have shown that these patterned surfaces offer significant improvement in condensation performance in comparison to other state of the art condensing surfaces in an NCG environment.

#### **6.4.1 Research outlook**

Exploration of pumpless surface microfluidics has been initiated in the recent years. Although this domain offers significant promise in novel  $\mu$ -volume liquid manipulation techniques, as with any newly-introduced technology, there remain several challenges that need to be mitigated. A few initial challenges are identified with the intent to help the community overcome the associated roadblocks. Grassroot-level end-users of most microfluidic technologies are not

fluid physicists or micro-nano fabrication experts, rather the majority of practitioners consists of clinicians, public health officials, aid workers or NGO volunteers. With this condition in mind, the biggest challenge is to develop pumpless surface microfluidic technology to be as facile as possible, minimizing expert intervention. Integrating the fluid transport and biochemistry with appropriate detection and reporting mechanisms is a key to develop user-friendly POC testing devices. End-user cost is another important parameter, since the demand for such technology is expected to be pervasive in various developing countries. On the technical front, more experiments and fundamental studies need to be performed by the microfluidics research community to identify the operating limits of the pumpless liquid manipulation mechanisms in terms of flow rates, fluid transport distance, material compatibility; especially at the device level. Proof of concept in academic laboratories is a desirable first step for any emerging technology, but the real value is realized when the technology is validated (i.e., it proves equivalent or better than an existing protocol), and emerges as a commercially viable product with a tangible utilization for the common good. Thus, the technology should cater to applications with high product volume and low product cost. As such, interdisciplinary research collaborations involving mechanical engineers, bioengineers, chemical engineers, clinicians etc. are another necessary and important step to filter the gamut of applications in the lab-on-chip domain. The simplicity and universal material compatibility (as long as wettability contrast is achieved) of open-surface, pumpless microfluidics opens boundaries beyond lab-on-chip applications (e.g. heat transfer, jet cooling, personal hygiene products, water management in fuel cells, etc.). Additional research must also be done to identify other domains that can benefit from pumpless surface microfluidics.

## APPENDICES

## Appendix A

### SUPPLEMENTARY INFORMATION FOR CHAPTER 3

#### **A.1 Surface wettability characterization (Section 2)**

Contact angle measurements were performed on the bare and coated (superhydrophobic and superhydrophilic parts) aluminum, paper and PET substrates. Both aluminum and paper exhibited sessile contact angles slightly less than  $90^\circ$ . The PET substrate showed strong wettability (apparently due to a commercial coating on the transparency film used in the experiment).

#### **A.2 Variation of capillary force on droplet with wedge angle $\alpha$ and liquid volume**

##### W

To confirm the validity of Equation 3.2, which indicates that the Laplace pressure gradient on a droplet placed on the wedge-shaped track is proportional to the wedge angle -as long as  $\alpha$  is small- we carried out a separate experiment (see Figure 14(a)) for evaluating the capillary force on the droplet as it began its journey from the narrow end on the track. The experiment was repeated for wedge angles of 0, 2, 3, 4 and 5 degrees. The superhydrophilic tracks were presuffused with water and droplets of known volumes were deposited. The substrates were initially tilted with the wider end up at an angle steep enough so that the forward (i.e., up-slope) capillary force on the liquid bulge could not overcome its in-plane component of weight (acting down-slope), thus keeping the droplet pinned at the narrower end of the track (Figure 37(a)).

## Appendix A (Continued)

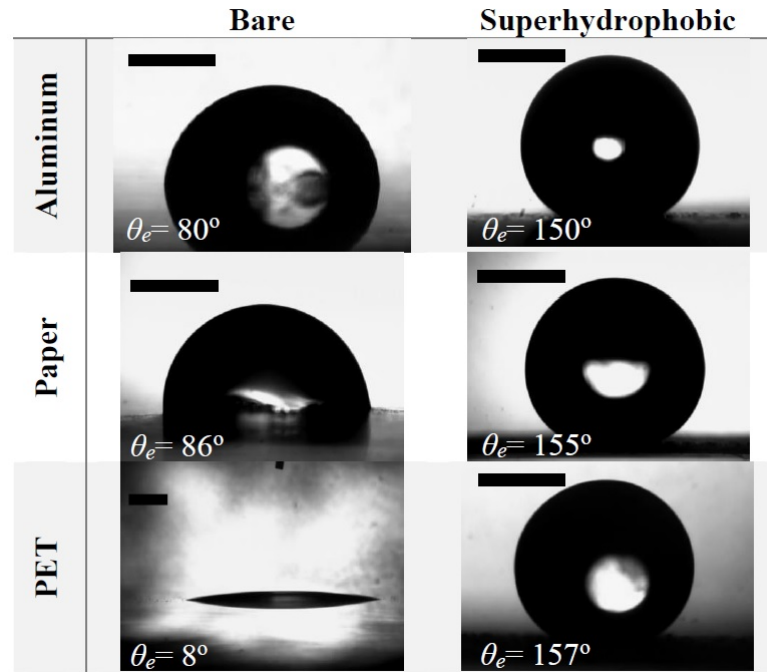


Figure 36. Sessile droplets on the bare substrate (left) and superhydrophobic sections (right) of aluminum, paper and PET substrates. This figure shows one sample image for each substrate taken from several runs used to obtain the  $\theta_e$  data. Each scale bar denotes 1 mm.

Inclination ( $\beta$ ) of the substrate was very slowly decreased until the in-plane component of the droplet weight became lower than the capillary force and the droplet started moving up the plane (Figure 37(b)). For rectangular tracks ( $\alpha = 0^\circ$ ) the liquid bulge deposited on the track did not move (although capillary spreading of the liquid front was observed) even for  $\beta = 0^\circ$  (horizontal surface). For higher wedge angles, the inclination  $\beta$  marking the impending motion of droplets was also higher, implying that the capillary force increased with  $\alpha$ . The capillary force on the liquid bulge, Equation 3.2 suggests, also depends on  $\theta_{avg}$ , which should be a function

## Appendix A (Continued)

of the dispensed droplet volume  $\Omega$ . In order to explore this dependence, we deposited droplets ranging from  $4.7 - 23.5 \text{ ml}$  and recorded the corresponding values of  $\beta$ . Figure 37(c) shows the variation of capillary force  $F_{cx}$  with droplet volume  $\Omega$  for different wedge angles. Each data point was obtained from averaging 60 to 300 readings, while the error bars denote the standard deviation in these readings. For larger wedge angles ( $\alpha = 4^\circ$  and  $5^\circ$ ) the capillary force was too strong to be countered by the weight of small volume droplets, and hence only larger volumes of droplet had to be dispensed. For all the substrates, the droplet volume was found not to influence the capillary force strongly. Therefore, the average  $F_{cx}$  values of Figure 14(b) were plotted using the data sets for each value of  $\alpha$  in Figure 37(c) by averaging over the entire range of droplet volumes used for each  $\alpha$ .

### A.3 Holding capacity of a wedge track

For an isolated superhydrophilic wedge track of finite length on a superhydrophobic background, liquid that is transported from the narrow to the wide end remains confined in the track. If the track is wide enough, the liquid builds up initially creating a rising rivulet from the narrow to the wide end. Further addition of liquid shows that the track retains its pumping ability, with the accumulating height increasing further. When  $\Omega/\delta^3$  exceeds a critical value, a liquid bulge becomes wider than the wide end of the track. For a track of  $60 \text{ mm}$  length and  $4^\circ$  wedge angle the wider end measures  $\delta \sim 4.2 \text{ mm}$ ; the bulge at the wide end did not evolve until 50 droplets of  $4.7 \text{ }\mu\text{L}$  each were deposited at the narrow end and transported there, leading to  $\Omega/\delta^3 = (235/4.23^3) = 3.17$  (see Figure 38).

## Appendix A (Continued)

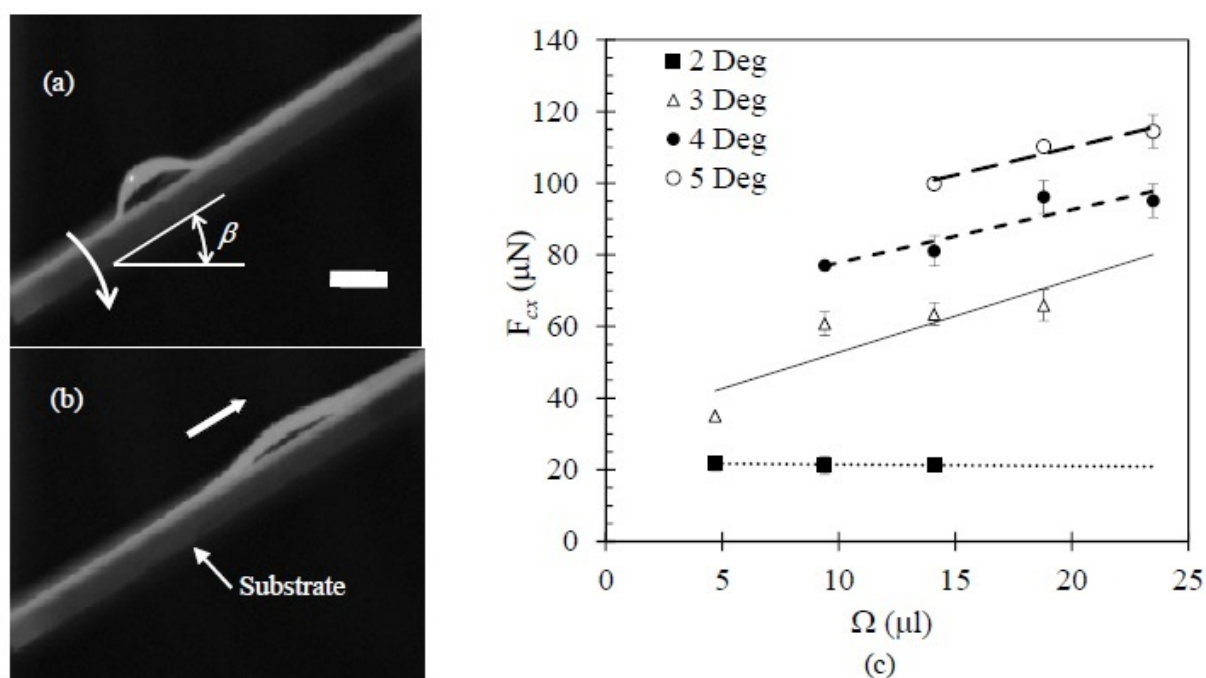


Figure 37. Image of the liquid accumulation on the inclined wedge track (a) just before  $\beta$  reached the critical value below which the liquid bulge started moving up the plane, as shown in (b). (c) Variation of the capillary force on the droplet with droplet volume for different values of wedge angle  $\alpha$ . Scale bar denotes 2 mm.

#### A.4 Effect of pre-wetting (presuffusing)

Figure 39 shows the effect of presuffusing on the capillary pore diameter that is driving hemiwicking. For a dry track, hemiwicking speed is limited by the smallest (deepest) roughness features on the surface. On a presuffused track, these smallest features are already submerged in liquid, leaving larger length-scale features, which in turn limit the hemiwicking speed. Since

## Appendix A (Continued)

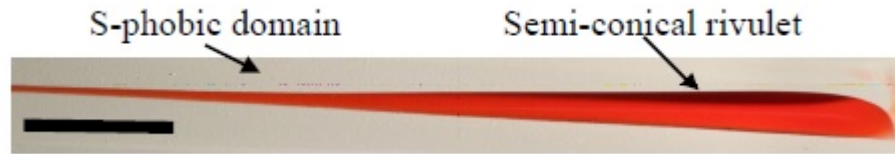


Figure 38. Image of the liquid accumulated after approximately 235  $mL$  of water (dyed for better visualization) were dispensed at the left end of the track. Scale bar denotes 10  $mm$ .

the latter scales linearly with pore diameter, liquid velocity is higher on the presuffused track.

### A.5 Evaluation of acceleration at $t=0$

Figure 40 shows the velocity of the liquid bulge as a function of time as it moved along the presuffused track with  $\alpha = 3^\circ$ ; see Figure 15(a) for the corresponding  $x$  vs.  $t$  plot. As discussed in the main text, the liquid bulge starts from rest due to its inertia. A cubic polynomial fit indicates that the acceleration of the liquid bulge at the inception of the droplet motion was  $dV/dt|_{t=0} = 12.3 \text{ m s}^{-2}$ . This matches closely with the acceleration ( $12 \text{ m s}^{-2}$ ) measured for a 4.7  $mL$  droplet that was driven by a capillary force of 56.3  $mN$  (see Figure 14(b)) on a tilted surface.

### A.6 Capillary bridging

Capillary bridging of the liquid bulges at the wider ends of tracks A and B took place where the surfaces of the two bulges touched. The bridge formed in the air (i.e., the liquid bridge does not touch the substrate at  $t = 0$ ) with an initial thickness  $h_0$ . The two adjacent bulges, which remained pinned to the superhydrophilic tracks, coalesced through progressive growth of

## Appendix A (Continued)

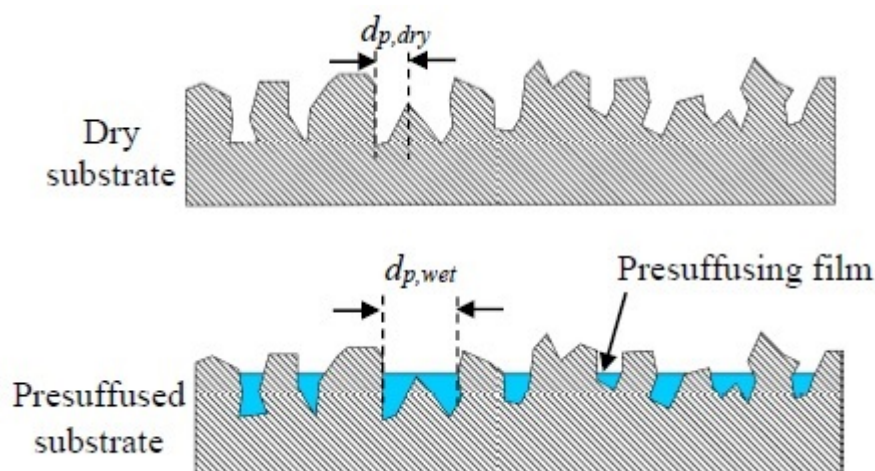


Figure 39. Effect of presuffusing on liquid mobility: for a dry track (top) the smaller surface features (characteristic dimension  $d_{p,dry}$ ) limit the hemiwicking speed. For a presuffused track (bottom), the narrower crevices of the tracks are submerged, and the hemiwicking speed is limited by the relatively larger features ( $d_{p,wet}$ ) of the exposed surface roughness.

the liquid bridge. The width  $h$  of the capillary bridge (as seen from the end view reported in Figure 16(b1) - (e1)) is plotted in Figure 41 for four different runs. The growth rate  $h/h_0$  was found to scale with  $t^{1/2}$ , which is typical of inertia-dominated coalescence (for viscous flow the dependence would have been proportional to  $t$ )(166).

### A.7 Droplet splitting on paper and PET films

Like the droplet bridging circuit, the droplet splitter design also worked equally well on paper and PET substrates. Figure 42(a) shows the images of the three-track design on paper, while Figure 42(b) and (c) show the images of the split volumes of water (colored for visualization) after dispensing 5 (23.5 L) and 15 droplets (70.5 L), respectively. To demonstrate how any eccentricity or bias in the position of the liquid dispenser leads to unequal degrees of liquid

## Appendix A (Continued)

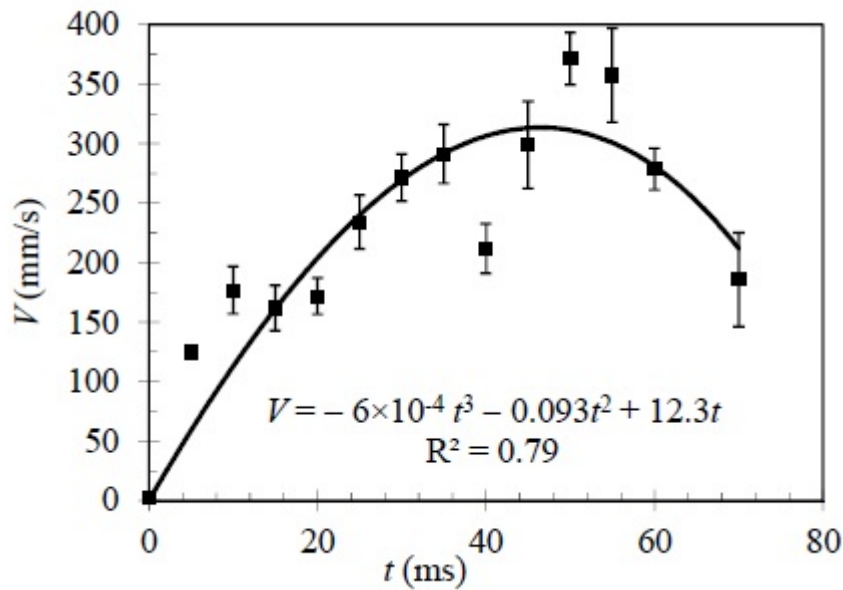


Figure 40. Velocity-time plot of the liquid bulge on a horizontal presuffused track with  $\alpha = 3^\circ$ .

distribution along the splitter limbs, we dispensed 5 droplets (23.5 L) with an offset of 100  $\mu$ m from the center spot. Figure 42(b) shows the extent of the resulting unequal liquid distribution. Figure 42(c1-c4) shows droplet splitting in a 5-splitter design on PET film. The bridged droplet at the early stage of splitting can be seen in frame (c2), while frame (c3) shows the nearly even distribution of the liquid after the split is complete. The central spot can be seen to retain a very small volume. The splitting continues for several consecutive droplets released until the accumulated liquid volume in the radial tracks eventually deters the de-bridging of the central droplet at the end of pumping. Figure 42(c4) shows the liquid accumulation at the end of

## Appendix A (Continued)

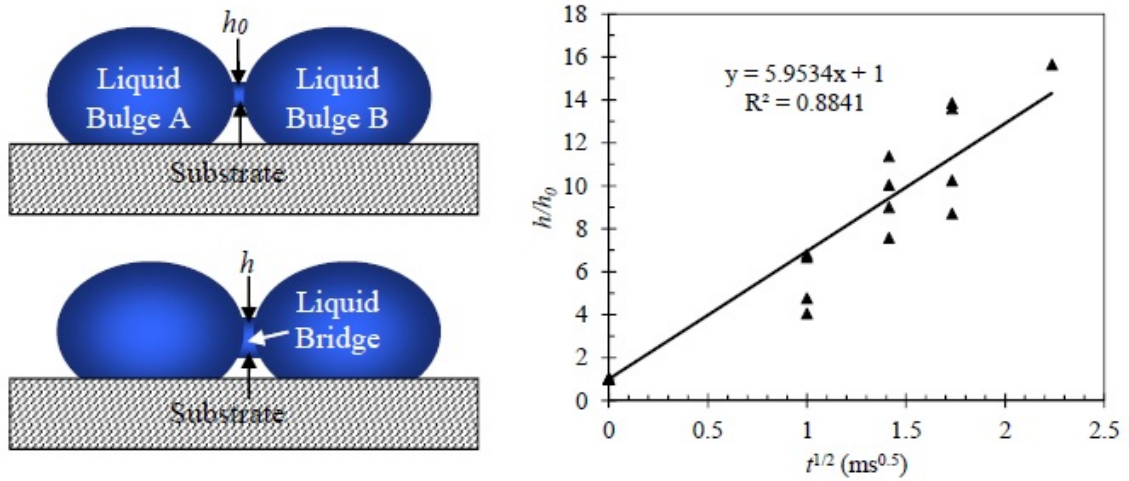


Figure 41. Growth of the capillary bridge thickness (normalized with  $h_0$ , the initial bridge thickness) as measured from Figure 16(b1 - e1) as a function of time. The bridge height exhibits a linear dependence with  $t^{1/2}$  (time scale is in milliseconds).

splitting of 10 consecutive droplets (47 L). This particular design on PET film has been found to work with repeatable features up to 17 consecutive splitting droplets (80 L).

## Appendix A (Continued)

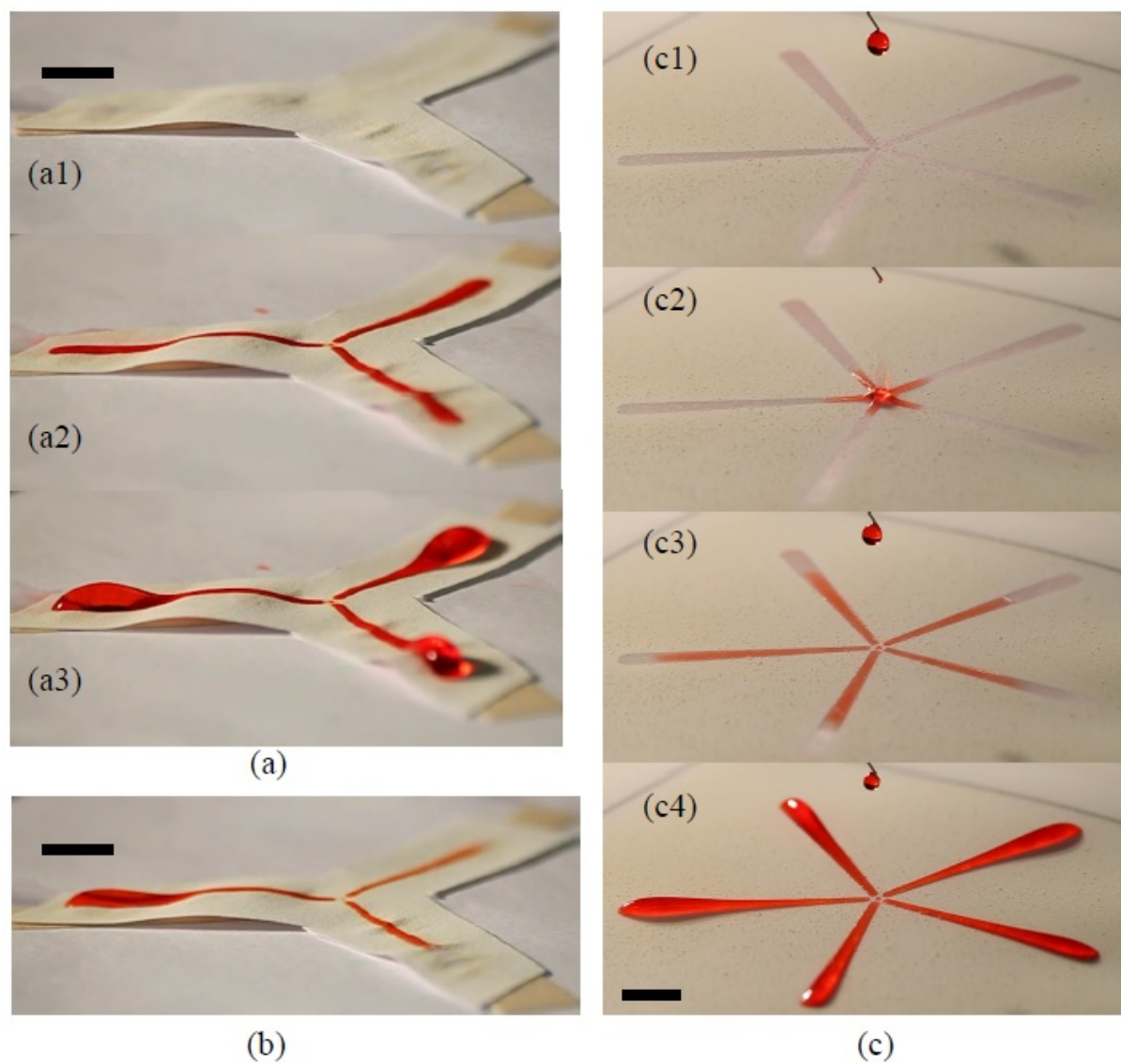


Figure 42. (a - b) Three-way droplet splitting on a paper substrate. (a1) The substrate, (a2) liquid accumulation after perfectly symmetric deposition of 5 drops ( $23.5 \mu\text{L}$ ) at the center, (a3) same, after 15 drops ( $70.5 \mu\text{L}$ ). (b) Biased accumulation after asymmetric splitting of 5 successively dispensed droplets. (c) Five-way droplet splitting on transparency (PET) film: (c1 - c3): sequence of the first droplet split, (c4) liquid accumulation after splitting of 10 droplets ( $47 \mu\text{L}$ ). Scale bars denote 5 mm.

## Appendix B

### SUPPLEMENTARY INFORMATION FOR CHAPTER 4

#### B.1 Evaluation of the largest droplet diameter

Using a custom made MATLAB code, we recorded the largest instantaneous droplet size on each of the hydrophilic strips, at every time stamp, for images taken at 1 minute intervals over a period of 30 minutes. Finally  $D_{max}$  was evaluated by averaging all the largest observable droplet size data (see Figure 44). For example, for  $\lambda = 2000\mu m$ , maximum droplet measurement was done for 6 hydrophilic strips on the surface, while 30 separate images were recorded (one minute apart) over 30 minutes. Therefore, over the viewed region in Figure 44,  $D_{max}$  was obtained by averaging about 180 data points. The number of hydrophilic strips over the viewed regions in Figure 27(a) varied with  $\lambda$ , and so did the total data points that were averaged to arrive at the corresponding  $D_{max}$ . For  $\lambda = 400\mu m$ ,  $D_{max}$  was obtained by averaging over 540 data points.

	Contact Angle Equilibrium	Contact Angle Advancing	Contact Angle Receding
Bare mirror finish aluminum	$78.2^\circ \pm 2^\circ$	$106.8^\circ \pm 1^\circ$	$72.8^\circ \pm 4^\circ$
Superhydrophilic Aluminum	*	*	*
Bare aluminum condition C1 (6 hours)	$76.5^\circ \pm 3^\circ$	$92.1^\circ \pm 2^\circ$	$61.5^\circ \pm 2^\circ$

TABLE V

CONTACT ANGLE FROM DIFFERENT REGIONS OF THE SUBSTRATE. \*CA VALUES TOO LOW TO MEASURE.

## Appendix B (Continued)

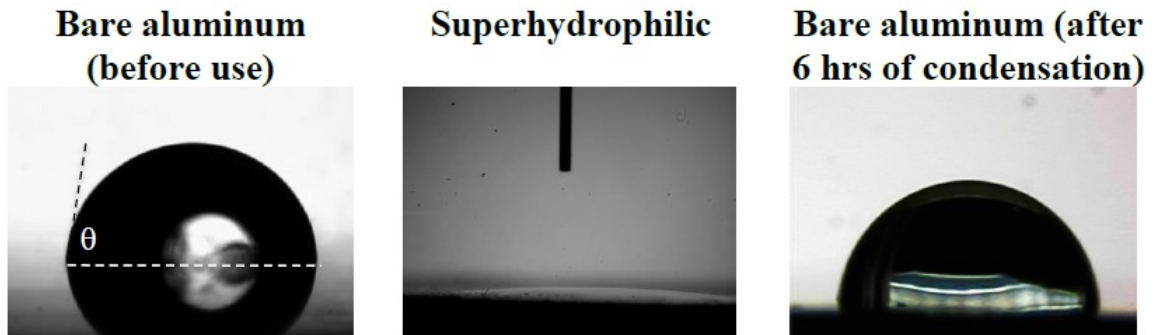


Figure 43. Sessile water droplets on mirror-finish aluminum (left), superhydrophilic region (center), and mirror-finish aluminum priorly subjected to 6 hrs of DWC testing and left to dry.

For  $\lambda = 2500\mu m$ , data were taken over only five hydrophilic strips and 30 images, therefore the average  $D_{max}$  was calculated from 150 data. Similar image analysis was done for all  $\lambda$ . Thus, the  $D_{max}$  we obtain may be reckoned as a spatial and temporal average of the largest visible droplet in the patterned region.

## **B.2 Analysis of vapor phase transport and condensation over an isolated droplet**

Although a large number of studies have been devoted to theoretical and numerical analyses of filmwise condensation in the presence of NCG(167; 168; 169), similar studies on dropwise condensation are rare(170). In the absence of a continuum-based model of gas phase transport and droplet growth in a DWC scenario, we adopt a simplified approach of evaluating the vapor mass fraction and temperature profile in the boundary layer around a droplet(134). For an isolated droplet resting on a surface (on which the water vapor is condensing in a quiescent environment) the vapor mass flux is driven by the radially inward gradient of vapor mass

## Appendix B (Continued)

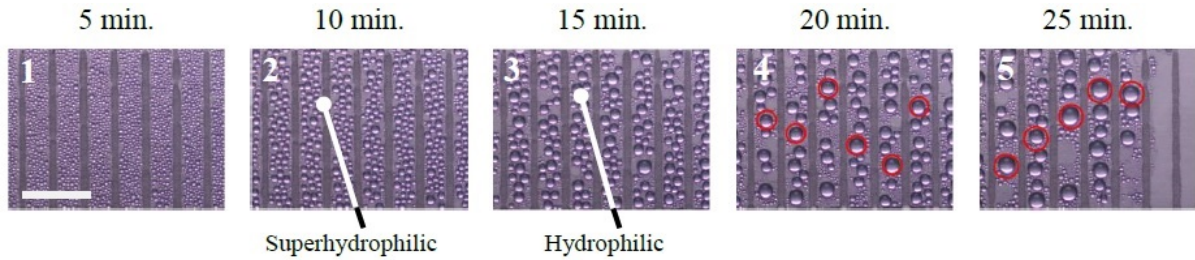


Figure 44. Determination of  $D_{max}$ . Five typical sample images showing the spatio-temporal evolution of condensate droplets on a patterned surface from the onset of DWC. The patterned region was divided in 6 equal strips of width  $\lambda = 2000\mu m$  (hydrophilic) separated by  $400\mu m$  wide superhydrophilic strips. The hydrophilic domains (strips) exhibited sustained DWC, while the superhydrophilic domains (tracks) remained covered in condensate films. A MATLAB code was used to identify the largest droplet in each hydrophilic strip at every time step. The red circles in frames 4 and 5 mark the largest droplet in each vertical strip; a similar exercise was performed for the earlier images. For each line pattern and the corresponding ambient conditions,  $D_{max}$  was determined by averaging the maximum droplet diameter values for each strip and over all times. The white bar in the leftmost frame denotes  $5\text{ mm}$ .

fraction, see Figure 28(a), while at the same time the conservation of mass in the vapor plus NCG phase is satisfied; see Figure 46(a).

$$\frac{d}{dr}(\rho r^2 u_r) = 0 \quad (\text{B.1})$$

The droplet surface is assumed to be impervious to the noncondensable gas so that at any radial position ( $r > r_l$ , the droplet radius) the total radial mass flux  $j_r'' (= j_{rw}'' + j_{rNCG}'')$  is equal to that of the vapor mass flux  $j_{rw}''$ , implying

$$\rho u_r Y_w - \rho D_w \frac{dY_w}{dr} = \rho u_r \quad (\text{B.2})$$

## Appendix B (Continued)

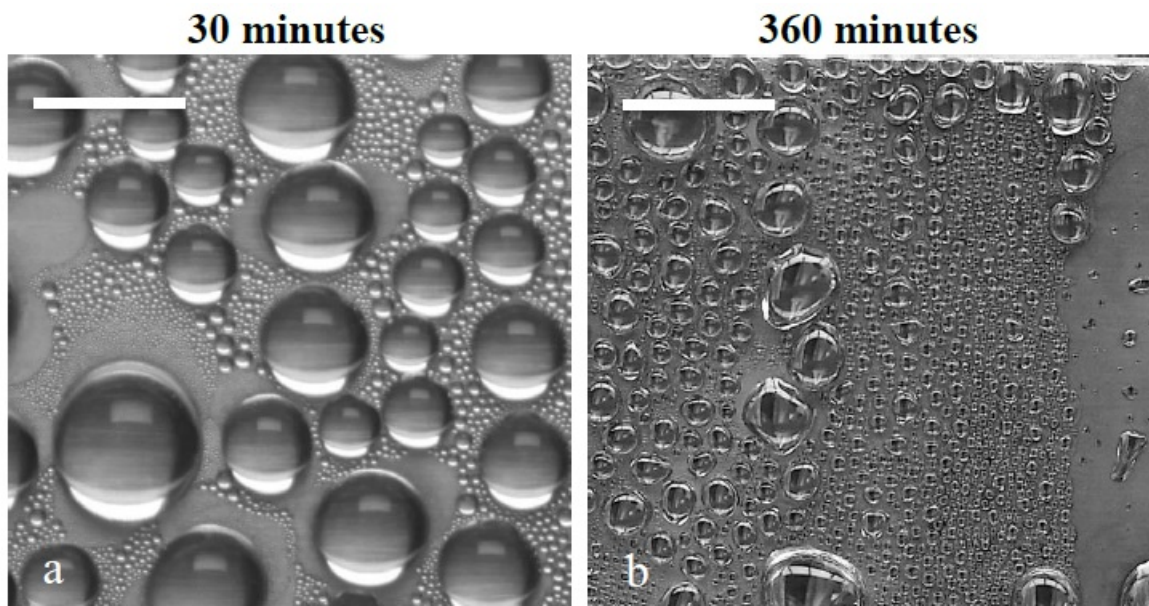


Figure 45. Snapshots of sustained DWC on the control surface after: (a) 30 minutes, and (b) 600 minutes from the inception of condensation under condition C1 (20C DBT, 80% RH, dew point  $\sim 16.5$  °C, substrate temperature  $2.6 \pm 0.3$  °C). No visible transition from DWC to FWC was observed for the duration of the experiment. Note the difference in droplet sizes due to different phases in their surface rejuvenation cycle (nucleation-growth-departure-nucleation). Both scale bars denote 2 mm.

## Appendix B (Continued)

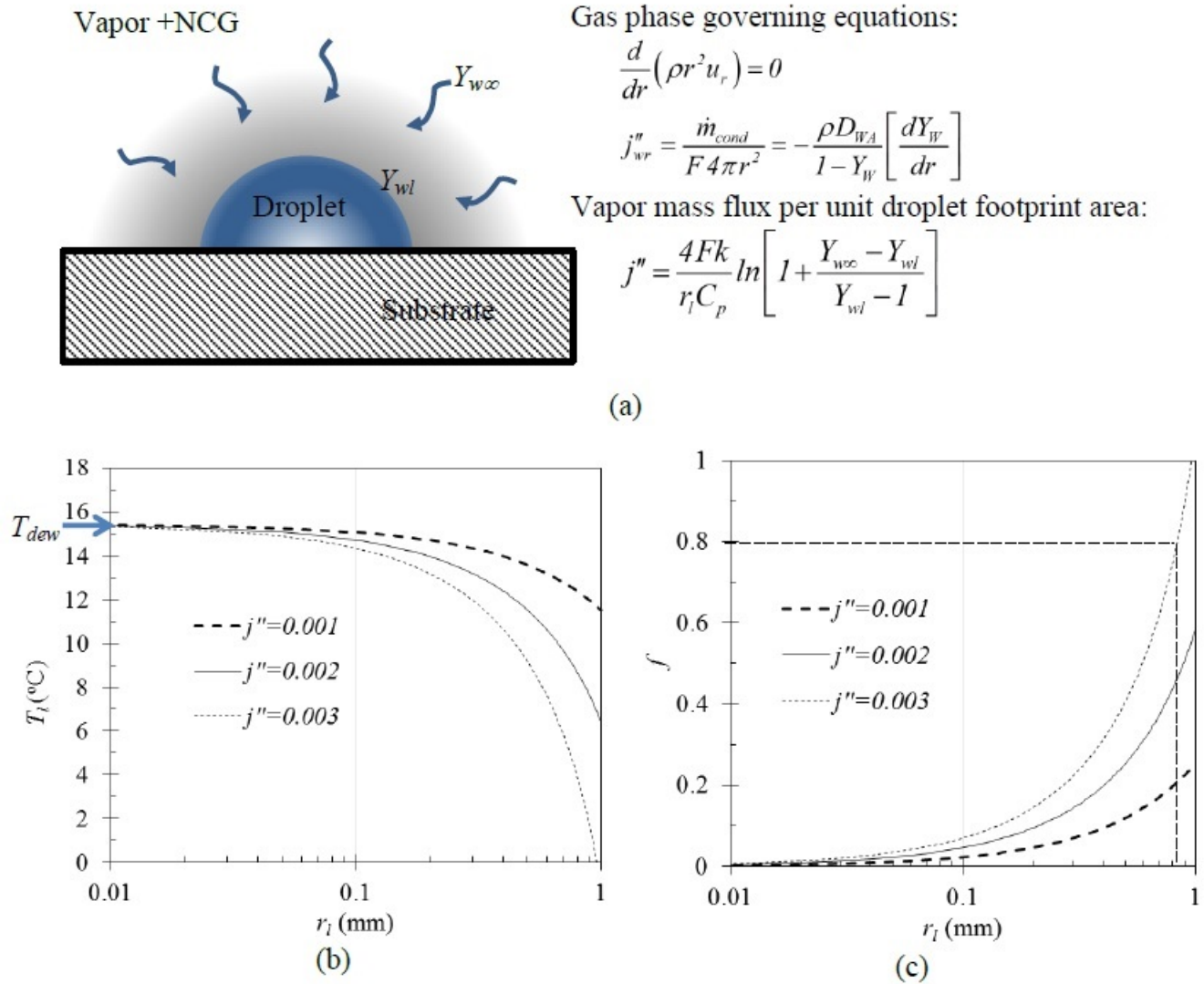


Figure 46. (a) Transport equations governing water vapor mass transport around a single condensate droplet, assuming spherically-symmetric transport over the hemispherical droplet in a quiescent environment.  $F$  denotes the ratio of actual area of the spherical droplet exposed to the gas side to the total surface area of a sphere with the same diameter. Variations of (b) vapor-side temperature on the liquid surface, and (c) fractional temperature drop ( $f = \Delta T_{bl}/\Delta T$ ) with droplet radius for different vapor mass fluxes ( $j''$  in  $kg\ m^{-2}\ s^{-1}$ ).

## Appendix B (Continued)

Reckoning that the radial vapor mass flux for  $r > r_l$  can be written in terms of the condensing mass transfer rate (to the droplet surface),  $j''_{rw} = \rho u_r = \dot{m}_{cond}/4\pi F r^2$ , where  $F$  denotes the fractional area (as compared to a sphere) of the droplet exposed to vapor plus NCG (for a hemispherical droplet  $F = 0.5$ , as assumed in our analysis)

$$\dot{m}_{cond}/4\pi F r^2 = -\frac{\rho D_w}{1 - Y_w} \frac{dY_w}{dr} \quad (\text{B.3})$$

It must be noted that  $\dot{m}_{cond}$  has a negative value for a condensing scenario. Boundary conditions for the differential Equation B.2 are  $Y_w = Y_{wl}$  at  $r = r_l$  (the droplet surface) and  $Y_w = Y_{w\infty}$  at  $r = \infty$  (water vapor mass fraction in the ambient). Assuming the gas phase Lewis number to be unity (so that  $\rho D = k/C_p$ ), solving Equation 3.3 yields

$$\frac{\dot{m}}{4\pi r_l^2 F} = \frac{k}{C_p r_l} \ln \left[ \frac{1 - Y_{w\infty}}{1 - Y_{wl}} \right] \quad (\text{B.4})$$

The condensation mass flux per unit droplet footprint area on the substrate (assuming the droplet to be hemispherical) can be determined from Equation B.4 as

$$j'' = \frac{\dot{m}_{cond}}{\pi r_l^2} = \left( 4Fk/r_l C_p \right) \ln \left[ 1 + B_M \right] \quad (\text{B.5})$$

where  $B_M = \frac{Y_{w\infty} - Y_{wl}}{Y_{wl} - 1}$  is the Spalding transfer number and has a negative value for condensation (134). Equation B.5 describes the relation between the condensation mass flux (per unit substrate area) and the vapor mass fraction condition, but its implicit nature prevents a direct solution. Both the mass flux and  $Y_{wl}$  are unknown, and one has to invoke the energy equation

## Appendix B (Continued)

for the gas and liquid phases. The coupled nature of the vapor species transport (Equation B.2) and energy equations warrants an iterative solution procedure that is beyond the scope of the present discussion.

Assuming local thermodynamic equilibrium near the droplet surface, the liquid surface temperature  $T_l$  may be approximated as the saturation temperature corresponding to the partial pressure of water vapor at the droplet surface, i.e.,

$$T_l = T_{sat}|_{p_l}, \quad \text{where } p_l = \frac{Y_{wl}}{0.376Y_{wl} + 0.624}, \quad \text{and } Y_{wl} = \frac{B_M + Y_{w\infty}}{B_M + l} \quad (\text{B.6})$$

For a given vapor mass flux, the gas phase temperature at the droplet surface can be evaluated from Equation B.5 and Equation B.6. Clearly, the value of  $T_l$  depends on the droplet radius, vapor mass fraction of the free stream and  $B_M$  (which, in turn, is a function of the vapor mass flux). Figure 46(b) shows the variation of  $T_l$  with droplet radius for different vapor mass flux ( $j''$  in  $kg\ m\ s^{-2}\ s^{-1}$ ) conditions for an ambient vapor mass fraction of 0.011 (corresponding to a dew point of  $15.4\ ^\circ C$ ). This figure shows that the effect of NCG in lowering the  $T_l$  is more pronounced for larger droplets. The temperature depression is also larger for the higher mass flux. Figure 46(c) shows the corresponding ( $f = \Delta T_{bl}/\Delta T$ ) values. A larger value of this quantity implies a larger resistance to the overall heat transfer, which is detrimental for condensation. Figure 46(c) indicates that condensation is significantly impeded at large  $j''$  values, particularly on larger droplets. This also underscores the need for control of condensate droplet size on the condensing surface.

## Appendix B (Continued)

It should be noted from Figure 28b that that the HTC for DWC in the presence of NCG is a strong function of  $f$ ; accuracy of the modified Rose model, therefore, depends strongly on the correct estimation of the factor  $f$ . In a practical DWC scenario, where droplets of different sizes exist, Equation B.6 implies that both  $Y_{wl}$  and  $T_l$  would vary spatially on the condenser surface. This would induce an interaction between the boundary layers of neighboring droplets that acts to homogenize the  $Y_{wl}$  and  $T_l$  over droplets of different size. Since the gas phase transport is much faster than its liquid phase counterpart, this would result in an approximately uniform  $\Delta T_{bl}$  across the vapor boundary layer over the condensing plate. However, exact prediction of  $f$  over the entire condensing substrate warrants a detailed CFD analysis, which is beyond the scope of the present study. In the absence of an involved numerical analysis for predicting the resulting vapor mass fraction and temperatures at the liquid surface, we have assumed constant  $f$  values over the entire surface in Figure 28(b). This may not provide an exact value of HTC, but helps to identify the principal factors responsible for HTC improvement.

## Appendix C

### SUPPLEMENTARY INFORMATION FOR CHAPTER 2

#### C.1 Parabolic profile fit of the bulge

The bulge volume exhibits a parabolic shape profile from the side across the length of the bulge. For the semi-analytical analysis we consider this parabolic form to estimate bulge height with total input volume.  $h(x) = ax^2 + bx + c$ . The maximum and minimum deviation of parabolic curve fitted height with the actual height is ranging from  $-3$  to  $+5\%$ .

## Appendix C (Continued)

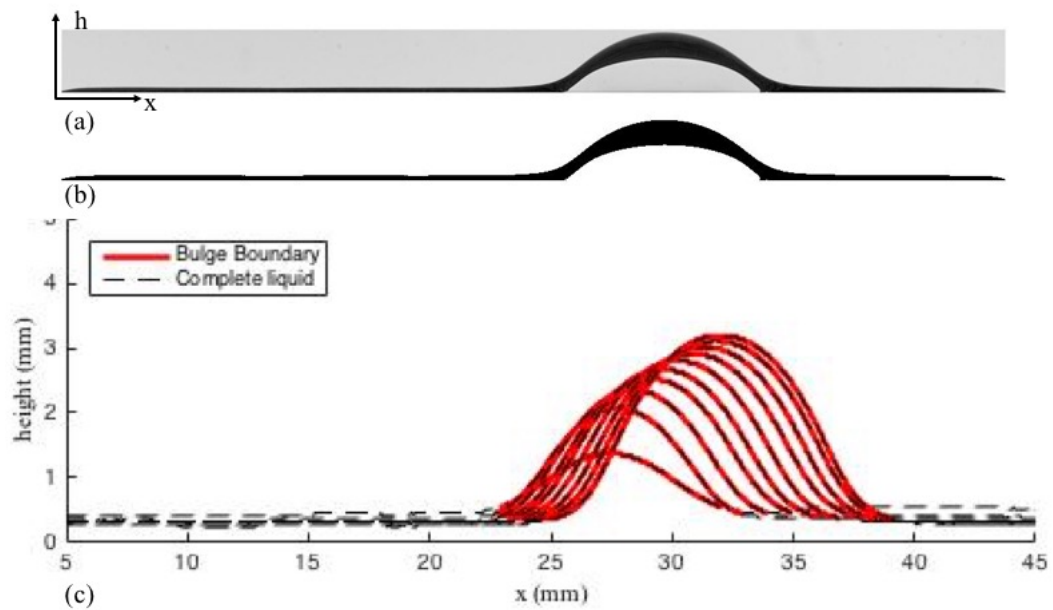


Figure 47. Step by step sequence of image processing. a) Raw image is cropped after identifying the track length from end to end. The origin (0, 0) for estimating height ( $h$ ) and length ( $x$ ) is set to at the lower left corner of the image. b) Image in (a) is processed and converted into binary format (black and white) for simplifying edge detection. A crisp edge at black and white intersection is detected, which is identical to the RAW image. Error is limited to  $\pm 1$  px. c) The code scans every single rows and columns to detect the shift in color (from black to white) to isolate the edges. Black dashed lines traces the height of the liquid profile. Red lines demarcates the bulge boundary.

## Appendix C (Continued)

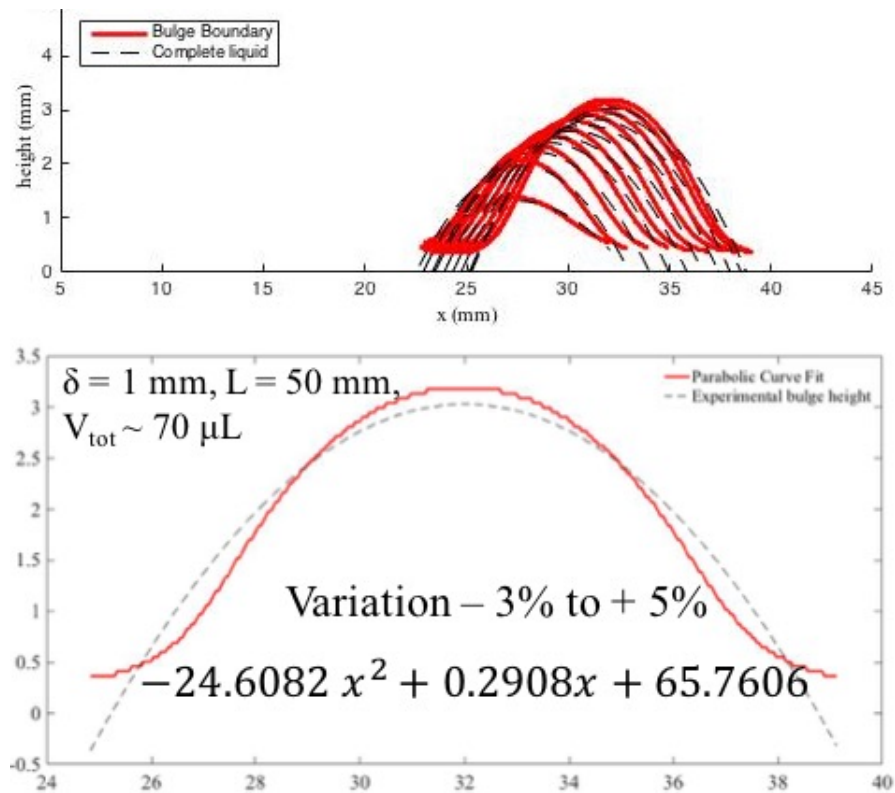


Figure 48. Parabolic curve fitting of the height of bulge volume using a second degree polynomial of  $x$ . a) Shows the curve fitted data (red) overlapped on experimental data (black dashed). Plot for all the bulge volume for a single track width  $\delta = 1000 \mu\text{m}$ ,  $L = 50$  mm is shown. b) Corresponds to a single case where  $V_{tot} = 70 \mu\text{L}$  and track geometry similar to (a).

Appendix D

**COPYRIGHT INFORMATION**

## Appendix D (Continued)

Issue 9, 2014 Previous Article | Next Article

Lab on a Chip  
Journal cover: Lab on a Chip |  
Lab on a Chip

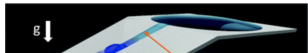
## Wettability patterning for high-rate, pumpless fluid transport on open, non-planar microfluidic platforms

Aritra Ghosh<sup>a</sup>, Ranjan Ganguly<sup>ab</sup>, Thomas M. Schutzius<sup>bc</sup> and Constantine M. Megaridis<sup>a\*</sup>

[Author affiliations](#)

### Abstract

Surface tension driven transport of liquids on open substrates offers an enabling tool for open micro total analysis systems that are becoming increasingly popular for low-cost biomedical diagnostic devices. The present study uses a facile wettability patterning method to produce open microfluidic tracks that – due to their shape, surface texture and chemistry – are capable of transporting a wide range of liquid volumes (~1–500  $\mu\text{L}$ ) on-chip, overcoming viscous and other opposing forces (e.g., gravity) at the pertinent length scales. Small volumes are handled as individual droplets, while larger volumes require repeated droplet transport. The concept is developed and demonstrated with coatings based on  $\text{TiO}_2$  filler particles, which, when present in adequate (~80 wt.%) quantities within a hydrophobic fluoroacrylic polymer matrix, form composites that are intrinsically superhydrophobic. Such composite coatings become superhydrophilic upon exposure to UV light (390 nm). A commercial laser printer-based photo-masking approach is used on the coating for spatially selective wettability conversion from superhydrophobic to superhydrophilic. Carefully designed wedge-patterned surface tension confined tracks on the open-air devices move liquid on them without power input, even when acting against gravity. Simple designs of wettability patterning are used on versatile substrates (e.g., metals, polymers, paper) to demonstrate complex droplet handling tasks, e.g., merging, splitting and metered dispensing, some of which occur in 3-D geometries. Fluid transport rates of up to  $350 \mu\text{L s}^{-1}$  are attained. Applicability of the design on metal substrates allows these devices to be used also for other microscale engineering applications, e.g., water management in fuel cells.



About	Cited by	Related
<p>Material from a third party non-RSC publication you must <a href="#">formally request permission</a> using RightsLink. Go to our <a href="#">Instructions for using RightsLink page</a> for details.</p> <p>Authors contributing to RSC publications (journal articles, books or book chapters) do not need to formally request permission to reproduce material contained in this article provided that the correct acknowledgement is given with the reproduced material.</p> <p>Reproduced material should be attributed as follows:</p> <ul style="list-style-type: none"> <li>For reproduction of material from NJC: Reproduced from Ref. XX with permission from the Centre National de la Recherche Scientifique (CNRS) and The Royal Society of Chemistry.</li> <li>For reproduction of material from PCCP: Reproduced from Ref. XX with permission from the PCCP Owner Societies.</li> <li>For reproduction of material from PPS: Reproduced from Ref. XX with permission from the European Society for Photobiology, the European Photochemistry Association, and The Royal Society of Chemistry.</li> <li>For reproduction of material from all other RSC journals and books: Reproduced from Ref. XX with permission from The Royal Society of Chemistry.</li> </ul> <p>If the material has been adapted instead of reproduced from the original RSC publication 'Reproduced from' can be substituted with 'Adapted from'.</p> <p>In all cases the Ref. XX is the XXth reference in the list of references.</p> <p>If you are the author of this article you do not need to formally request permission to reproduce figures, diagrams etc. contained in this article in third party publications or in a thesis or dissertation provided that the correct acknowledgement is given with the reproduced material.</p> <p>Reproduced material should be attributed as follows:</p>		

Figure 49. Copyright screen shot for Chapter 3

## Appendix D (Continued)

Gmail - Regarding Incident 1310756 (CMI: MCID041153) 4/17/18, 6:05 PM

 Gmail aritra ghosh <aritra.jadavpur@gmail.com>

---

**Regarding Incident 1310756 {CMI: MCID041153}**

support@services.acs.org <support@services.acs.org> Tue, Apr 17, 2018 at 3:10 PM  
To: aritra.jadavpur@gmail.com



Dear Dr.Ghosh,

Thank you for contacting ACS Publications Support.

Your permission request is granted and there is no fee for this reuse. In your planned reuse, you must cite the ACS article as the source, add this direct link <https://pubs.acs.org/doi/abs/10.1021/ta5028866> and include a notice to readers that further permissions related to the material excerpted should be directed to the ACS.

I hope this is helpful and if you need further assistance, please feel free to contact me.

Sincerely,

Ashley Gibson  
ACS Publications  
Customer Services & Information  
Website: <https://help.acs.org>

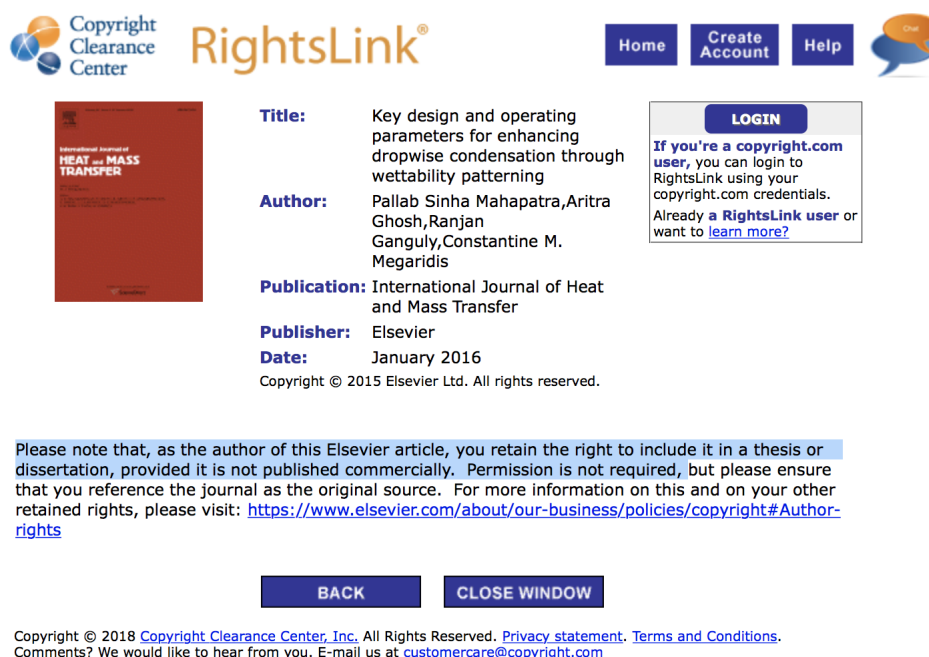
Incident Information:

Incident:	1310756
Incident Created:	2018-04-17T02:24:18
Short Description:	Requesting permission to reuse a Langmuir article for thesis chapter. I am the first author.
Description:	Dear Sir,

<https://mail.google.com/mail/u/1/?ui=2&ik=4e1c809b4c&jsver=4NKE...iew=pt&msg=162d5046ce8a66d8&search=inbox&siml=162d5046ce8a66d8> Page 1 of 2

Figure 50. Copyright screen shot for Chapter 4

## Appendix D (Continued)



The screenshot displays the Copyright Clearance Center RightsLink interface. At the top left is the Copyright Clearance Center logo, and next to it is the RightsLink logo. On the top right, there are navigation buttons for 'Home', 'Create Account', and 'Help', along with a 'Chat' icon. The main content area features a red cover image of the 'International Journal of HEAT and MASS TRANSFER'. To the right of the image, the following details are listed:

- Title:** Key design and operating parameters for enhancing dropwise condensation through wettability patterning
- Author:** Pallab Sinha Mahapatra, Aritra Ghosh, Ranjan Ganguly, Constantine M. Megaridis
- Publication:** International Journal of Heat and Mass Transfer
- Publisher:** Elsevier
- Date:** January 2016

Below the article details, there is a 'LOGIN' button and a text box that reads: "If you're a copyright.com user, you can login to RightsLink using your copyright.com credentials. Already a RightsLink user or want to learn more?". At the bottom of the interface, there are two buttons: 'BACK' and 'CLOSE WINDOW'. A footer at the very bottom contains the following text: "Copyright © 2018 Copyright Clearance Center, Inc. All Rights Reserved. Privacy statement. Terms and Conditions. Comments? We would like to hear from you. E-mail us at [customercare@copyright.com](mailto:customercare@copyright.com)".

Figure 51. Copyright screen shot for Chapter 5

## CITED LITERATURE

1. Manz, A., Harrison, D. J., Verpoorte, E. M., Fettingner, J. C., Paulus, A., Lüdi, H., and Widmer, H. M.: Planar chips technology for miniaturization and integration of separation techniques into monitoring systems: capillary electrophoresis on a chip. Journal of Chromatography A, 593(1):253–258, 1992.
2. Whitesides, G. M.: The origins and the future of microfluidics. Nature, 442(7101):368–373, 2006.
3. Bruus, H.: Theoretical Microfluidics. Oxford Publishing, 2006.
4. Haeberle, S. and Zengerle, R.: Microfluidic platforms for lab-on-a-chip applications. Lab on a Chip, 7(9):1094–1110, 2007.
5. Foresti, D., Nabavi, M., Klingauf, M., Ferrari, A., and Poulikakos, D.: Acoustophoretic contactless transport and handling of matter in air. Proceedings of the National Academy of Sciences, 110(31):12549–12554, 2013.
6. Puri, I. K. and Ganguly, R.: Particle transport in therapeutic magnetic fields. Annual Review of Fluid Mechanics, 46:407–440, 2014.
7. Sackmann, E. K., Fulton, A. L., and Beebe, D. J.: The present and future role of microfluidics in biomedical research. Nature, 507(7491):181–189, 2014.
8. Hourtane, V., Bodiguel, H., and Colin, A.: Dense bubble traffic in microfluidic loops: Selection rules and clogging. Physical Review E, 93(3):032607, 2016.
9. Cong, H., Xu, X., Yu, B., Liu, H., and Yuan, H.: Fabrication of anti-protein-fouling poly (ethylene glycol) microfluidic chip electrophoresis by sandwich photolithography. Biomicrofluidics, 10(4):044106, 2016.
10. Unger, M. A., Chou, H.-P., Thorsen, T., Scherer, A., and Quake, S. R.: Monolithic microfabricated valves and pumps by multilayer soft lithography. Science, 288(5463):113–116, 2000.

11. Sia, S. K. and Whitesides, G. M.: Microfluidic devices fabricated in poly (dimethylsiloxane) for biological studies. Electrophoresis, 24(21):3563–3576, 2003.
12. Guckenberger, D. J., de Groot, T. E., Wan, A. M., Beebe, D. J., and Young, E. W.: Micromilling: a method for ultra-rapid prototyping of plastic microfluidic devices. Lab on a Chip, 15(11):2364–2378, 2015.
13. Madou, M. J.: Fundamentals of microfabrication: the science of miniaturization. CRC press, 2002.
14. Anderson, J. R., Chiu, D. T., Wu, H., Schueller, O., and Whitesides, G. M.: Fabrication of microfluidic systems in poly (dimethylsiloxane). Electrophoresis, 21(1):27–40, 2000.
15. Ghosh, A., Ganguly, R., Schutzius, T. M., and Megaridis, C. M.: Wettability patterning for high-rate, pumpless fluid transport on open, non-planar microfluidic platforms. Lab on a Chip, 14(9):1538–1550, 2014.
16. Chatterjee, S., S. Mahapatra, P., Ibrahim, A., Ganguly, R., Megaridis, C., Yu, L., and Dodge, R.: Capillary-driven, spatially-directed liquid transport on and through thin porous substrates. In APS Meeting Abstracts, 2016.
17. Zhao, Y., Wang, H., Zhou, H., and Lin, T.: Directional fluid transport in thin porous materials and its functional applications. Small, 2016.
18. Smith, J. D., Dhiman, R., Anand, S., Reza-Garduno, E., Cohen, R. E., McKinley, G. H., and Varanasi, K. K.: Droplet mobility on lubricant-impregnated surfaces. Soft Matter, 9(6):1772–1780, 2013.
19. Simpson, J. T., Hunter, S. R., and Aytug, T.: Superhydrophobic materials and coatings: a review. Reports on Progress in Physics, 78(8):086501, 2015.
20. Martinez, A. W., Phillips, S. T., Whitesides, G. M., and Carrilho, E.: Diagnostics for the developing world: microfluidic paper-based analytical devices. Analytical Chemistry, 82(1):3–10, 2009.
21. Nelson, W. C. and Kim, C.-J. : Droplet actuation by electrowetting-on-dielectric (ewod): a review. Journal of Adhesion Science and Technology, 26(12-17):1747–1771, 2012.

22. Gau, H., Herminghaus, S., Lenz, P., and Lipowsky, R.: Liquid morphologies on structured surfaces: from microchannels to microchips. Science, 283(5398):46–49, 1999.
23. Schutzius, T. M., Elsharkawy, M., Tiwari, M. K., and Megaridis, C. M.: Surface tension confined (stc) tracks for capillary-driven transport of low surface tension liquids. Lab on a Chip, 12(24):5237–5242, 2012.
24. De Gennes, P.-G., Brochard-Wyart, F., and Quéré, D.: Capillarity and wetting phenomena: drops, bubbles, pearls, waves. Springer Science & Business Media, 2013.
25. Quéré, D.: Wetting and roughness. Annu. Rev. Mater. Res., 38:71–99, 2008.
26. Cate, D. M., Adkins, J. A., Mettakoonpitak, J., and Henry, C. S.: Recent developments in paper-based microfluidic devices. Analytical Chemistry, 87(1):19–41, 2014.
27. Bonn, D., Eggers, J., Indekeu, J., Meunier, J., and Rolley, E.: Wetting and spreading. Reviews of Modern Physics, 81(2):739, 2009.
28. Xing, S., Harake, R. S., and Pan, T.: Droplet-driven transports on superhydrophobic-patterned surface microfluidics. Lab on a Chip, 11(21):3642–3648, 2011.
29. Cira, N., Benusiglio, A., and Prakash, M.: Vapour-mediated sensing and motility in two-component droplets. Nature, 519(7544):446–450, 2015.
30. Chakraborty, M., Ghosh, U. U., Chakraborty, S., and DasGupta, S.: Thermally enhanced self-propelled droplet motion on gradient surfaces. RSC Advances, 5(56):45266–45275, 2015.
31. Chaudhury, M. K. and Whitesides, G. M.: How to make water run uphill. Science, 256(5063):1539–1541, 1992.
32. Martinez, A. W., Phillips, S. T., Butte, M. J., and Whitesides, G. M.: Patterned paper as a platform for inexpensive, low-volume, portable bioassays. Angewandte Chemie International Edition, 46(8):1318–1320, 2007.
33. Choudhary, T., Rajamanickam, G., and Dendukuri, D.: Woven electrochemical fabric-based test sensors (wefts): a new class of multiplexed electrochemical sensors. Lab on a Chip, 15(9):2064–2072, 2015.

34. Darhuber, A. A., Valentino, J. P., Troian, S. M., and Wagner, S.: Thermocapillary actuation of droplets on chemically patterned surfaces by programmable microheater arrays. Journal of Microelectromechanical Systems, 12(6):873–879, 2003.
35. Zhao, Y., Liu, F., and Chen, C.-H.: Thermocapillary actuation of binary drops on solid surfaces. Applied Physics Letters, 99(10):104101, 2011.
36. Linke, H., Alemán, B., Melling, L., Taormina, M., Francis, M., Dow-Hygelund, C., Narayanan, V., Taylor, R., and Stout, A.: Self-propelled leidenfrost droplets. Physical Review Letters, 96(15):154502, 2006.
37. Leidenfrost, J. G.: De aquae communis nonnullis qualitatibus tractatus. Ovenius, 1756.
38. Lagubeau, G., Le Merrer, M., Clanet, C., and Quéré, D.: Leidenfrost on a ratchet. Nature Physics, 7(5):395–398, 2011.
39. Bliznyuk, O., Jansen, H. P., Kooij, E. S., Zandvliet, H. J., and Poelsema, B.: Smart design of stripe-patterned gradient surfaces to control droplet motion. Langmuir, 27(17):11238–11245, 2011.
40. Dos Santos, F. D. and Ondarcohu, T.: Free-running droplets. Physical Review Letters, 75(16):2972, 1995.
41. Zorba, V., Persano, L., Pisignano, D., Athanassiou, A., Stratakis, E., Cingolani, R., Tzanetakos, P., and Fotakis, C.: Making silicon hydrophobic: wettability control by two-lengthscale simultaneous patterning with femtosecond laser irradiation. Nanotechnology, 17(13):3234, 2006.
42. Yang, J.-T., Yang, Z.-H., Chen, C.-Y., and Yao, D.-J.: Conversion of surface energy and manipulation of a single droplet across micropatterned surfaces. Langmuir, 24(17):9889–9897, 2008.
43. Lv, C. and Hao, P.: Driving droplet by scale effect on microstructured hydrophobic surfaces. Langmuir, 28(49):16958–16965, 2012.
44. Sommers, A., Brest, T., and Eid, K.: Topography-based surface tension gradients to facilitate water droplet movement on laser-etched copper substrates. Langmuir, 29(38):12043–12050, 2013.

45. Alheshibri, M., Rogers, N., Sommers, A., and Eid, K.: Spontaneous movement of water droplets on patterned cu and al surfaces with wedge-shaped gradients. Applied Physics Letters, 102(17):174103, 2013.
46. Darhuber, A. A., Troian, S. M., and Reisner, W. W.: Dynamics of capillary spreading along hydrophilic microstripes. Physical Review E, 64(3):031603, 2001.
47. Washburn, E.: Ew washburn, phys. rev. 17, 273 (1921). Phys. Rev., 17:273, 1921.
48. Brinkmann, M. and Lipowsky, R.: Wetting morphologies on substrates with striped surface domains. Journal of applied physics, 92(8):4296–4306, 2002.
49. Lipowsky, R., Brinkmann, M., Dimova, R., Franke, T., Kierfeld, J., and Zhang, X.: Droplets, bubbles, and vesicles at chemically structured surfaces. Journal of Physics: Condensed Matter, 17(9):S537, 2005.
50. Yu, Z., Yu, Y., Li, Y., Song, S., Huo, S., and Han, X.: Preparation and characterization of super-hydrophobic surfaces on aluminum and stainless steel substrates. Surface Review and Letters, 17(03):375–381, 2010.
51. Wilson, P. W., Lu, W., Xu, H., Kim, P., Kreder, M. J., Alvarenga, J., and Aizenberg, J.: Inhibition of ice nucleation by slippery liquid-infused porous surfaces (slips). Physical Chemistry Chemical Physics, 15(2):581–585, 2013.
52. Ghosh, A., Beaini, S., Zhang, B. J., Ganguly, R., and Megaridis, C. M.: Enhancing dropwise condensation through bioinspired wettability patterning. Langmuir, 30(43):13103–13115, 2014.
53. Choi, K., Ng, A. H., Fobel, R., and Wheeler, A. R.: Digital microfluidics. Annual review of analytical chemistry, 5:413–440, 2012.
54. Nelson, W. C. and Kim, C.-J. .: Droplet actuation by electrowetting-on-dielectric (ewod): A review. Journal of Adhesion Science and Technology, 26(12-17):1747–1771, 2012.
55. Park, S.-Y., Teitell, M. A., and Chiou, E. P.: Single-sided continuous optoelectrowetting (scoew) for droplet manipulation with light patterns. Lab on a Chip, 10(13):1655–1661, 2010.

56. Long, Z., Shetty, A. M., Solomon, M. J., and Larson, R. G.: Fundamentals of magnet-actuated droplet manipulation on an open hydrophobic surface. Lab on a Chip, 9(11):1567–1575, 2009.
57. Seo, J., Lee, S., Lee, J., and Lee, T.: Guided transport of water droplets on superhydrophobic–hydrophilic patterned si nanowires. ACS applied materials & interfaces, 3(12):4722–4729, 2011.
58. Mertaniemi, H., Jokinen, V., Sainiemi, L., Franssila, S., Marmur, A., Ikkala, O., and Ras, R. H.: Superhydrophobic tracks for low-friction, guided transport of water droplets. Advanced Materials, 23(26):2911–2914, 2011.
59. Darhuber, A. A., Valentino, J. P., Troian, S. M., and Wagner, S.: Thermocapillary actuation of droplets on chemically patterned surfaces by programmable microheater arrays. Journal of Microelectromechanical Systems, 12(6):873–879, 2003.
60. Wang, Z. and Zhe, J.: Recent advances in particle and droplet manipulation for lab-on-a-chip devices based on surface acoustic waves. Lab on a Chip, 11(7):1280–1285, 2011.
61. Foresti, D., Nabavi, M., Klingauf, M., Ferrari, A., and Poulikakos, D.: Acoustophoretic contactless transport and handling of matter in air. Proceedings of the National Academy of Sciences, 110(31):12549–12554, 2013.
62. Darhuber, A. A. and Troian, S. M.: Principles of microfluidic actuation by modulation of surface stresses. Annu. Rev. Fluid Mech., 37:425–455, 2005.
63. Chen, Y.-J., Nagamine, Y., and Yoshikawa, K.: Self-propelled motion of a droplet induced by marangoni-driven spreading. Physical Review E, 80(1):016303, 2009.
64. Kooij, E., Jansen, H., Bliznyuk, O., Poelsema, B., and Zandvliet, H.: Directional wetting on chemically patterned substrates. Colloids and Surfaces A: Physicochemical and Engineering Aspects, 413:328–333, 2012.
65. Chandesris, B., Soupremanien, U., and Dunoyer, N.: Uphill motion of droplets on tilted and vertical grooved substrates induced by a wettability gradient. Colloids and Surfaces A: Physicochemical and Engineering Aspects, 434:126–135, 2013.

66. Lai, Y.-H., Yang, J.-T., and Shieh, D.-B.: A microchip fabricated with a vapor-diffusion self-assembled-monolayer method to transport droplets across superhydrophobic to hydrophilic surfaces. Lab on a Chip, 10(4):499–504, 2010.
67. Khoo, H. S. and Tseng, F.-G.: Spontaneous high-speed transport of subnanoliter water droplet on gradient nanotextured surfaces. Applied Physics Letters, 95(6):063108, 2009.
68. Jokinen, V., Sainiemi, L., and Franssila, S.: Complex droplets on chemically modified silicon nanograss. Advanced Materials, 20(18):3453–3456, 2008.
69. Nakajima, A., Nakagawa, Y., Furuta, T., Sakai, M., Isobe, T., and Matsushita, S.: Sliding of water droplets on smooth hydrophobic silane coatings with regular triangle hydrophilic regions. Langmuir, 29(29):9269–9275, 2013.
70. Jokinen, V., Kostianen, R., and Sikanen, T.: Multiphase designer droplets for liquid-liquid extraction. Advanced Materials, 24(46):6240–6243, 2012.
71. Lee, M., Chang, Y. S., and Kim, H.-Y.: Drop impact on microwetting patterned surfaces. Physics of Fluids, 22(7):072101, 2010.
72. Kim, S., Moon, M.-W., and Kim, H.-Y.: Drop impact on super-wettability-contrast annular patterns. Journal of Fluid Mechanics, 730:328–342, 2013.
73. Balu, B., Berry, A. D., Hess, D. W., and Breedveld, V.: Patterning of superhydrophobic paper to control the mobility of micro-liter drops for two-dimensional lab-on-paper applications. Lab on a Chip, 9(21):3066–3075, 2009.
74. Chitnis, G., Ding, Z., Chang, C.-L., Savran, C. A., and Ziaie, B.: Laser-treated hydrophobic paper: an inexpensive microfluidic platform. Lab on a Chip, 11(6):1161–1165, 2011.
75. Xing, S., Jiang, J., and Pan, T.: Interfacial microfluidic transport on micropatterned superhydrophobic textile. Lab on a Chip, 13(10):1937–1947, 2013.
76. Göröcs, Z., Ling, Y., Dai Yu, M., Karahalios, D., Mogharabi, K., Lu, K., Wei, Q., and Ozcan, A.: Giga-pixel fluorescent imaging over an ultra-large field-of-view using a flatbed scanner. Lab on a Chip, 13(22):4460–4466, 2013.

77. Cheng, J.-T. and Chen, C.-L.: Adaptive chip cooling using electrowetting on coplanar control electrodes. Nanoscale and Microscale Thermophysical Engineering, 14(2):63–74, 2010.
78. Kandlikar, S. G.: Microscale and macroscale aspects of water management challenges in pem fuel cells. Heat Transfer Engineering, 29(7):575–587, 2008.
79. Hirayanagi, T., Tsukamoto, T., Esashi, M., and Tanaka, S.: Micro thermal diode with glass thermal insulation structure embedded in vapor chamber. In Journal of Physics: Conference Series, volume 476, page 012019. IOP Publishing, 2013.
80. Takeuchi, M., Sakamoto, K., Martra, G., Coluccia, S., and Anpo, M.: Mechanism of photoinduced superhydrophilicity on the tio<sub>2</sub> photocatalyst surface. The journal of physical chemistry B, 109(32):15422–15428, 2005.
81. Yang, M., Di, Z., and Lee, J.-K.: Facile control of surface wettability in tio<sub>2</sub>/poly (methyl methacrylate) composite films. Journal of colloid and interface science, 368(1):603–607, 2012.
82. Tadanaga, K., Morinaga, J., Matsuda, A., and Minami, T.: Superhydrophobic- superhydrophilic micropatterning on flowerlike alumina coating film by the sol- gel method. Chemistry of materials, 12(3):590–592, 2000.
83. Lorenceau, É. and Quéré, D.: Drops on a conical wire. Journal of Fluid Mechanics, 510:29–45, 2004.
84. Kusumaatmaja, H. and Lipowsky, R.: Equilibrium morphologies and effective spring constants of capillary bridges. Langmuir, 26(24):18734–18741, 2010.
85. Eiswirth, R., Bart, H.-J., Ganguli, A., and Kenig, E.: Experimental and numerical investigation of binary coalescence: Liquid bridge building and internal flow fields. Physics of Fluids, 24(6):062108, 2012.
86. Cassie, A. and Baxter, S.: Wettability of porous surfaces. Transactions of the Faraday society, 40:546–551, 1944.
87. Beér, J. M.: High efficiency electric power generation: The environmental role. Progress in Energy and Combustion Science, 33(2):107–134, 2007.

88. Zhang, F., Yang, X., and Wang, C.: Liquid water removal from a polymer electrolyte fuel cell. Journal of the Electrochemical Society, 153(2):A225–A232, 2006.
89. Peters, T. B., McCarthy, M., Allison, J., Dominguez-Espinosa, F. A., Jenicek, D., Kariya, H. A., Staats, W. L., Brisson, J. G., Lang, J. H., and Wang, E. N.: Design of an integrated loop heat pipe air-cooled heat exchanger for high performance electronics. IEEE Transactions on Components, Packaging and Manufacturing Technology, 2(10):1637–1648, 2012.
90. Liu, L. and Jacobi, A. M.: The effects of hydrophilicity on water drainage and condensate retention on air-conditioning evaporators. 2006.
91. Lee, A., Moon, M.-W., Lim, H., Kim, W.-D., and Kim, H.-Y.: Water harvest via dewing. Langmuir, 28(27):10183–10191, 2012.
92. Bejan, A.: Entropy generation through heat and fluid flow. Wiley, 1982.
93. Rose, J.: Dropwise condensation theory and experiment: a review. Proceedings of the Institution of Mechanical Engineers, Part A: Journal of Power and Energy, 216(2):115–128, 2002.
94. Schmidt, E., Schurig, W., and Sellschopp, W.: Versuche über die kondensation von wasserdampf in film-und tropfenform. Technische Mechanik und Thermodynamik, 1(2):53–63, 1930.
95. Chen, X., Wu, J., Ma, R., Hua, M., Koratkar, N., Yao, S., and Wang, Z.: Nanograssed micropyramidal architectures for continuous dropwise condensation. Advanced functional materials, 21(24):4617–4623, 2011.
96. Patankar, N. A.: Supernucleating surfaces for nucleate boiling and dropwise condensation heat transfer. Soft Matter, 6(8):1613–1620, 2010.
97. Varanasi, K. K., Hsu, M., Bhate, N., Yang, W., and Deng, T.: Spatial control in the heterogeneous nucleation of water. Applied Physics Letters, 95(9):094101, 2009.
98. Volmer, M. and Weber, A.: Keimbildung in übersättigten gebilden. Z. phys. Chem, 119(3/4):277–301, 1926.
99. Kim, S. and Kim, K. J.: Dropwise condensation modeling suitable for superhydrophobic surfaces. Journal of heat transfer, 133(8):081502, 2011.

100. Tanaka, H.: Measurements of drop-size distributions during transient dropwise condensation. Journal of Heat Transfer, 97(3):341–346, 1975.
101. Chatterjee, A., Derby, M. M., Peles, Y., and Jensen, M. K.: Condensation heat transfer on patterned surfaces. International Journal of Heat and Mass Transfer, 66:889–897, 2013.
102. Miljkovic, N. and Wang, E. N.: Condensation heat transfer on superhydrophobic surfaces. MRS bulletin, 38(05):397–406, 2013.
103. Daniel, S., Chaudhury, M. K., and Chen, J. C.: Fast drop movements resulting from the phase change on a gradient surface. Science, 291(5504):633–636, 2001.
104. Miljkovic, N., Enright, R., Nam, Y., Lopez, K., Dou, N., Sack, J., and Wang, E. N.: Jumping-droplet-enhanced condensation on scalable superhydrophobic nanostructured surfaces. Nano letters, 13(1):179–187, 2012.
105. Boreyko, J. B. and Chen, C.-H.: Self-propelled dropwise condensate on superhydrophobic surfaces. Physical Review Letters, 103(18):184501, 2009.
106. Miljkovic, N., Preston, D. J., Enright, R., and Wang, E. N.: Electric-field-enhanced condensation on superhydrophobic nanostructured surfaces. ACS nano, 7(12):11043–11054, 2013.
107. Boreyko, J. B.: From dynamical superhydrophobicity to thermal diodes. Doctoral dissertation, Duke University, 2012.
108. Anand, S., Paxson, A. T., Dhiman, R., Smith, J. D., and Varanasi, K. K.: Enhanced condensation on lubricant-impregnated nanotextured surfaces. ACS nano, 6(11):10122–10129, 2012.
109. Kumagai, S., Tanaka, S., Katsuda, H., and Shimada, R.: On the enhancement of filmwise condensation heat transfer by means of the coexistence with dropwise condensation sections. Experimental Heat Transfer, 4(1):71–82, 1991.
110. Ma, X.-h.: Condensation heat transfer of steam on vertical dropwise and filmwise coexisting surfaces with a thick organic film promoting dropwise mode. Experimental heat transfer, 16(4):239–253, 2003.

111. Ma, X., Zhou, X.-D., Lan, Z., Song, T.-Y., and Ji, J.: Experimental investigation of enhancement of dropwise condensation heat transfer of steam-air mixture: falling droplet effect. Journal of enhanced heat transfer, 14(4), 2007.
112. Mishchenko, L., Khan, M., Aizenberg, J., and Hatton, B. D.: Spatial control of condensation and freezing on superhydrophobic surfaces with hydrophilic patches. Advanced functional materials, 23(36):4577–4584, 2013.
113. Enright, R., Miljkovic, N., Alvarado, J. L., Kim, K., and Rose, J. W.: Dropwise condensation on micro- and nanostructured surfaces. Nanoscale and Microscale Thermophysical Engineering, 18(3):223–250, 2014.
114. Thickett, S. C., Neto, C., and Harris, A. T.: Biomimetic surface coatings for atmospheric water capture prepared by dewetting of polymer films. Advanced Materials, 23(32):3718–3722, 2011.
115. Bai, H., Wang, L., Ju, J., Sun, R., Zheng, Y., and Jiang, L.: Efficient water collection on integrative bioinspired surfaces with star-shaped wettability patterns. Advanced Materials, 26(29):5025–5030, 2014.
116. Derby, M. M., Chatterjee, A., Peles, Y., and Jensen, M. K.: Flow condensation heat transfer enhancement in a mini-channel with hydrophobic and hydrophilic patterns. International Journal of Heat and Mass Transfer, 68:151–160, 2014.
117. Beaini, S. S. and Carey, V. P.: Strategies for developing surfaces to enhance dropwise condensation: Exploring contact angles, droplet sizes, and patterning surfaces. Journal of Enhanced Heat Transfer, 20(1), 2013.
118. Durand, M.: Architecture of optimal transport networks. Physical Review E, 73(1):016116, 2006.
119. Ying, J., Eid, K. F., and Sommers, A. D.: Designing energy-efficient heat exchangers creating micro-channels on the aluminum fin surface. International Refrigeration and Air Conditioning Conference, (Paper 1108), 2010.
120. Yin, J. and Jacobi, A.: Condensate retention effects on the air-side heat transfer performance of plain and wavy-louvered heat exchangers. Technical report, Air Conditioning and Refrigeration Center. College of Engineering. University of Illinois at Urbana-Champaign., 2000.

121. Qu, M., Zhang, B., Song, S., Chen, L., Zhang, J., and Cao, X.: Fabrication of superhydrophobic surfaces on engineering materials by a solution-immersion process. Advanced Functional Materials, 17(4):593–596, 2007.
122. Preston, D. J., Miljkovic, N., Sack, J., Enright, R., Queeney, J., and Wang, E. N.: Effect of hydrocarbon adsorption on the wettability of rare earth oxide ceramics. Applied Physics Letters, 105(1):011601, 2014.
123. Rausch, M., Fröba, A., and Leipertz, A.: Dropwise condensation heat transfer on ion implanted aluminum surfaces. International Journal of heat and Mass transfer, 51(5):1061–1070, 2008.
124. Carey, V.: Liquid vapor phase change phenomena taylor-francis. New York, pages 353–371, 2008.
125. Marek, R. and Straub, J.: Analysis of the evaporation coefficient and the condensation coefficient of water. International Journal of Heat and Mass Transfer, 44(1):39–53, 2001.
126. Mikic, B.: On mechanism of dropwise condensation. International Journal of Heat and Mass Transfer, 12(10):1311–1323, 1969.
127. Glicksman, L. R. and Hunt, A. W.: Numerical simulation of dropwise condensation. International Journal of Heat and Mass Transfer, 15(11):2251–2269, 1972.
128. Ma, X.-H., Zhou, X.-D., Lan, Z., Yi-Ming, L., and Zhang, Y.: Condensation heat transfer enhancement in the presence of non-condensable gas using the interfacial effect of dropwise condensation. International Journal of Heat and Mass Transfer, 51(7):1728–1737, 2008.
129. Minkowycz, W. and Sparrow, E.: Condensation heat transfer in the presence of noncondensables, interfacial resistance, superheating, variable properties, and diffusion. International Journal of Heat and Mass Transfer, 9(10):1125–1144, 1966.
130. Grooten, M. and Van der Geld, C.: Dropwise condensation from flowing air-steam mixtures: Diffusion resistance assessed by controlled drainage. International Journal of Heat and Mass Transfer, 54(21):4507–4517, 2011.
131. Quere, D., Azzopardi, M.-J., and Delattre, L.: Drops at rest on a tilted plane. Langmuir, 14(8):2213–2216, 1998.

132. Rose, J.: Some aspects of condensation heat transfer theory. International communications in heat and mass transfer, 15(4):449–473, 1988.
133. LeFevre, E. and Rose, J.: A theory of heat transfer by dropwise condensation. In Chemical Engineering Progress, volume 62, page 86, 1966.
134. Lee, S., Yoon, H. K., Kim, K. J., Kim, S., Kennedy, M., and Zhang, B. J.: A dropwise condensation model using a nano-scale, pin structured surface. International Journal of Heat and Mass Transfer, 60:664–671, 2013.
135. Spalding, D.: The calculation of mass transfer rates in absorption, vaporization, condensation and combustion processes. Proceedings of the Institution of Mechanical Engineers, 168(1):545–570, 1954.
136. No, H. C. and Park, H. S.: Non-iterative condensation modeling for steam condensation with non-condensable gas in a vertical tube. International Journal of Heat and Mass Transfer, 45(4):845–854, 2002.
137. Bonner, R. W.: Correlation for dropwise condensation heat transfer: Water, organic fluids, and inclination. International Journal of Heat and Mass Transfer, 61:245–253, 2013.
138. Torresin, D., Tiwari, M. K., Del Col, D., Poulikakos, D., et al.: Flow condensation on copper-based nanotextured superhydrophobic surfaces. Langmuir, 29(2):840–848, 2013.
139. Thomas, A. V., Koratkar, N., and Peles, Y.: Dehumidification heat transfer on copper surfaces. International Journal of Heat and Mass Transfer, 55(25):7858–7864, 2012.
140. Incropera, F., Bergman, T., Lavine, A., and Dewitt, D.: Fundamentals of heat and mass transfer, John Wiley & Sons, New York. L996, 2011.
141. Seo, D., Lee, C., and Nam, Y.: Influence of geometric patterns of microstructured superhydrophobic surfaces on water-harvesting performance via dewing. Langmuir, 30(51):15468–15476, 2014.
142. Hong, K. and Webb, R.: Performance of dehumidifying heat exchangers with and without wetting coatings. Transactions-ASME Journal of Heat Transfer, 121:1018–1026, 1999.

143. Kim, M.-H. and Bullard, C. W.: Air-side performance of brazed aluminum heat exchangers under dehumidifying conditions. International Journal of refrigeration, 25(7):924–934, 2002.
144. Dehbi, A. and Guentay, S.: A model for the performance of a vertical tube condenser in the presence of noncondensable gases. Nuclear Engineering and Design, 177(1):41–52, 1997.
145. Khawaji, A. D., Kutubkhanah, I. K., and Wie, J.-M.: Advances in seawater desalination technologies. Desalination, 221(1-3):47–69, 2008.
146. Attinger, D., Frankiewicz, C., Betz, A. R., Schutzius, T. M., Ganguly, R., Das, A., Kim, C.-J., and Megaridis, C. M.: Surface engineering for phase change heat transfer: A review. MRS Energy & Sustainability, 1:E4, 2014.
147. Zhao, Q., Zhang, D., Lin, J., and Wang, G.: Dropwise condensation on lb film surface. Chemical Engineering and Processing: Process Intensification, 35(6):473–477, 1996.
148. Rose, J. and Glicksman, L.: Dropwise condensation the distribution of drop sizes. International Journal of Heat and Mass Transfer, 16(2):411–425, 1973.
149. Ma, X., Wang, S., Lan, Z., Peng, B., Ma, H., and Cheng, P.: Wetting mode evolution of steam dropwise condensation on superhydrophobic surface in the presence of noncondensable gas. Journal of Heat Transfer, 134(2):021501, 2012.
150. Le Fevre, E. and Rose, J.: Heat-transfer measurements during dropwise condensation of steam. International Journal of Heat and Mass Transfer, 7(2):272–273, 1964.
151. Graham, C. and Griffith, P.: Drop size distributions and heat transfer in dropwise condensation. International Journal of Heat and Mass Transfer, 16(2):337–346, 1973.
152. Abu-Orabi, M.: Modeling of heat transfer in dropwise condensation. International journal of heat and mass transfer, 41(1):81–87, 1998.
153. Castillo, J. E., Weibel, J. A., and Garimella, S. V.: The effect of relative humidity on dropwise condensation dynamics. International Journal of Heat and Mass Transfer, 80:759–766, 2015.

154. Yamada, Y., Ikuta, T., Nishiyama, T., Takahashi, K., and Takata, Y.: Droplet nucleation on a well-defined hydrophilic–hydrophobic surface of 10 nm order resolution. Langmuir, 30(48):14532–14537, 2014.
155. Vorobyev, A. and Guo, C.: Multifunctional surfaces produced by femtosecond laser pulses. Journal of Applied Physics, 117(3):033103, 2015.
156. Dietz, C., Rykaczewski, K., Fedorov, A., and Joshi, Y.: Visualization of droplet departure on a superhydrophobic surface and implications to heat transfer enhancement during dropwise condensation. Applied physics letters, 97(3):033104, 2010.
157. Zhong, L., Xuehu, M., Sifang, W., Mingzhe, W., and Xiaonan, L.: Effects of surface free energy and nanostructures on dropwise condensation. Chemical Engineering Journal, 156(3):546–552, 2010.
158. Peng, B., Ma, X., Lan, Z., Xu, W., and Wen, R.: Experimental investigation on steam condensation heat transfer enhancement with vertically patterned hydrophobic–hydrophilic hybrid surfaces. International Journal of Heat and Mass Transfer, 83:27–38, 2015.
159. Hou, Y., Yu, M., Chen, X., Wang, Z., and Yao, S.: Recurrent filmwise and dropwise condensation on a beetle mimetic surface. ACS nano, 9(1):71–81, 2014.
160. Izumi, M., Kumagai, S., Shimada, R., and Yamakawa, N.: Heat transfer enhancement of dropwise condensation on a vertical surface with round shaped grooves. Experimental Thermal and Fluid Science, 28(2):243–248, 2004.
161. Zhu, J., Luo, Y., Tian, J., Li, J., and Gao, X.: Clustered ribbed-nanoneedle structured copper surfaces with high-efficiency dropwise condensation heat transfer performance. ACS applied materials & interfaces, 7(20):10660–10665, 2015.
162. Malik, F., Clement, R., Gethin, D., Krawszik, W., and Parker, A.: Nature’s moisture harvesters: a comparative review. Bioinspiration & biomimetics, 9(3):031002, 2014.
163. Nørgaard, T., Ebner, M., and Dacke, M.: Animal or plant: which is the better fog water collector? PloS one, 7(4):e34603, 2012.
164. Hamilton, W. J. and SEELY, M. K.: Fog basking by the namib desert beetle, *onymacris unguicularis*. Nature, 262(5566):284–285, 1976.

165. Chatterjee, A., Derby, M. M., Peles, Y., and Jensen, M. K.: Enhancement of condensation heat transfer with patterned surfaces. International Journal of Heat and Mass Transfer, 71:675–681, 2014.
166. Aarts, D. G., Lekkerkerker, H. N., Guo, H., Wegdam, G. H., and Bonn, D.: Hydrodynamics of droplet coalescence. Physical review letters, 95(16):164503, 2005.
167. Ambrosini, W., Forgione, N., Manfredini, A., and Oriolo, F.: On various forms of the heat and mass transfer analogy: Discussion and application to condensation experiments. Nuclear Engineering and Design, 236(9):1013–1027, 2006.
168. Liao, Y. and Vierow, K.: A generalized diffusion layer model for condensation of vapor with noncondensable gases. Journal of Heat Transfer, 129(8):988–994, 2007.
169. Dehbi, A., Janasz, F., and Bell, B.: Prediction of steam condensation in the presence of noncondensable gases using a cfd-based approach. Nuclear Engineering and Design, 258:199–210, 2013.
170. Lan, Z., Wen, R., Wang, A., and Ma, X.: A droplet model in steam condensation with noncondensable gas. International Journal of Thermal Sciences, 68:1–7, 2013.
171. Park, S.-Y., Teitell, M. A., and Chiou, E. P.: Single-sided continuous optoelectrowetting (scoew) for droplet manipulation with light patterns. Lab on a Chip, 10(13):1655–1661, 2010.
172. Long, Z., Shetty, A. M., Solomon, M. J., and Larson, R. G.: Fundamentals of magnet-actuated droplet manipulation on an open hydrophobic surface. Lab on a Chip, 9(11):1567–1575, 2009.
173. Huang, S., Song, J., Lu, Y., Chen, F., Zheng, H., Yang, x., Liu, X., Sun, J., Carmalt, C. J., Parkin, I. P., et al.: Underwater spontaneous pumpless transportation of nonpolar organic liquids on extreme wettability patterns. ACS Applied Materials & Interfaces, 2016.
174. Marlow, J.: Why space craft of the future will be packed with microfluidics? Wired, 2013.
175. Koukoravas, T. P., Ghosh, A., Mahapatra, P. S., Ganguly, R., and Megaridis, C. M.: Spatially-selective cooling by liquid jet impinging orthogonally on a wettability-patterned surface. International Journal of Heat and Mass Transfer, 95:142–152, 2016.

**VITA**

# Aritra Ghosh

+1- 312 479 0732, aritra.jadavpur@gmail.com  
842 W Taylor Street, MC 251-ERF, University of Illinois at Chicago, USA-60607

## EDUCATION

**PhD Candidate**, Mechanical Engineering (GPA-3.83/4.0) **Summer 2017**

*Micro/Nanoscale Fluid Transport Laboratory, University of Illinois at Chicago (UIC)*

**Course concentration:** Thermodynamics, heat transfer, fluid mechanics

**Thesis:** Pumpless manipulation of micro-volume liquids on surfaces using wettability engineering.

Advisor: Constantine Megaridis

Committee Members: Ryan Enright, W.J. Minkowycz, Ranjan Ganguly, Amin Salehi Khojin

- 7 international peer-reviewed articles, 15+ international conference talks/workshops, led to 2 grant applications ~ \$1m in funding, 5 inventions (1 PCT pending, 2 provisional, 2 invention disclosure)

**BE**, Power Engineering (GPA-8.6/10, Top 3)

**June 2011**

**Jadavpur University (JU), India**

**Thesis:** Comparison of spray characteristics between pressure and air assisted atomizer.

- 1 international conference publication

Top 1% out of all India WB-JEE exam and top 2.5% out of all India IIT-JEE exam

## RESEARCH EXPERIENCE

**Micro/Nanoscale Fluid Transport Laboratory (UIC) (PI: Constantine Megaridis)** **Aug 2012 - present**

*PhD Candidate*, performed research on fluid transport, with applications on heat transfer, lab on chip and microbiome capture. Focus on wettability engineered surfaces for pumpless transport and manipulation of liquid. Proficient in facile surface preparation by spray processing, laser based etching and wet chemistry. Experienced in designing thermos-fluids experiments, surface preparation and characterization, high-speed imaging and image processing (ImageJ, MATLAB).

**Bell Labs, Dublin, Ireland (PI: Ryan Enright)**

**Jan 2015- July 2015**

*Research Intern*, Efficient Energy Transfer ( $\eta$ ET)

Developed scalable phase change heat transfer surfaces for enhanced electronics cooling. Worked in machine shop, fitting shop and fabricated an experimental setup for heat transfer performance testing (dropwise condensation).

**FA University of Erlangen, Germany (PI: Thomas Seeger, Alfred Leipertz)**

**June 2010 - July 2010**

*Summer Research Intern*, Institute for technical Thermodynamics (LTT)

**DAAD-WISE** fellow, Responsible for constructing an experimental setup on laser (LIG) based combustion diagnostics to measure the species concentration of fuel (propane) vapor.

**Jadavpur University, India (PI: Amitava Datta)**

**June 2010 - May 2011**

*UG Thesis*, Designing and fabricating MIE scattering setup to compare spray characteristics between pressure and air assisted atomizers. Focus on developing a laser based light sheet to image spray droplets from different nozzles.

## AWARDS and FELLOWSHIPS

- **Deans Fellowship 2017** highest distinguished award from UIC in recognition of distinguished graduate students and their scholarly achievement. \$22000 and tuition waiver.
- **ThinkChicago Fellow 2016**, 200 selected nationwide (USA) to network and participate in Chicago's emerging startup scene.
- **Chancellor's Student Leadership award 2016** for exceptional leadership service to the university and community
- **GSC Travel award 2013, 2016** for presenting at conferences. \$550 towards airfare.
- **Faydor Litvin award 2012** for best incoming graduate student in the department (out of ~150 students). \$3000
- **DAAD-WISE Fellowship 2010** undergraduate research internship at Erlangen, **Germany**. €2000

## PEER REVIEWED PUBLICATIONS, Citations – 240 (Google Scholar)

- Morrisette, Jared M., Pallab Sinha Mahapatra, **Aritra Ghosh**, Ranjan Ganguly and Constantine M. Megaridis. "Two-Dimensional Wettability-Patterned Designs for Rapid, Self-Driven Liquid Micromixing", **Scientific Reports** 7 (2017): 1800.
- Enright, Ryan, **Aritra Ghosh**, Anne Gallagher, Shenghui Lei and Tim Persoons. "Apparent Slip Enhanced Magnetohydrodynamic Pump", **Proceedings in Itherm** 2016, Las Vegas, USA
- Koukoravas, Theodore P., **Aritra Ghosh**, Pallab Sinha Mahapatra, Ranjan Ganguly, and Constantine M. Megaridis. "Spatially-selective cooling by liquid jet impinging orthogonally on a wettability-patterned surface." **International Journal of Heat and Mass Transfer** 95 (2016): 142-152.

- Mahapatra, Pallab Sinha, **Aritra Ghosh**, Ranjan Ganguly, and Constantine M. Megaridis. "Key design and operating parameters for enhancing dropwise condensation through wettability patterning." **International Journal of Heat and Mass Transfer** 92 (2016): 877-883.
- Song, Jinlong, Shuai Huang, Yao Lu, Xiangwei Bu, Joseph E. Mates, **Aritra Ghosh**, Ranjan Ganguly et al. "Self-driven one-step oil removal from oil spill on water via selective-wettability steel mesh." **ACS Applied materials & Interfaces** 6, no. 22 (2014): 19858-19865.
- **Ghosh, Aritra**, Sara Beaini, Bong June Zhang, Ranjan Ganguly, and Constantine M. Megaridis. "Enhancing dropwise condensation through bioinspired wettability patterning." **Langmuir**, no. 43 (2014): 13103-13115.
- **Ghosh, Aritra**, Ranjan Ganguly, Thomas M. Schutzius, and Constantine M. Megaridis. "Wettability patterning for high-rate, pumpless fluid transport on open, non-planar microfluidic platforms." **Lab on a Chip**, no. 9 (2014): 1538-1550.

#### **PUBLICATIONS IN PREPARATION**

- **Ghosh, Aritra**, Souvick Chatterjee, Pallab Sinha Mahapatra, Ranjan Ganguly and Constantine Megaridis, "Morphological evolution of liquid volumes on wettability engineered tracks", (*in preparation*)
- **Ghosh, Aritra**, Souvick Chatterjee, Pallab Sinha Mahapatra, Ranjan Ganguly and Constantine Megaridis. "Pumpless Surface Microfluidics", **invited review**, (*to be submitted*)
- **Ghosh, Aritra**, Anne Gallagher, Tim Persoons and Ryan Enright. "Nusselt number formulae for Hartmann flow with asymmetric hydrodynamic and thermal slip", *JHMT (in preparation)*

#### **INVENTIONS**

- C. M. Megaridis, **A. Ghosh**, R. Ganguly and T. M. Schutzius, "Wettability Patterned Substrates for Pumpless Liquid Transport and Drainage," **International PCT Patent** Application Number PCT/US2015/012302 A1 (filed on 01-21-2015).
- C. M. Megaridis, J. M. Morrisette, P. Sinha Mahapatra, **A. Ghosh**, R. Ganguly, "Self-Driven Surface Micromixer," U.S. Provisional Patent Application 62/258,195 (filed on 11-20-2015).
- C. M. Megaridis, T. P. Koukoravas, **A. Ghosh**, P. Sinha Mahapatra, R. Ganguly, "Spatially-Selective Cooling with Wettability-Engineered Surfaces," U.S. Provisional Patent Application 62/258,060 (filed on 11-20-2015).

#### **TALKS**

- 69<sup>th</sup> American Physical Society, Division of Fluid Dynamics, November 2016, Portland, USA
- Microfluidics Congress, July 2016, Philadelphia, USA
- Invited Talk, Jadavpur University, January 2016, Kolkata, India
- 68<sup>th</sup> American Physical Society, Division of Fluid Dynamics, November 2015, Boston, USA
- Gordon Research Conference on Micro Nano scale heat transfer, January 2015 Galveston, USA
- 67<sup>th</sup> American Physical Society, Division of Fluid Dynamics, November 2014, San Francisco, USA
- SelectBIO conference on Lab on a Chip technology, September 2014, San Diego, USA
- Joint 12<sup>th</sup> International Conference on Nanochannels, Microchannels and Minichannels and 4<sup>th</sup> European Fluids Engineering Division, August 2014, Chicago, USA
- Material Research Society Fall 2013 Conference, December 2013, Boston, USA (contributed)
- 66<sup>th</sup> American Physical Society, Division of Fluid Dynamics, November 2013, Pittsburgh, USA

#### **WORKSHOPS/SYMPOSIUMS**

- 1<sup>st</sup> Midwest Mechanics Workshop at UIUC, August 2015, Champaign, USA
- Symposium on Hybrid Materials, University of Michigan, October 2014, Michigan, USA
- 9<sup>th</sup> International Symposium on Contact Angle, Wettability and Adhesion, June 2014, Lehigh University, Bethlehem, USA
- Workshop on Micro Nano Scale Heat Transfer, MIT, April 2013, Boston, USA

#### **TECHNOLOGY TRANSFORMATION EXPERIENCE**

##### **PreScouter, Chicago**

**Feb 2017 – present**

*Global Scholar*, Technology Consulting

Providing research data and insight on R&D planning and product development to corporate innovation leaders in sustainable energy applications.

##### **ENTERPRISEWORKS CHICAGO (EWC), Chicago**

**Sep 2015 – Dec 2016**

*Lead Consultant*, Technology Commercialization

- Led team of consultants and analysts (post-doc, PhD, Master student). Spearheaded the competitive landscape analysis as well as barriers for market entry for water and energy technologies (battery, filtration, CO2 capture)
- Interviewed clients to identify the value proposition and industry experts to assess the pain points. Proposed future course of action to the technology team based on market analysis and investor appetite.

## TEACHING AND MENTORING

---

### Teaching Assistant, UIC

Jan 2013 – present

Taught problem solving classes, laboratory classes, graded tests and homework assignments for ME211: Introduction to Fluid Mechanics, ME429; Internal Combustion Engines, ME421: Intermediate Heat Transfer, ME341: Experimental Methods in mechanical Engineering.

### Master's student mentored, UIC

- **Rucha Bapat**, UIC 2016 (present: working at LUK, Schaeffler Group )  
Thesis: Fluorinated POSS based polymer nanocomposites for super repellency of oils.

### Undergraduate students supervised, UIC

- **Apoorva Sooranahalli**, UIC 2017 (present: Grad student at UC Berkeley)  
Thesis: Wettability patterned surfaces for pumpless transport of oils.
- **Kenneth Brenner**, UIC 2017  
Thesis: Surface fabrication for a one-step wickless vapor chamber.

## ACADEMIC AND PROFESSIONAL ACTIVITIES

---

### Professional Society Membership

American Physical Society, Materials Research Society, ASME, American Chemical Society

### Peer Reviewed Reviewer for

Langmuir, RSC Advances, Applied Material & Interfaces, Chemical Communications (RSC), Journal of Colloids and Interface Science

## LEADERSHIP EXPERIENCE

---

### Advanced Degree Consulting Club, UIC, Chicago

Apr 2016 – present

*Founder & Vice President*, Initiated with 5 students and persuaded ~ 100 members to join including graduate students, post docs and faculty. Formulated and hosted several sessions (information, case practice, resume workshop) related to consulting.

### Graduate Student Association, UIC, Chicago

Aug 2013 – Jul 2014

*President*, Doubled intra- department graduate student communication. Secured reduction (by 50%) in additional college fees for PhD students.

## ADDITIONAL INFORMATION

---

**Media Coverage:** National Science Foundation News Top 5 most watched [videos](#), **Buzzfeed** How water phobic material may help save [earth](#)?

**Startup workshop on:** Intellectual Asset Management, Market Validation, Operating a Company, Venture Capital Overview

**Interests:** Avid Traveler (Visited 16 and worked in 4 countries), post rock, sarod, pint of science.